PULSED FAR-INFRARED EXPERIMENTS ON DYNAMICAL PROPERTIES IN SEMICONDUCTOR SYSTEMS

R.E.M. de BEKKER

PULSED FAR-INFRARED EXPERIMENTS
ON DYNAMICAL PROPERTIES
IN SEMICONDUCTOR SYSTEMS

PROMOTORES: PROF. Dr. P. WYDER
PROF. Dr. H. VAN KEMPEN

CO-PROMOTOR: Dr. L.M. CLAESSEN (E.P.O.)

PULSED FAR-INFRARED EXPERIMENTS ON DYNAMICAL PROPERTIES IN SEMICONDUCTOR SYSTEMS

ISBN 90-9004591-0

PULSED FAR-INFRARED EXPERIMENTS ON DYNAMICAL PROPERTIES IN SEMICONDUCTOR SYSTEMS

een wetenschappelijke proeve op het gebied van
de natuurwetenschappen

PROEFSCHRIFT

ter verkrijging van de graad van doctor aan
de Katholieke Universiteit Nijmegen
volgens besluit van het college van decanen
in het openbaar te verdedigen op
maandag 2 december 1991
des namiddags te 3.30 uur

door

RUBEN EGIDIUS MARIA de BEKKER
geboren te Deventer

PROMOTORES: ·	PROF. Dr. P. WYDER PROF. Dr. H. VAN KEMPEN
CO-PROMOTOR:	Dr. L.M. CLAESSEN (E.P.O.)

Dit proefschrift is tot stand gekomen mede dankzij de steun en medewerking van eigenlijk iedereen die ik goed ken. Daarom wil ik aan het begin van dit boekje al mijn vrienden en kennissen zowel buiten als binnen de fysica, zowel in Frankrijk als in Nederland en elders, van harte bedanken voor hun bijdragen.

Ondanks de onmogelijkheid allen persoonlijk te noemen zou ik hier echter toch enkelen met name willen vermelden.

- Allereerst Michiel voor het inwijden in de wereld van de experimentele Vaste Stof Fysica en voor het samen schouder aan schouder doorbreken van ettelijke barrieres in Grenoble alsook voor de 'common sense' gesprekken onder het genot van koffie of een ander donker vocht.
- Martyn for his motivating discussions by facsimile and his travelling to Grenoble several times for doing experiments always with an open mind for the relativity involved in what we are doing.
- In Grenoble de medewerkers van het Hochfeld-Magnetlabor en het Service National des Champs Intenses voor de internationale ambiance in het lab, met name Peter Scheuzger und Herr Dr. Müller für ihre Freundschaft und Spass an der Physik, Herbert, Hans, Albin en Werner für die technische Unterstützung, André Plante pour ses solution efficaces et rapide, Valmir, Christoph en Jan-Cees who were very much involved in accomplishing the last chapter. Henk, Louis, Jan-Cees en de rest van de Nederlandse club voor hun collegialiteit.
- In England, Mohammed for kindly growing the samples, G. Hill for the processing of electric contacts and Richard, Mark and Martyn for all their help.
- In Nijmegen vooral Riki voor haar onmisbare hulp en Tos en Herman voor de opbouwende kritiek aangaande het manuscript.
- Edith, Jan en mijn moeder voor de onmisbare morele steun.
- Als laatste maar eigenlijk als meest belangrijke, op duizend kilometer hier vandaan, Angela omdat ze Angela is.

Hier, op deze plaats, acht ik het ook gepast een moment mijn vader te herinneren mede uit dank voor alles wat hij voor mij gedaan en betekend heeft en dankzij wiens invloed dit proefschrift mede tot stand is gekomen.

Grenoble, september 1991
Ruben de Bekker

voor Angela,
voor mijn moeder,
en voor mijn vader.

CONTENTS

CHAPTER 4 SPIN LATTICE RELAXATION MEASUREMENTS UNDER ELECTRON PARAMAGNETIC RESONANCE CONDITIONS BY MEANS OF A PICK-UP COIL

CHAPTER 5 FAR INFRARED ASSISTED TUNNELLING IN DOUBLE BARRIER RESONANT TUNNELLING STRUCTURES

CHAPTER 1

GENERAL INTRODUCTION

Far infrared (FIR) spectroscopy has proven to be a very powerful technique in the study of semiconductors. This is due to the correspondence of the energies of the FIR photons with some typical energies in semiconductors eg. optical phonon energies, ionisation energies of hydrogen-like impurities, Zeeman splitting energies and cyclotron energies. These energies typically range from about 0.5 meV to 50 meV for wavelengths of 2000μm to 20 μm respectively.

The generation of FIR radiation can be achieved very conveniently by using a Michelson interferometer or by using continuous wave optically pumped molecular gas lasers which can operate at a variety of wavelengths. The power level for the emitted radiation, however, is rather low (power $\leq$ 10 mW/cm^2).

Much higher power levels can be obtained by using these molecular lasers in combination with strong pulsed pump lasers, like the transverse excited atmospheric carbon dioxide laser (TEA CO_2). Pulses with power of the order of MW/cm^2 with a duration of about 100 nanoseconds can be reached with such a technique. Application of such powerful pulses in experimental FIR studies of semiconductors creates several new possibilities. Whilst for continuous sources the experimental studies are mostly restricted to equilibrium properties and linear phenomena, application of powerful pulsed sources offer an efficient means to study non-equilibrium properties and non-linear phenomena. This may be understood considering the two most important properties of pulses which are the resolution in time and the high power. The first offers the possibility to study dynamical effects by observing time resolved responses, whilst the second may be important to observe non-linear effects by enhancing the importance of higher order dependencies of electric or magnetic fields.

In this thesis a study of the generation of pulses and pulse sequences as well as their applications in several experimental studies is presented. These experiments consider nanosecond resolved recombination dynamics of shallow donor impurities, spin dynamics in dilute magnetic semiconductors (spin-lattice relaxation) and the transport dynamics through double barrier resonant tunnelling structures.

To study these different dynamic effects which can be induced by pulsed FIR radiation, it is necessary to apply different experimental methods and therefore this thesis is organised as follows:

In chapter 2 a detailed description is given of this FIR pulse laser and its performance. As for all experiments described in this thesis the excitation source used to study the different effects was a pulsed optically pumped FIR laser. The pulses which have a duration of about 100 ns can be switched on and off by means of plasma-reflection switches for which the principle of operation consists of the reflection of FIR radiation by an electron-hole plasma which can be induced in the surface of a semiconductor by high power irradiation with above-bandgap light. Rise and fall times of the resulting pulses are in the order of 1 ns. A special application of this technique is the use of an intra-cavity switch in order to generate cavity-dump pulses shorter than 10 ns and with a power of several kW. Using the same technique it has been possible to obtain pulse sequences and a two-pulse sequence has been successfully generated consisting of two pulses of 10 ns with a time interval of 100 ns in between.

Chapter 3 concerns time-resolved photoconductivity measurements to study the recombination dynamics of photo-ionised shallow donors and electrons in n-GaAs bulk and AlGaAs/GaAs quantum wells. Shallow donor impurities are atoms in the host lattice of the semiconductor of which the electrons in the outer atomic shell are weakly bound. Such a donor can give up one electron to the conduction band, leaving behind a single fixed positive charge. This situation is equivalent to the well known hydrogen atom in vacuum and therefore, binding energies of the electron to the impurity atom can be accurately described using a hydrogen-like model for which the free electron mass is replaced by the effective electron mass and the dielectric permitivity is multiplied by the static dielectric constant of the host material. For III-V semiconductors an effective Rydberg is found of the order of 5 to 10 meV. The ground state is called the 1s level and the most important excited states are the 2s and 2p levels which are degenerate at zero magnetic field.

In general, at low temperatures, conduction in semiconductors which are slightly n-doped occurs through the presence of free electrons in the conduction band coming from ionised shallow donor impurities. The ionisation process occurs by thermal excitation, impact ionisation or optical excitation from the ground state directly in the conduction band or to excited states followed by further thermal or impact ionisation. Therefore photo-(thermal)conduction represents an important mechanism for the operation of FIR detectors, since conductivity is directly proportional to the intensity of the incident radiation, or for use in characterising the impurity contents of a sample.

If a magnetic field is applied to the hydrogen-like system the degeneracy of its energy levels is lifted. The optical transition rate of the $1s \rightarrow 2p^+$ transition becomes dominant. This offers the opportunity to make narrow band tunable FIR detectors. An important question of a detector is how fast can it react to radiation. Therefore, it is interesting to look at the dynamical response of the shallow donor system. In chapter 3 an experimental study is presented where the photoconductive response is measured after excitation with very short FIR pulses from the ground state to to $2p^+$ state with a nanosecond resolution. Recombination times of electrons with photo-ionised shallow donors were determined as a function of doping concentration, temperature, electric field, as well as dimensionality which can be reduced by putting the donor impurities in a quantum well structure or by application of a magnetic field or both.

In comparison with previous time-resolved studies [1], the experiments as presented in chapter 3 are characterised by much better controlled instrumentation which offers a less ambiguous means of interpreting the results. A FIR excitation stimulus of a few nanoseconds with well defined rise and fall characteristics is used instead of quite long stimuli for which only the fall-off characteristic was well controlled. Furthermore, the resolution of the detection system with one nanosecond offers the possibility of a more detailed study of recombination dynamics. Due to the application of very short FIR pulses with well known rise and fall times the observation of the whole photoconductive process makes it possible to exclude artifact effects caused by, for example, changes in the electron mobility.

Another difference with former studies is the use of shallow donor systems in quantum well structures. The effect of the confinement due to the quantum well barriers strongly enhances the binding energy and reduces the physical extension of the wavefunctions of such a system in respect to the normal bulk case. Such an effect may also be achieved by the application of a magnetic field. From previous studies, the reduction of the recombination time with increasing magnetic field could be explained by a theory which describes transition probabilities under emission and absorption of acoustic phonons [1]. In this study, the same arguments are used to explain the very fast (<1ns) recombination in case of shallow donor systems in quantum wells.

It is noted that the recombination rates are strongly affected by the concentration of the acceptor impurities N_A. In a simple theory considering rate equation arguments, where only the acoustic phonon interaction is taken into account, this dependence on the macroscopic value N_A is explained.

An interesting anomaly was observed which for electric fields above a certain value showed a very pronounced "tail"-structure (>10μs). These structures are attributed to impact excitation and -ionisation of excited hydrogen-like states, and using rate equation arguments [2] the lifetime of the lowest excited bound state could be estimated.

In chapter 4 a technique is presented to study the process of pulsed electron paramagnetic resonance (EPR) in high magnetic fields by means of a pick-up coil.

In the absence of a magnetic field, a spin system consisting of uncoupled spins having a total spin "S" will be multi-fold degenerate because the $S_z=-S, -S+1, \ldots, S-1, S$ states all have the same energy. Application of a magnetic field lifts this degeneracy and the levels are split by the Zeeman energy (1meV/10Tesla for g-factor $\simeq$ 2). Between these non-degenerate levels optical transitions can be induced if the selection rule $\Delta S_z=1$ is satisfied. Evidently, satisfaction of this condition will change the magnetisation of a spin system under EPR conditions which may be probed by inductive measurements.

In the experiment described in chapter 4, this change in the magnetisation of a paramagnetic crystal due to a resonant EPR FIR pulse is detected as an induction voltage in a pick-up coil around the crystal. After the excitation process the spin system relaxes back to thermal equilibrium due to spin-lattice coupling. Again an induction signal is observed, though with opposite polarity. In this way it is possible to measure directly the spin lattice relaxation (SLR) time.

The SLR time is investigated in a dilute magnetic semiconductor consisting of a CdTe crystal in which a small part of the Cd^{2+} ions is replaced by paramagnetic Mn^{2+} ions. The SLR times have been measured as a function of temperature and within the experimental resolution the results were explained by one-phonon processes.

An other important relaxation process for spin systems is known as spin-spin relaxation which concerns the phase coherence of the spins. Experimental techniques for measuring these processes rely on excitation by pulse sequences to observe electron spin echoes (ESE). In the appendix of chapter 4 a small feasibility study of such an experiment for FIR excitation will be discussed.

Finally, in chapter 5 an experimental study is described concerning the influence of FIR radiation on the transport properties through a double barrier tunnel structure.

With crystal growth techniques such as molecular beam epitaxy, it has become possible to grow artificial quantum structures in compound semiconductor materials reliably. In 1970, the quantum mechanical phenomenon of tunnelling was observed in an artificial solid state material consisting of a quantum well sandwiched between barriers [3]. It is well known that under resonant bias voltage conditions (where the electron in the emitter has the same energy as the subband in the quantum well) the transmission of electrons through such a structure is maximal and no reflection from the potential barriers is noted.

However, the fundamental mechanism is still under discussion. The "coherent" process is similar to the Fabry-Perot etalon in optics [3] in which the electron spends a certain time inside the well, being multiply reflected in the barriers, before leaving the structure. This process will have typical transit times which are longer than the oscillation period of FIR radiation. The "sequential" process on the other hand [4] describes a tunnelling process initially through the the first barrier and subsequently through the second. In between both tunnel steps the electron phase memory may be completely lost by scattering. Typical scattering times may be estimated to be shorter than the oscillation period of the FIR.

Therefore, in chapter 5 an experimental study is described concerning the influence of FIR radiation on the transport properties through a double barrier tunnel structure and it is argued that this can be used to probe whether the main tunnelling process is dominated by a coherent or a sequential mechanism. This is possible because typical transit times for the different mechanisms are longer or shorter, respectively, than the oscillation period of FIR radiation.

Because the I-V characteristic is highly nonlinear a rectification signal is expected if an oscillating electric field is applied. In this chapter will be argued that the rectified signal due to FIR irradiation should be frequency dependent for the case where tunnelling in the structures is governed by "coherent" processes. Due to the fact that no frequency dependence is detected it is concluded that in the structures under study the tunnelling process is mainly sequential.

All experiments were carried out at the laboratory for high magnetic fields (Hochfeld-Magnetlabor) from the Max-Planck-Institut für Festkörperforschung in Grenoble (France).

References

[1] G.L.J.A. Rikken, P. Wyder, J.M. Chamberlain, G.A. Toombs, and L.L. Taylor, Phys. Rev. B **38**, 2002 (1988).

[2] J.M. Chamberlain, A.A. Reeder, L.M. Claessen, G.L.J.A. Rikken, and P. Wyder, Phys. Rev. B **35**, 2391 (1985).

[3] R.L. Tsu and L. Esaki, Appl. Phys. Lett. 22, 562 (1973).

[4] S. Luryi, Appl. Phys. Lett. 47, 490 (1985).

CHAPTER 2

GENERATION OF SHORT FAR INFRARED PULSES

ABSTRACT

In this chapter various methods are presented to generate short far infrared (FIR) laser pulses. The short FIR pulses (100ns.) are obtained by an optically pumped molecular gas laser. To modulate the temporal behaviour of these pulses an optical switching technique is described consisting of an optical element of which the reflectivity is controlled by modulating the free carrier concentration using specific radiation. A FIR cavity dump laser is presented which has been realised using this technique, by mounting the optical element intra-cavity under the Brewster angle with respect to the optical axes. This system produces very short high power ($\propto$ 1 kW) FIR pulses with a duration of less than 10 ns.
Pulse detection techniques are also briefly discussed.

(Parts of this chapter have been published in J. Appl. Phys. **68**, 3729 (1990))

2.1 Introduction

Time-resolved far infrared (FIR) spectroscopy is a powerful method to observe dynamical properties in semiconductors. Usually in such experiments the material response to a short FIR laser stimulus is studied as a function of time (see chapter 3). Therefore, the generation of FIR pulses with a well known time behaviour, needed to study these dynamical features, has been under development for a long time. To generate very short pulses various techniques are available. In the lower frequency range for instance advanced microwave pulse techniques are commercially available, whereas in the high frequency region (IR and visible) electro optical modulators exist, for mode-locking and Q-switching. However, all these techniques unfortunately do not operate efficiently in the FIR.

Therefore, alternative techniques have recently been developed to obtain FIR pulses: Semiconductor lasers have been realised from p-Ge in which stimulated emission is due to transitions between the light and heavy hole bands, with an inverted population occuring when the crystal is subject to crossed electric and magnetic fields (power < 10W; $\lambda \simeq 75$-250 μm; duration <1 μs) [1,2]. Landau-emission sources made from n-GaAs or n-InSb have radiative transitions between Landau levels which provide a magnetically tunable emission in the FIR (1 μW; $\lambda \simeq 60$-500 μm; 1 ns rise time) [3]. Also FIR pulses have been generated by difference-frequency mixing of two high power pulsed optical lasers by using a non linear electro optical $LiNbO_3$ crystal (kW; $\lambda \simeq 50$ - 500 μm; picoseconds) [4]. A very complicated but versatile source of high power frequency-tunable coherent radiation is the Free Electron Laser, which uses a high-quality high energy (relativistic) electron beam passing through a periodic transverse magnetic field (wiggler or ondulator), to generate and amplify an electromagnetic (optical) wave (power < 40 kW; $\lambda \simeq 120$-800 μm; duration <50 μs [7]) [5,6]. However these sources are mostly in an experimental phase and/or commercially not available.

The conventional way of obtaining FIR pulses is by optically (IR) pumping a molecular gas cavity with a pulsed CO_2 laser [8,9]. Roughly FIR radiation will be present as long as the CO_2 stimulus is present. An additional advantage of the use of a pulsed instead of a continuous wave (cw) CO_2 pump laser is that much higher power can be obtained in the FIR radiation, because of its much higher pump power. In the first section of this chapter a system will be described producing pulses with wavelengths between λ= 60-2000 μm.

Obviously, to observe nanosecond processes, one needs FIR laser pulses with a defined and well known temporal behaviour of the same time scale. By applying standard optical techniques CO_2 pump lasers can supply pulses even shorter than a nanosecond. However, it is not feasible to transfer short IR pulses ($t< 10$ns) into FIR pulses, because the typical lifetimes of the exited states in the molecular medium of the FIR laser are of the order of 100 ns. The practical lower limit of the duration of FIR pulses, generated in this way, is on the order of 20-30 ns. Therefore it is necessary to shape up the existing laser pulse after its generation.

A widely applied method to modulate and control the evolution in time of existing IR laser radiation is optical switching (OS), which consists of controlling the optical properties of an element in the light path by means of appropriate illumination. Normally, a semi-insulating semiconductor is transparent for (far)-infrared radiation due to the absence of free carriers. Intense above-bandgap radiation (photon energy in excess of the bandgap) forms an electron plasma by excitation of free carriers into the conduction band. This electron plasma will strongly enhance the reflectivity of the material, allowing the switch-on and -off of (far)-infrared radiation in reflection and transmission respectively [10,11]. OS has been successfully applied in the infrared to produce very short laser pulses [10,12] and has recently been extended into the FIR [13,14], where it already has been used to terminate abruptly a long FIR laser pulse in order to measure decay times in FIR photoconductive processes in semiconductors [15,16]. In these experiments fall-off times of the order of a few nanoseconds have been obtained. In addition, a second OS element can be used to cut off the rising part of the pulse in order to make well defined short pulses. The theoretical and experimental approach of this OS technique will be described subsequently.

A new method is also reported in which the OS element is used for cavity dumping a FIR laser. Here the OS element is a semi-insulating semiconductor slab placed under the Brewster angle inside the cavity of a conventional optically pumped molecular gas laser. During illumination with above-bandgap light, this OS element couples out the laser radiation. Consequently, all further laser action is stopped due to the strong decrease of the cavity Q-factor. Therefore a FIR pulse is obtained with a duration that equals the time needed by the remaining FIR photons to leave the cavity via the OS element, and consequently the pulse duration is only determined by geometrical factors.

With this novel cavity-dumping technique ultra short FIR pulses with a well defined temporal behaviour can relatively easily be realised using only one single OS element. In the wavelength range from $\lambda=100$ μm to 600 μm the described laser system can produce pulses with a duration of 7 ns and a peak power of $\propto$ 1 kW .

In the last section the detection techniques of FIR pulses will be shortly discussed.

2.2 Laser system

The main part of the laser system consisted of a pulsed CO_2 laser, which was used to pump a FIR molecular gas laser cavity. In this way it was possible to produce powerful FIR pulses (≃ 1kW), with a duration governed by the duration of the CO_2 stimulus (typically about 100 ns) and wavelengths between λ= 60-2000 μm. The experimental set-up is shown in Fig. 2.1. In the following both CO_2 and FIR lasers will be discussed more fully.

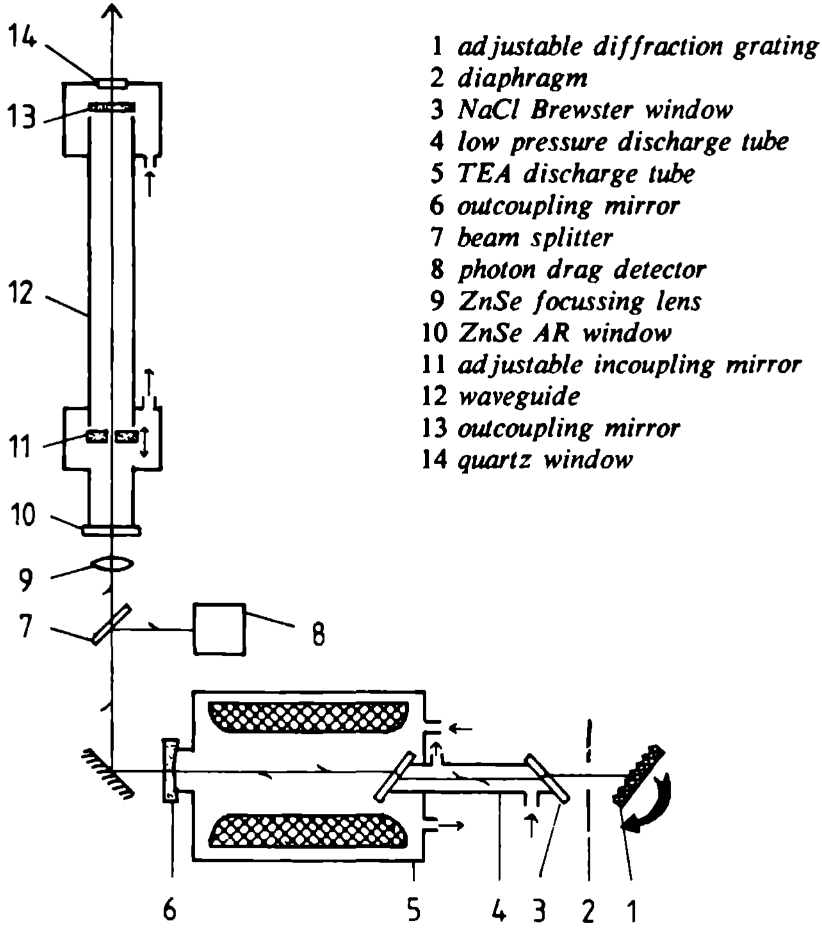

1 *adjustable diffraction grating*
2 *diaphragm*
3 *NaCl Brewster window*
4 *low pressure discharge tube*
5 *TEA discharge tube*
6 *outcoupling mirror*
7 *beam splitter*
8 *photon drag detector*
9 *ZnSe focussing lens*
10 *ZnSe AR window*
11 *adjustable incoupling mirror*
12 *waveguide*
13 *outcoupling mirror*
14 *quartz window*

Fig 2.1 *Configuration of the pulsed FIR laser system.*

The pump laser is a two section Transversely Excited Atmospheric pressure (TEA) CO_2 laser (Lumonics 820) which provided high power pulses of about 500 kW with a typical duration of 100 ns. In order to pump efficiently, the bandwidth of the TEA-CO_2 laser should be matched to the typical absorption bandwidth of 30 MHz/mbar of the molecular gas laser. Therefore, to compress the large inversion bandwidth ($\simeq$ 4 GHz) of the atmospheric CO_2 section of the laser cavity, also an intra cavity low pressure section is involved [17]. Under correct tuning conditions this low pressure section, with a typical selectivity of 75 MHz at 25 mbar favours only one out of several longitudinal cavity modes, which have a typical spacing of about 150 MHz. This favoured mode is given an extra independent gain, and as such a preference in the mode competition, which is inherent to a wide gain profile, as available in the section with the atmospheric CO_2. Because the homogeneous nature of this wide gain profile (pressure broadening) the major part of the inversion energy will be transferred into this single mode [18] yielding a pulse power of over 500 kW on the strongest lines. In this way single longitudinal mode operation is obtained on 75 lines in the 9.4-10.6 μm range.

The FIR laser is of the conventional waveguide design. The vertically polarised infrared is focussed by a $f = 40$ cm lens into the FIR cavity through the 1 mm hole of a conventional incouple mirror which is translatable to adjust the cavity length. The cavity consists of a cylindrical dielectric (quartz) waveguide with an inner diameter of 10 mm and a typical length of 120 cm through which the medium flowed. With a conventional hole outcoupling mirror the FIR pulse follows that of the IR as shown in Fig. 2.2.

However, due to the high pump intensity of the TEA-CO_2 laser, the resulting FIR gain bandwidth includes more than one longitudinal mode. Because of the interference of these longitudinal modes, having small frequency differences, mode-beating occurs. This results in a rather chaotic temporal behaviour of the pulse (see Fig. 2.2). To obtain spectral purity, and as such to obtain smooth pulses (see Fig. 2.2), it is necessary to restrict the cavity oscillation to one single longitudinal and transversal mode of the resonator as in the case of the TEA-CO_2 laser. In the FIR however, an intra cavity frequency selective element, as has been used in the TEA-CO_2 laser, would not be convenient because the loss of power and handling ease in the changing of the FIR frequency. The mode selectivity of the FIR cavity can be optimised though, by changing the dimensions and material of the cavity, varying the pressure of the medium, and by using frequency selective outcouple devices, such as metal mesh mirrors or hybrid coated mirrors [19,20,21].

By reducing the length of the cavity, the longitudinal modes are more separated. On the other hand by reducing the diameter of the cavity, higher order transversal modes are dampened, and as such the cavity is made more selective and suited for single mode operation. An additional advantage of a

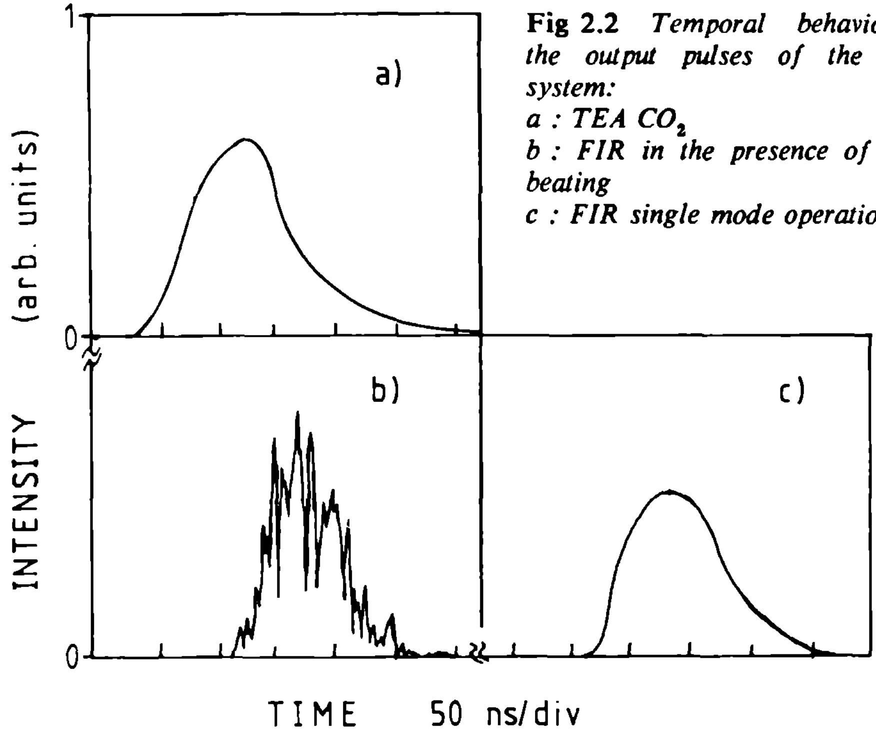

Fig 2.2 *Temporal behaviour of the output pulses of the laser system:*
a : TEA CO_2
b : FIR in the presence of mode beating
c : FIR single mode operation.

smaller cavity diameter (d) is that due to the $1/d^2$ dependence of the vibrational relaxation rate [19], the population inversion is increased, by the improved emptying of the lower laser level. This effect allows higher pressures which also results in a broadening of the gain bandwidth. As such stronger mode competition will occur, which again favorites only a few of the possible modes.

However for long wavelength radiation ($\lambda > 600\mu m$), in spite of the above mentioned advantages, bigger diameters are favorited because the transmission losses in a dielectric waveguide, which are proportional to λ^2/d^3 [21], become appreciable in this frequency region. These transmission losses for the lowest loss modes in a cylindrical dielectric quartz waveguide, such as the almost equally attenuated EH_{11} linearly polarised mode and the TE_{01} doughnut-shaped mode, are comparable to the losses in a copper or brass waveguide whose diameter is one order of magnitude smaller than that of the dielectric guide [19]. As a result of boundary condition rules (the EH_{11} mode is forbidden in a conducting waveguide) in such brass waveguides the lowest loss mode is found to be the TE_{01} mode. Considering reasonable dimensions and pumping efficiency brass waveguides were used for the generation of FIR radiation with wavelengths longer than 600μm.

As mentioned, optimisation of mode selection also can be realised by metal mesh outcoupling devices. These metal meshes have a uniform reflectance and transmission over the entire mirror (contrary to hole mirrors) making them favourable for the EH_{11} mode, which has its intensity maximum in the center of the dielectric waveguide. The IR reflection efficiency of the outcoupling device is not that important because the short IR absorption length in the high pressure molecular gas makes multiple passing not needed. By varying the grid geometry of the meshes one can also reduce the number of longitudinal modes by defining the smallest outcouple losses of a given frequency in the highest part of the gain bandwidth and hence optimise the laser output [20].

In Table I the FIR wavelengths are summarised which were obtained with this system, showing a reasonable coverage of the FIR spectral range.

Table I *Typical performance of the FIR pulse laser.*

$\lambda(\mu m)$	medium	pressure(mbar)	pumpline	power(Watt)
66	D_2O	10	9P32	10^3
90.9	NH_3	14	9R16	$2 \cdot 10^3$
118	CH_3OH	8	9P36	$5 \cdot 10^2$
148	NH_3	25	9P34	$8 \cdot 10^2$
151	NH_3	8	10P32	$3 \cdot 10^2$
231	CH_3F	12	9R30	$3 \cdot 10^2$
292	NH_3	25	10R06	$8 \cdot 10^2$
496	CH_3F	5	9P20	$1 \cdot 10^3$
570	CH_3OH	2	9P16	$2 \cdot 10^1$
751	CH_3I	5	9P24	$2 \cdot 10^1$
1055	CH_3I	5	10P32	$2 \cdot 10^1$
1218	$C^{13}H_3F$	4	9P32	$1 \cdot 10^2$
1899.9	C_2H_3Br	5	10P20	$2 \cdot 10^1$

2.3 Generation of very short pulses by optical switching

In the preceding section a system was presented to obtain short FIR pulses of about 100ns duration. These pulses follow the CO_2 stimulus and as such their temporal behaviour is totally governed by duration of the CO_2 pump pulse. Many techniques are available to create much shorter pump pulses, however it is not evident how to transfer these shorter IR pulses into shorter FIR pulses, because the typical lifetimes of the excited states in the gas molecules of the FIR laser are about 100 ns. To be able to obtain very short FIR pulses, optical switching techniques can be used for shaping up the already existing short FIR pulses.

2.3.1 Optical switching: theoretical

The principle of optical switching (OS) is the creation of a dense electron plasma in a semi-insulating semiconductor. This plasma is created by optically exciting electrons into the conduction band. The optical properties of this plasma can be characterised by the plasma frequency ω_p, given by

$$\omega_p^2 = \frac{N_e e^2}{m_{eff} \epsilon_0 \epsilon_\infty} \tag{2.1}$$

where N_e is the electron density, e the electronic charge, m_{eff} the effective electron mass, and ϵ_∞ the optical dielectric constant of the medium [10]. In principle all radiation with frequencies below ω_p is totally reflected from the plasma surface and as such any transmission through the semiconductor will be totally blocked.

About 25 years ago already devices were described to modulate the intensity of long wavelength radiation by using free carrier reflection and absorption in semiconductors, induced by radio frequency (RF) voltages [22]. Nowadays, using high power optical lasers high electron densities up to 10^{26} m^{-3} can be reached even on a picosecond timescale: for most semiconductors such an electron density corresponds to a plasma frequency in the near-infrared.

Total reflection can be achieved only in the ideal situation of a perfect semi-infinite plasma without any scattering, see Fig. 2.3. However, an electron-hole plasma generated by absorption of above bandgap photons, has a spatially dependent density profile due to the finite penetration depth of the optical radiation. A typical plasma extends up to several μm into the semi-

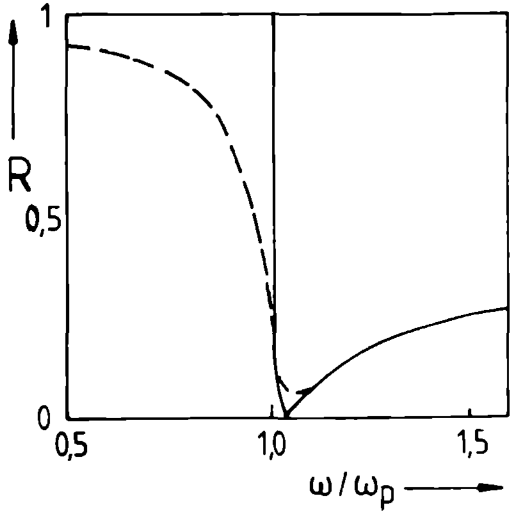

Fig 2.3 *Reflection efficiency (R) of a semiconductor as a function of frequency* ω *relative to the plasmafrequency* ω_p, *in the region of the plasma edge, with (dashed line) and without (solid line) electron collisions.*

conductor. After the above bandgap radiation has been stopped, this profile will change in space and in time due to diffusion into the semiconductor as well as recombination.

If the skindepth of the radiation to be reflected is larger than the plasma thickness, some of the light will be transmitted and consequently the reflection will be less than 100 %. For infrared radiation this condition is not very relevant, as skin-depths are less than a μm [10]. For FIR however, skin-depths can be larger and can exceed the thickness of the plasma. In such a situation the plasma can not be considered anymore to be semi-infinite.

An exact determination of the skin-depth and reflection efficiency of FIR in OS elements depends on the electron mean free path and the complicated density profile of the hot electron plasma, and is beyond the scope of this work. However, some insight might be gained by considering a simplified model incorporating a semi-infinite plasma with a time independent electron density N_e and a time and frequency independent scattering time τ. Now the dielectric function can be written according to the Drude model, by [23]

$$\epsilon(\omega) = \epsilon_\infty \left\{ 1 - \frac{(\omega_p \tau)^2}{1+(\omega\tau)^2} + \frac{i(\omega_p \tau)^2}{(1+(\omega\tau)^2)\omega\tau} \right\} \tag{2.2}$$

The strong increase in reflectivity with decreasing ω at ω_p (plasma edge) can be explained by a change of sign of $\epsilon(\omega)$, which, in the case of $\tau \to \infty$, is a real quantity. It is easily shown that, under the conditions $\omega\tau >> 1$ and $\omega < \omega_p$, any plane wave in the plasma will have an imaginary wavevector k and therefore an evanescent wave will extend into the plasma as far as the skin-depth δ, which can be expressed as [23,24]

$$\delta = \frac{1}{|k|} = 1/\left| \frac{\omega}{c} \sqrt{\epsilon} \right| \simeq \frac{c}{\omega_p} \simeq 1\ \mu m \tag{2.3}$$

where $\omega_p = 2 \cdot 10^{14}\ sec^{-1}$ ($\lambda \simeq 10\ \mu m$) as given by eq.(1) with a carrier concentration of $10^{26}\ m^{-3}$ and an effective mass $m_{eff} = 0.1 m_0$. This penetration depth is smaller than the typical plasma thickness and no radiation will propagate. Therefore the plasma can be estimated to be nearly 100% reflecting and the transmission will be zero. On the other hand, for $\omega\tau >> 1$ and $\omega > \omega_p$, $\epsilon(\omega)$ will be positive and radiation can normally propagate.

However, for finite τ, the dielectric function $\epsilon(\omega)$ will be complex and as such absorption effects will be involved. Reflection will be not that efficient (see also Fig. 2.3), although the efficiency of the decrease in transmission will hardly be affected.

In the situation where ω_τ exceeds the frequency of the applied FIR ($\omega << \omega_\tau$: $\omega\tau << 1$) the dielectric function (equation 2.2) of the plasma can be approximated with the Hagen-Rubens relation. For $\epsilon(\omega) = \epsilon'(\omega) + i\epsilon''(\omega)$ now ϵ' is considered constant and $\epsilon'' \propto 1/\omega$ [23]. This predicts a skindepth of the order of

$$\delta = \frac{c}{\omega_p} \sqrt{\frac{1}{\omega\tau}} \tag{2.4}$$

which can exceed the plasma thickness. Under these circumstances the plasma can not be considered as semi infinite, and as such reflection will be less efficient. Hence a FIR lower frequency limit ($\omega\tau \simeq 1$) for which OS still works efficiently can be provided by an estimation of the electron collision frequency ω_T of the semiconductor material. Based on room temperature mobility data critical wavelengths of $\lambda_c \simeq 600\mu m$ in GaAs, and $\lambda_c \simeq 300\mu m$ in Si can be obtained [25]. Indeed the experiments showed that the OS element (GaAs) had a frequency dependent reflectivity during illumination, starting at 50% at $\lambda=500\mu m$, and rapidly increasing with decreasing wavelength. High reflection efficiencies were obtained up to $\lambda = 10\ \mu m$ (CO_2 radiation).

The temporal behaviour of the optical properties of the induced plasmas are strongly related to the electron diffusion into the material and to the wavelengths involved. A detailed description of these effects is presented in Ref. 10. Another important factor is the choice for a direct- or indirect-gap semiconductor. For the first material-choice it is evident that the induced plasma will be present nearly as long as the illuminating stimulus, whilst for the latter a plasma can stay up to microseconds, due to the reduced decay rate back to the valence band.

Applications of this optical switching technique will be discussed in the next two sections.

2.3.2 Optical switching: experimental

The conventional way of using the optical switching technique to "shape up" the time behaviour of an existing FIR pulse is shown in Fig. 2.4. The two optical switches involved are of semi-insulating semiconductor slabs (thickness $\simeq 0.5\mu m$; resistivity $\simeq 10^7\ \Omega cm$) which are normally transparent for (far)-infrared radiation. The first switch is used to switch the final pulse 'on', by reflecting the FIR beam towards the second switch. This second one is used in transmission, to switch the final pulse 'off'.

To obtain optimal switching efficiency, these devices are installed at the Brewster angle with respect to the incoming FIR radiation. This results in a maximum of transmission and a minimum of reflection for the correct light polarisation. Normally the FIR light is linearly polarised parallel or perpendicular with respect to the CO_2 pump laser, dependent on the spe-cific transition. If necessary, a polarisation flipper was used to adjust the po-larisation of the CO_2 laser by 90°. Such a device consists of seven mirrors in a helical configuration [26]. To optimise the FIR polarisation, an additional polariser was put into the FIR beam.

To create the electron-hole plasma in the surface of these semiconductor slabs, the second harmonic radiation of a Q-switched pulsed Nd:YAG laser (Quanta ray DCR 2A) with filled-in beam optics was used. This laser provided pulses with a wavelength of 533nm and a typical energy of 1 Joule

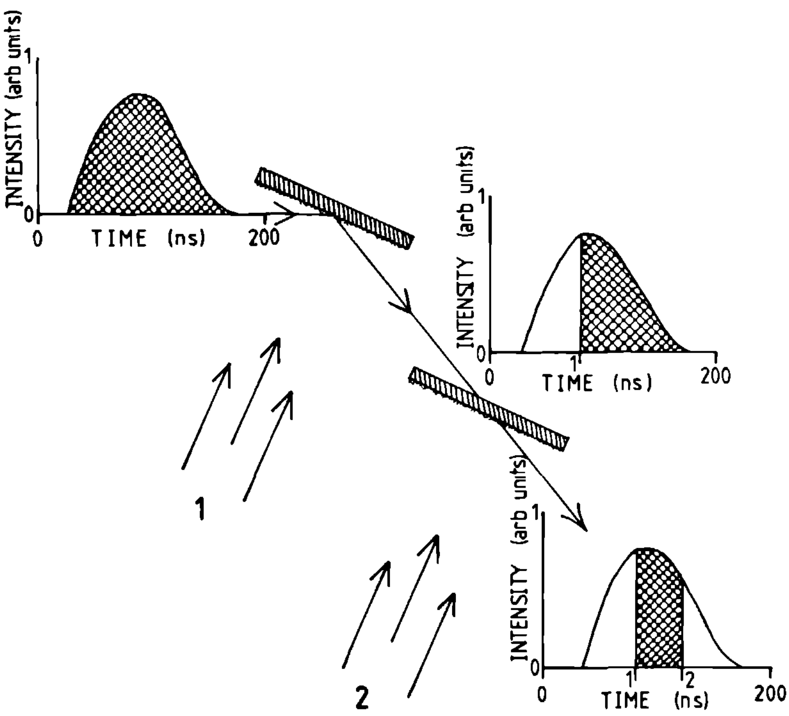

Fig 2.4 *Experimental configuration for FIR pulse shaping using OS elements in reflection and transmission. The resulting FIR pulse is given by the hatched part. The mutually delayed Nd:YAG laser beam to irradiate the first and second switch are referred to as 1 and 2 respectively.*

in 10 ns. To supply both of the switches with the above bandgap radiation the Nd:YAG laser beam was split in two. The fraction intended to irradiate the transmission switch (Fig. 2.4) was intentionally delayed by a geometric delay line. The duration of the shaped-up pulse now is defined by the geometrical factors: The difference in optical path from both the Nd:YAG laser pulses to the switches minus the optical path of the FIR between the switches. The switching performance was found to be dependent on the Nd:YAG laser pulse power and the photon energy as well as the choice of the semiconductor material. The photon energy should exceed the bandgap energy of the semiconductor involved and the Nd:YAG laser pulse power should be sufficient to create a high enough plasma density. The reflection efficiency was strongly reduced, when too high power or too high photon energy was used, by the heating up of the plasma and the generation of large amounts of phonons by the cooling plasma and the fact that the absorption rate is reduced as $E_{photon} \gg E_{bandgap}$ [27]. Using the second harmonic Nd:YAG laser photons ($E_{ph} \simeq 2.3$ eV) already at the threshold of the laser (100 mJ) severe surface damaging could be observed for Ge ($E_{gap} \simeq 0.66$ eV). For Si ($E_{gap} \simeq 1.12$ eV) and for GaAs ($E_{gap} \simeq 1.42$ eV) a damaged surface was only observed at much higher pulse energies. Without the above bandgap radiation, the spurious reflectivity of a semiconductor slab was clearly enhanced by the damage of the surface, which makes the OS less efficient. For an undamaged surface this spurious reflection can be estimated to be less than 1%. Therefore Si and GaAs switches were used. These showed a typical transmission reduction of 2 to 3 orders of magnitude in less than 1 ns. The reflectivity rise time was also about 1 or 2 ns, depending of the Nd:YAG laser pulse energy. For longer wavelengths (λ>300μm) GaAs was preferred rather than Si because of the switching performance as was expected from previous section.

To obtain very short pulses with a duration between 1 and 10 ns the double switch set-up (see Fig 2.4) was normally operated with the direct bandgap material GaAs for the first switch (reflection; pulse 'on') and GaAs or Si for the second one (transmission; pulse 'off'). For the generation of longer pulses an indirect gap material as Si should be used also for the first switch. The reason for this is that the induced plasma in an indirect-gap material can stay up much longer than is the case in a direct-gap material, which will last only some nanoseconds after cessation of the above bandgap irradiation (see foregoing section). However, while generating longer pulses, only a transmission switch is applied to obtain a semi infinite pulse with a fast cut-off. This is because there is a time jitter between the electrical trigger pulse of the Q-switch of the Nd:YAG laser and the optical output pulse of the CO_2 laser, of the order of more than 10 ns. The origin of this is in the jitter between the optical output pulse of the CO_2 laser and the corresponding electrical synchronisation signal, which finally triggers the Q-switch of the Nd:YAG laser. This jitter reduces the overlap of the FIR pulse with the time window for shaping up this pulse. Another reason can be found in the complexity of the optical delay for one of the split-off Nd:YAG laser pulses (10ns $\propto$ 3m). To perform time resolved response measurements this jitter problem does not enter the data acquisition because all electronics is triggered by the signal of a fast photo diode responding to the Nd:YAG laser pulse. This offers a jitter free synchronisation with the experiment.

2.3.3 Cavity dump laser

In the previous sections a method has been described, to modulate the temporal behaviour of an existing FIR pulse. In this method two OS elements are needed outside the FIR cavity for switching the pulse 'on' and 'off'. In this section a novel method is reported in which only a single OS element is used for both reflection and transmission by cavity dumping the FIR laser. The set up is shown in Fig. 2.5. Here the OS element existed of a semi insulating GaAs slab (as before) which was placed under the Brewster angle inside the cavity of a conventional optically pumped pulsed molecular gas laser. The distance between the incoupling mirror and the OS device was typically 110 cm and the outcoupling mirror was replaced by gold mirror, which reflects about 100%.

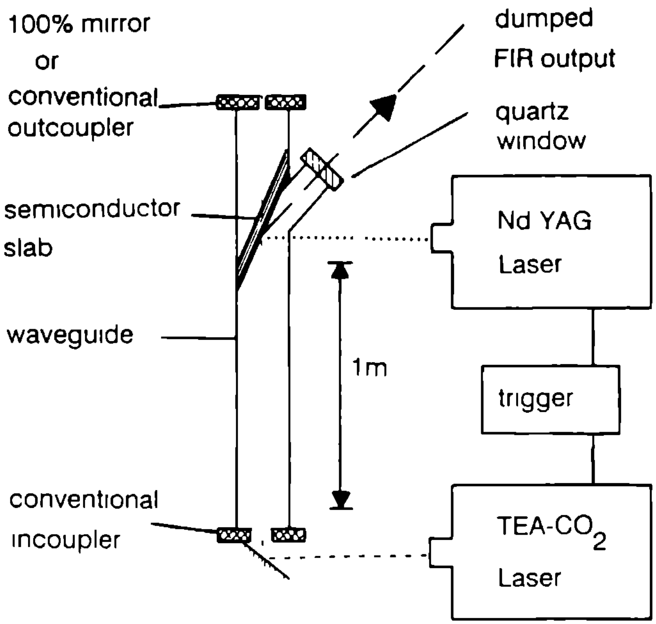

Fig 2.5 *Experimental configuration of the cavity dump laser.*

During illumination with above bandgap light (second harmonic of YAG laser), this OS element couples out the laser radiation. Consequently, all further laser action is stopped due to the strong decrease of the cavity Q-factor. In this way a FIR pulse is obtained with a duration corresponding to the time needed by the remaining FIR photons to leave the cavity via the OS element, and consequently the pulse duration is only determined by geometrical factors. Therefore the FIR pulses generated this way all have a duration corresponding to the time needed to traverse twice the cavity, having a length of 110 cm which corresponds to $\simeq$ 7 ns. The rise and fall times of these resulting pulses are about 1 ns.

Some results obtained this way are shown in Fig. 2.6 and some pulse data are shown in Table II. The data for the 496μm wavelength however correspond to a superradiant laser transition and will be subsequently discussed.

In the cavity dump mode, the polarisation of the CO_2 light must be parallel to the polarisation of the emitted FIR light. The reason for this is that otherwise the OS element does not function as a Brewster element for the CO_2 light, which will then be blocked and consequently there will be no inversion between the OS element and the 100% mirror, resulting in a net

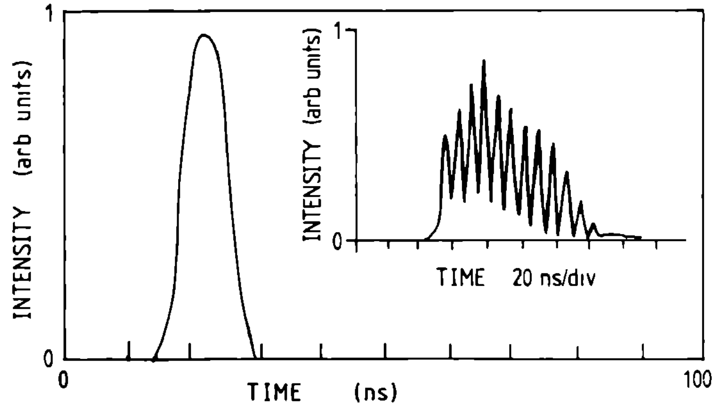

Fig 2.6 *Cavity dump pulse produced using intra cavity optical switching. The inset shows a cavity dump output in the presence of mode-locking.*

loss instead of a gain in this part of the cavity. Now mode-locking occurs, giving rise to a rapidly oscillating FIR pulse as shown in the inset of Fig. 2.6. This effect can also be observed for correct polarised light, when the CO_2 laser is attenuated and the OS element is slightly tilted from the Brewster angle. Also if the OS element has a poor surface quality (for instance a damaged surface caused by too much Nd:YAG-laser power) some mode-locking can occur.

In direct-gap semiconductors, the reflectivity only stays at a high level during 10-20 ns. At pump powers far above the threshold level needed for FIR laser action, the laser action will immediately be restored after the recovering of the Q-factor of the cavity. This is shown in Fig 2.7, where the resulting FIR pulse from the dump cavity is monitored, after it has been coupled out by means of conventional outcoupling mirror (replacing the 100% reflector). Therefore the cavity dump system offers the possibility to dump two or even more short pulses out of the cavity during a single CO_2-laser pulse (≃100 ns) by simply splitting the Nd:YAG laser beam and geometrically delaying a part of this beam. However, due to the time jitter of the synchronisation between the CO_2 and Nd:YAG laser (≃ 20 ns), a second pulse should rather be realised by making an independent second CO_2 pulse by splitting and delaying the CO_2 laser too (see next section).

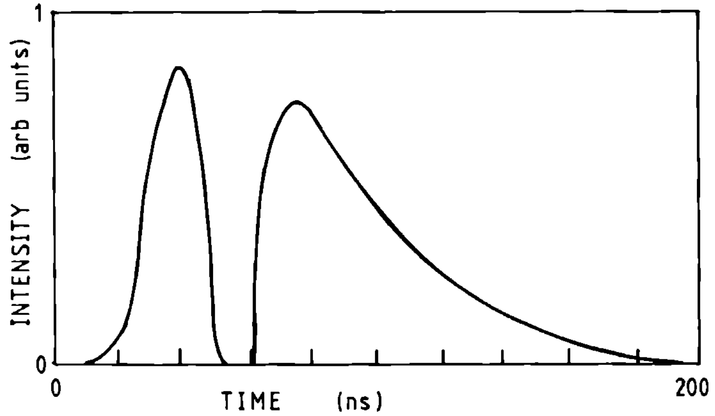

Fig. 2.7 *Output of dump cavity by conventional outcoupling, showing fast recovery of the FIR laser action.*

As discussed above, in the cavity dump mode only FIR output is possible during illumination of the OS element. However, due to some spurious reflection at the surfaces a FIR background signal will be present as long as the CO_2 stimulus is present. Under normal conditions (non damaged clean surface) this background has about 2 % of the intensity of the cavity dumped-pulse. To reduce the background after cessation of the FIR cavity dump, a second OS transmission device made of Si (an indirect-gap semiconductor) has been placed in the outcoming beam. This element was illuminated with a part of the Nd:YAG laser beam that had been appropriately delayed, and as such blocked all further FIR radiation ($\simeq$ 99 %). In this way the background after the cavity dumped pulse could be reduced to less than 0.1%. By tuning the delay it was also possible to shorten the FIR pulse to a few nanoseconds. As mentioned above, such a shortening can in principle also be realised by decreasing the distance between the OS element and incouple mirror of the FIR laser.

If superradiant transitions occur, the medium gain is so high that there is no need for a cavity to obtain FIR laser action, as is the case for λ=496 μm (see Table II) [9,28]. FIR laser action will now be present as long as a CO_2 stimulus is available, independent on the optical state of the OS device. The duration of the FIR pulse reflected out by the OS element is governed only by the time behaviour of its reflection efficiency. As discussed before, for a direct gap semiconductor this time will be 10-20 ns when a stimulating YAG pulse of about 10 ns is used, which is consistent with the experimental results of Table II.

Table II *Experimental results for different FIR laser lines. The data marked * present a superradiant transition.*

λ (μm)	medium	pumpline	duration (ns)	power(Watt)
66.0	D_2O	9P32	7	$2\cdot10^3$
90.9	NH_3	9R16	7	$5\cdot10^3$
118	CH_3OH	9P36	7	$1\cdot10^3$
148	NH_3	9P34	7	$1.5\cdot10^3$
231	CH_3F	9R30	7	$8\cdot10^3$
292	NH_3	10R06	7	$2\cdot10^3$
496*	CH_3F	9P16	10-20	$2.5\cdot10^3$

The advantage of using this cavity dump technique over the conventional way of generating very short FIR pulses (see foregoing section), is that much higher output powers are attainable. By using the cavity dump technique, 100% of the intra-cavity FIR power is in principle available for the resulting very short pulse. By obtaining very short pulses in the conventional way, however, only the much weaker pulse, from a conventional cavity output, is used. In comparison with the intra-cavity power, the power of this conventional output pulse is reduced 90% by the efficiency of the outcoupler of the FIR laser (typically between 10-20 %). In actual experiments the typical power of a dump pulse was twice the power of the output of the conventional pulse laser and up to ten times the power of a pulse obtained by using OS in the conventional way. An additional advantage of the cavity dump technique is that this system has a rather straightforward experimental configuration which improves the stability and reduces jitter.

2.3.4 Two pulse sequence

A sequence of two very short ($\simeq$ 10 ns) high power FIR pulses, with a temporal separation up to a few hundred nanoseconds make a new and interesting tool for the observation of dynamical properties with typical timescales of the same order of magnitude. Such a sequence could be applied in a future pump-probe experiment, studying for example spin-lattice relaxation times [see chapter 4], or in the case of sufficiently powerful pulses, such a pulse sequence could be used as the stimulus for submillimeter Electron Spin Echo (ESE) experiments (see appendix 4.6). A typical pulse sequence is shown in Fig. 2.8. In the following the method, of obtaining this pulse sequence will be discussed shortly.

The generation of the very short pulse ($\simeq$ 10 ns) was obtained by the cavity dump laser. To obtain the double pulse sequence both the Nd:YAG-laser and the CO_2 laser were split in two equal parts by 50%/50% beamsplitters. For both split off beams an optical delay was installed of 100 ns, which is an optical path of 30 m. In Fig. 2.9 a schematic view of the optical paths are given.

For the Nd:YAG-laser, with filled-in beam optics, the diameter of the spot size after 14 m was about 7 cm. Here the beam was reflected, respectively by two short focus ($f = 60$ cm; $\phi = 10$ cm) aluminium spherical mirrors. The inter-mirror distance was bigger than twice the focal length in order to obtain an outgoing converting beam. A third flat aluminium mirror was used for pointing the beam in the right direction. The 14 m path length was folded by three dielectric mirrors which can reflect the small spot beam

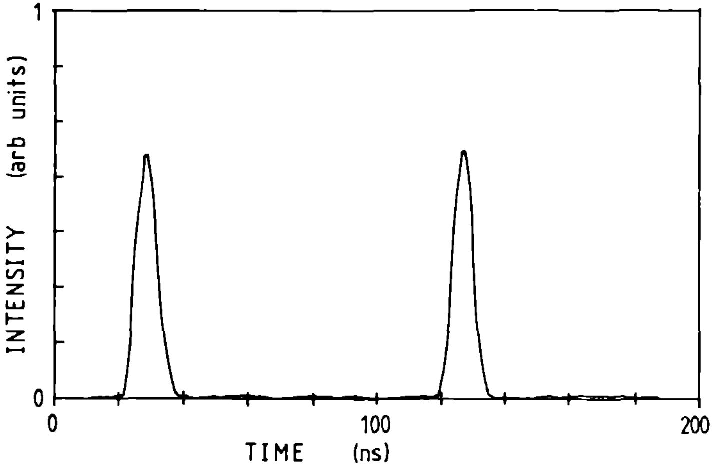

Fig. 2.8 *Double pulse sequence, showing two pulses (λ = 496 μm) of about 10 ns duration with a time interval of 100 ns.*

without being damaged by the high intensity (the reason for the use of aluminium mirrors only at expanded beam). This set-up is easily adjustable if another delay is needed. The coupling to the OS element (after again 14 m) was realised using nearly the same optical axes as the non delayed beam.

For the CO_2 laser beam the divergence is not as small as is the case for the Nd:YAG-laser. Therefore after 3 m the beam was reflected 5 times on the same long focus (f = 7.5 m; ϕ = 12 cm) gold mirror, each time after being reflected back from one out of four flat gold mirrors, placed on a distance of about 3 m from this long focus mirror. In this delay line two focii was obtained. After a path of 30 m the delayed CO_2 beam was coupled in to the optical axes of the non delayed beam by a second beam splitter before the focussing lens, which governs the incoupling in to the cavity. Alignment was optimised by controlling the interference pattern of both beams as seen on a beam visualiser. Both CO_2 pulses were able to generate equally powered FIR pulses.

The reproducibility concerning the power and width of the dump pulses, within the sequence of two, or between the different sequences themselves was better than 95%. The pulse power was about 1 kW, as can be expected from the reduction of the CO_2 laser pump power by a factor of 4. Such a power level is nearly sufficient for ESE experiments. These power levels could even be improved by applying a CO_2 amplifier, which can increase the CO_2 power by a factor of about 100.

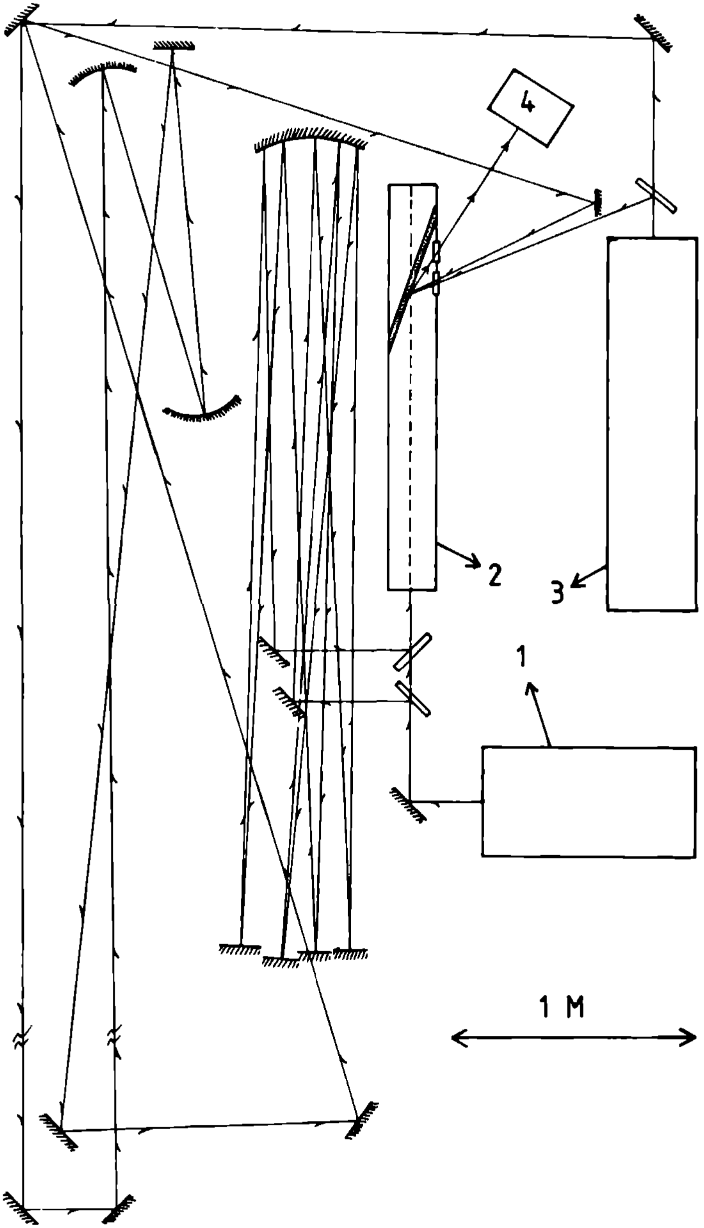

Fig. 2.9 *Schematic drawing of the optical set-up used for realising the double pulse sequence. (1) CO_2 laser; (2) FIR dump laser; (3) Nd:YAG laser; (4) FIR detector*

2.4 Pulse detection

The laser system incorporates several lasers, whose output radiation is very different in wavelength and power. In this section the devices involved to detect the performance of these lasers is presented.

To register the output of the Nd:YAG laser ($\lambda \leq 1 \mu m$) a fast Si photodiode was installed (Centronics BPX 65) which had a risetime of 1 ns. Firstly the signal is used to maximise the power, by optimising the delay of the Q-switch trigger signal relative to the high voltage trigger signal which activates the YAG laser, and secondly to give a jitter-free trigger signal to the electronical data acquisition system of the time resolved measurements.

For the output control of the CO_2-laser ($\lambda \simeq 10 \ \mu m$) a fast photondrag detector was applied, obtaining a nanosecond resolution in the temporal behaviour of the pulse. This enabled the optimisation of the single mode operation in order to get high pumping efficiencies. Power estimations could be made by relative calibration to a pyro detector.

For the time resolved detection of the FIR pulses ($\lambda \simeq 100 - 1000 \ \mu m$) a non commercial room temperature Schottky-barrier diode (MPI Bonn [29]) has been used. This consists of a nonlinear element, rectifying the AC electrical field of the FIR radiation that is coupled into the device by an antenna whisker. The speed limitation is only set by parasitic electronic effects, which depend on the design of the detector. Sensitivity of microwatts is achievable. Although such a high sensitivity is not necessary for the laser pulse detection, it may become very useful to detect the rather weak signals in future Electron Spin Echo experiments [see section 4.6]. An alternative for a Schottky-barrier diode for this application may be given by a Josephson-tunnel diode, which can be faster and with a sensitivity even up to pico Watts [30], though being operational only at liquid helium temperatures. Also fast multiple quantum well extrinsic photoconductors were used as detectors for time resolved measurements of the pulse [29]. The principle of operation of these semiconductor detectors is the photoionisation of their shallow impurity levels which will be discussed in detail in the next chapter. The disadvantage of these devices is that they only operate at low temperatures.

To measure the pulse power of the FIR the 'good old' Golay cell and a calibrated pyro electric detector were applied. These are standard FIR detectors for CW applications based on the temperature rise of a macroscopic body due to absorbed FIR. The typical response time is of the order of 10 ms with a sensitivity for the Golay-cell of about 10^5 V/W. Pyro electric detectors can have much shorter response times up to 10 ns, though with a proportional loss of sensitivity ($\simeq$ 10 V/W). For pulsed application however these devices can be used to measure the total energy in the pulse, which can be converted into power if the pulse duration is known from a fast detector as eg. the Schottky-diode.

References

[1] A.A. Andronov, Y.N. Nozdrin and V.N. Shastin, Infrared Phys. 27, 31 (1987)
[2] S. Kuroda and S. Komiyama, Infrared Phys. 29, 361 (1989)
[3] W. Muller, F. Kohl and E. Gornik, Infrared Phys. **18**, 691 (1978)
[4] M. Borg, C.B. Harris, T.W. Kenny and P.L. Richards, Appl. Phys. Lett. 47, 206 (1985)
[5] B.G. Danley, R.J. Temkin and G. Belefi, IEEE J. Quantum Electron. QE-23, 1739 (1987)
[6] L.R. Elias, G.Ramian, J. Hu and A. Amir, Phys. Rev. Lett. 57 424 (1986)
[7] performance of UCSB (University of California Sant Barbara) [see also Ref. 6].
[8] H.J.A. Bluyssen, A.F. van Etteger, J.C. Maan, and P. Wyder, IEEE J. Quantum Electron. QE-16, 1347 (1980)
[9] C.T.Gross, J. Kiess, A. Mayer, and F. Keilmann, IEEE J. Quantum Electron. QE-23, 377 (1987)
[10] A.J. Alcock and P.B. Corkum, Can. J. Phys. 57, 1280 (1979)
[11] T. Vogel, thesis, (Plasma Inst. Stuttgart, Germany, 1986, unpublished)
[12] P.B. Corkum, Opt. Lett. **8**, 514 (1983)
[13] H. Salzmann, T. Vogel, and G. Dodel, Opt. Commun. 47, 340 (1983)
[14] R.E.M. de Bekker, G.L.J.A. Rikken, T. Strutz, and P. Wyder, *Proceedings of CIRP4 1988*, p. 379, edited by R.Kesselring and F.K. Kneubühl, (ETH Zürich, Switzerland, 1988)
[15] G.L.J.A. Rikken, P.Wyder, J.M. Chamberlain, G.A. Toombs and L.L. Taylor, Phy.Rev. B **38**, 2002 (1988)
[16] G.L.J.A. Rikken, P. Wyder, J.M. Chamberlain, and L.L. Taylor, Europhys. Lett. 5, 61 (1988)
[17] A. Gondhalekar, E. Holzhauer and N.R. Heckenberg, Phys. Lett. A46, 299 (1973)
[18] see e.g. *Laser spectroscopy*, p.550, by W. Demtröder (Springer, Berlin, 1982)
[19] M. Yamanaka, J. Opt. Soc. Am. 67, 952 (1977)
[20] R. Ulrich, Infrared Phys. 7, 37 (1967)
[21] J.J. Degnan, Appl. Phys. 11, 1 (1976)
[22] L.Genzel, Jap. J. Appl. Phys. 4, 353 (1965)
[23] see e.g. *Freie Elektronen in Festkörpern*, p.130, by P. Grosse (Springer, Berlin, 1979)
[24] see e.g. *Introduction to Solid State Physics*, p.258, by C. Kittel (John Wiley & Sons, Inc., New York 1986)
[25] G.L.J.A. Rikken, thesis, (Katholieke Universiteit Nijmegen, The Netherlands, 1987, unpublished)
[26] F. Keilmann, Opt. Comm. 14, 236 (1975).
[27] K. Seeger, *"Semiconductor Physics, an Introduction"*, chapter 11, Springer, Berlin (1982)

[28] D.E. Evans, L.E. Sharp, B.W. James and W.A. Peebles, Appl. Phys. Lett. 26, 630 (1975)

[29] we are grateful to Dr Röser and Dr. H. Nett from Max-Planck-Institut für Radioastronomie in Bonn, Germany, for supplying this device.

[30] P.L. Richards, in *"Semiconductors and Semi-metals"* Vol 12, *"Infrared detectors II"*, chapter 6, eds R.K. Willardson and A.C. Beer, Academic, New York (1977)

[31] R.E.M. de Bekker, L.M. Claessen, P. Wyder, M.B. Stanaway, R.T. Grimes, J.M. Chamberlain, M. Hennini, O.H. Hughes, and G. Hill, J. Appl. Phys. 68, 1913 (1990)

CHAPTER 3

TIME RESOLVED FAR INFRARED MAGNETOSPECTROSCOPY OF PHOTO-IONISED SHALLOW DONOR IMPURITIES IN GaAs EPITAXIAL LAYERS AND GaAs/AlGaAs QUANTUM WELL STRUCTURES.

ABSTRACT

In this chapter the recombination dynamics of shallow donors and electrons in n-GaAs bulk and AlGaAs/GaAs quantum wells has been investigated by measuring the time resolved photoconductive response with nanosecond resolution after excitation with very short FIR pulses to the $2p^+$ (bound) donor state. The main goal of the work was to study the influence on the recombination rate of a confining potential induced by either a magnetic field or by a confining band structure, e.g. the GaAs/AlGaAs quantum well, or both. The observed decay times show a monotonic decrease with increasing magnetic field (as applied up to 10 T) and are very strongly affected by the acceptor concentration N_A. For the quantum well structures, considering the nanosecond resolution of the experiment, subnanosecond decay times are estimated and no further influence of the magnetic field could be resolved. The effects of several parameters such as temperature, electric fields, and FIR pulse intensity have also been investigated. All the observed effects could be satisfactorily explained using numerical estimates from recently developed theory, of the electron-phonon interaction.

(Parts of this chapter have been published in J. Appl. Phys. **68**, 1913 (15 August, 1990); and Materials Science Forum, **65-66**, p. 105 (1990) [Trans Tech Publications, Zürich])

3.1 Introduction

An electron bound to a shallow donor in bulk III-V semiconductors (such as GaAs or InP) is known to be a good analogue of the three-dimensional hydrogen atom, having typical ionisation energies in the far-infrared (FIR) spectral region (see section 3.3). Due to considerable efforts in both theoretical and experimental studies, the energy levels of electrons bound to these hydrogen-like donors in magnetic fields are very well known [1,2]. Recently, due to modern crystal growth techniques, it has become possible to create semiconductor structures, such as AlGaAs/GaAs quantum wells (QW), in which the three-dimensional character of the system is reduced to (quasi) two-dimensional. The energetic behaviour of the hydrogen-like shallow donor in such structures has been investigated by CW FIR techniques and is at this time rather well understood [3,4]. One of the most interesting features of the confinement effect (due to the barriers) on the donor in the well center is the increase of the binding energy up to a factor of four [4].

However, despite the significant interest in hydrogen-like systems, whether in bulk or in QWs, very little attention has been paid to the dynamical aspects within these systems (eg. lifetimes of free and bound states and the transition rates between them). The use of time-resolved (TR) FIR photoconductivity makes it possible to monitor the dynamical properties of the individual transitions by appropriate choice of FIR wavelength and magnetic fields. In contrast with electrical pulse or short wavelength experiments, FIR experiments have the advantage that the photo-excited free electron population is in (quasi-) equilibrium with the lattice, whereas for the other cases such an equilibrium is not attained because of hot electron effects. After the disturbance by pulsed FIR laser excitation, time-resolved (TR) photoconductivity measurements will provide direct information about the recombination of the free electron-photo-ionised shallow donor system [5]. This recombination occurs through capture of a free electron in a bound state, not necessarily a highly excited one, followed by a cascade down to the ground state. In principle it is unknown into which bound state the electron is initially captured. However, the main mechanism for this capture and relaxation process is the emission of acoustic phonons [6,7].

The efficiency of this capture process is shown to be dependent on temperature, acceptor concentration (N_A), electric field, and magnetic field and has been studied by several workers, though only in bulk material [5,8,10]. In time-resolved (TR) FIR photoconductivity experiments in n-InP [10] and saturation photoconductivity measurements in n-GaAs [8] it has been shown that the decay times decrease significantly when a magnetic field is applied. It may be argued that the mechanism for this decrease is the increased phonon emission efficiency occurring because of the shrinkage of the electron wave function of the bound state, as was first discussed in detail by

Toombs [10]. For quantum wells, however, where the wavefunctions of the in-well donors are already squeezed by the quasi-two dimensional geometry, this argument could imply faster relaxation rates in comparison with the rates from comparable bulk material. This argument is the basis for the quantum well experiments as presented in this chapter.

Therefore, in this chapter, a time-resolved photoconductivity study is presented which investigates the recombination of free electrons with photoionised shallow donors in n-GaAs epitaxial layers and AlGaAs/GaAs quantum well structures. In section 2 the applicability of PC to study the subject of recombination is discussed on the basis of some general remarks about PC, to clarify the further sections. In section 3 the energetic behaviour of shallow donor systems in both bulk and QW are discussed. Section 4 describes the relaxation mechanisms and in section 5 the experimental details will be discussed. Section 6 will present the data, which will be interpreted and discussed in the last sections.

The TR-PC is investigated in magnetic fields up to 10 Tesla and the photosignal for the resonant $1s \rightarrow 2p^+$ transition is monitored. FIR pulses of 7 ns, generated by the cavity dump laser (see chapter 2) [11], are used to induce the PC in the samples. In order to be able to reach a nanosecond time resolution in these measurements special care was taken with the FIR stimulus and the electronic measuring circuitry. It was also found necessary to design carefully the contact patterns on the samples in order to reduce the very high impedance of the QW structures in particular.

The measurements on several bulk n-GaAs samples, differing in purity, showed a strong dependence on the acceptor concentration, N_A, even at the highest magnetic fields; this is in contrast to earlier experimental results, realised on n-GaAs [8] and n-InP [10]. Zero field measurements yielded decay times for bulk samples of typically between 8 and 150 ns. A clear decrease in decay time with increasing magnetic field up to 10T was noted; typically this was by a factor between two and three times for the purest sample. For the quantum wells no magnetic field effect was detected, simply because the zero field subnanosecond response times were already within the experimental limit.

A third kind of GaAs sample was measured. This was a bulk sample grown with a non-homogeneous Silicon doping profile, in order to mimic the QW structures but omitting the AlGaAs barriers. In zero field this gave a decay time of 4 ns increasing in field up to 8 ns. This dependence is explained by geometrical effects.

In the last section of this chapter some attention is also paid to an interesting effect, obtained under high bias conditions of the pulsed magneto photoconductivity measurements, which results in a pronounced "tail"-structure in the photoresponse. This effect is explained by impact-reionisation from the lowest lying bound state, which acts as a rate determining step in the (cascade) relaxation process into the ground state [9]. Using an appropriate theoretical model [9], the relaxation time of this rate determining step could be deduced, consistent with results from saturation-absorption experiments [8].

3.2 General remarks concerning photoconductivity in semiconductors

Although far infrared (FIR) photoconductivity is a well known technique for shallow impurity studies of semiconductors, it is appropriate to make some general remarks *vis à vis* its restrictions and possibilities for application in the study of recombination dynamics. This will enhance the clarity of later discussion and will be presented before going into the detailed experimental results which are described in this chapter.

The principle of the photoconductivity effect is evidently the change of conductivity following absorption of light. To understand the mechanism of this effect, three main processes may be distinguished, and these are illustrated schematically in Fig. 3.1 [12]:

i) Intrinsic photoconductivity involves the optical excitation of an electron from the valence band (VB) to the conduction band (CB) of a semiconductor. Because of the creation of free electrons and free holes the conductivity of the sample is enhanced. This mechanism will only occur if the energy of the applied photons exceeds the bandgap energy of the semiconductor involved (eg. for GaAs $\propto$ 1.42eV), which in practice defines a long wavelength cut-off in the near infrared or optical region.

ii) extrinsic photoconductivity involves the presence of impurity doping in the semiconductor. In the experiments described in this chapter these impurities are considered to be weakly bound shallow donors which can be described by an hydrogen model. For low enough temperatures, where the uncompensated impurities are neutral, photoconductivity occurs through ionisation of such a neutral impurity. In the case of an n-type semiconductor this results in the excitation of the electron bound to the donor directly into the conduction band or to a higher excited bound state, followed by ionisation by photo-thermal or impact ionisation processes. Because the energy levels of such a bound electron lie within the bandgap of the semiconductor the long wavelength cut-off occurs at much longer wavelengths, which are normally in the FIR region (eg. for a Si-donor in GaAs $\propto$ 5.6 meV; wavelength $\lambda_{FIR} \propto 200\ \mu m$).

iii) free carrier absorption does not create a difference in the free carrier concentration of the semiconductor, but rather changes the carriers' mobility. By interaction with the incident radiation, electrons can gain energy ('heat-up') and exceed the equilibrium energy. Under the condition that the mobility is energy dependent (due to scattering or temperature dependence), the mobility is affected. This process starts at a wavelength of about 100μm, however it is most efficient at very long wavelengths greater than approximately 1000μm [12].

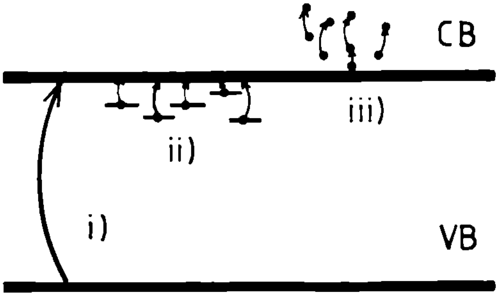

Fig 3.1 *Schematic diagram of different mechanisms for photoconductivity in semiconductors as discussed and numbered in the text.*

From the above arguments it is now clear that in photoconductivity measurements the observable is the change of the conductivity, $\Delta\sigma$, which can be written down as

$$\Delta\sigma \propto \Delta n \cdot \mu + \Delta\mu \cdot n \tag{3.1}$$

where μ is the mobility and n the free charge carrier concentration. For normal spectroscopic studies of energy levels in semiconductors with PC the only important feature of equation (3.1) is, in general, the change of carrier numbers (Δn). An exception is the study of the cyclotron resonance in PC which is a transition between two Landau levels. To a first approximation, which is valid for short pulse excitation, only the mobility is affected by changing the distribution (and not the number) of free electrons over the Landau levels [13].

Although equation (1) shows a dependence of the change of both the carrier number and the mobility, it is noted that for the theoretical description of the time-resolved photoconductivity experiments, presented in this chapter, no dependence of mobility change ($\Delta\mu$) has been taken into account. The most plausible reason for this approach is that the change in conductivity due to the photon pulses, $\Delta\sigma$, is several orders of magnitude which is much too big to be explained by the mobility change. A small additional influence of mobility, however, can never be excluded completely. In CW measurements even large changes in the electron mobility have been obtained by impurity excited photo-Hall experiments [15,16]. CW experiments can not be compared with pulsed experiments, however. The fundamental difference between CW and short pulse excitation is that as long as the excitation time (laser pulse) is smaller or equal to the decay time, only the energy levels involved in the transition are affected and the system is not in equilibrium. In CW measurements, however, the system under interest is always studied under steady-state conditions, where the occupation numbers of all energy levels involved are redistributed into a new equilibrium situation and where, due to the constant influence of radiation, free carriers may heat-up by means of free carrier absorption. Such an equilibrium situation is definitely not obtained as long as the duration of the short exciting pulse is shorter than the relaxation times of the levels involved. In such a case mainly the effects of higher concentrations of ionised impurity scattering centers (which lower the electron drift mobility) and the screening of the ionised impurities by the electron gas (increasing the mobility) could induce a difference in the mobility. Estimations of the mobility changes, taking both these effects into account, can be made by the formalism of Brooks and Herring which considers the mobility of an electron gas in thermal equilibrium. Application of this formalism is doubtful because thermal equilibrium for pulsed photoconductive experiments may not be available, although it is expected that the electrons thermalise within a fraction of a nanosecond. However, it shows that the mobility is only weakly dependent on the degree of photo-ionisation of the donors [14].

For these reasons mentioned, it is concluded that under the experimental conditions of moderate sample bias voltages and laser illumination intensities, the observed change of conductivity, due to short pulse excitation, is governed by the change in carrier concentration.

3.3 Hydrogen-like shallow donors in semiconductors

In the III-V material semiconductor GaAs a shallow impurity atom of the group IV, eg. Si, normally will fill in a group III lattice site. From four of its available valence electrons only three will bind to the lattice and the fourth electron will be bound by the Coulomb potential of the remaining uncompensated positive charge of the Si atom. Theoretically this is analogous to the Bohr model of the three-dimensional hydrogen atom, and therefore the impurity is often called hydrogen-like. To apply this theory to hydrogen-like impurities it is necessary to take into account the influence of the host lattice [17]. Firstly, m^* will be the effective mass of the electron at the bottom of the conduction band. Because the Rydberg (the binding energy of the electron to the hydrogen ion) is proportional to the free electron mass, m_0, as known from the real hydrogen atom [18], the effective Rydberg, R^*, (binding energy of the electron to the donor) will be very small, and consequently the effective Bohr radius, a^*, will be large. Therefore, the bound electron will have a Bohr orbit which contains a great number of unit cells, and as such the semiconductor crystal lattice may be considered a macroscopic dielectric, characterised by the dielectric constant, ϵ_r . The Hamiltonian of the hydrogen model for an impurity in a bulk semiconductor material can, therefore, be written as

$$H_{3d} = -\frac{\hbar}{2m^*}\nabla^2 - \frac{e^2}{\epsilon_0 \epsilon_r r} \tag{3.2}$$

and an effective Rydberg, R^*, as well as an effective Bohr radius, a^*, may be obtained, given by

$$R^* = (m^*/m_0)\epsilon_r^{-2} \cdot R \quad ; \quad a^* = (m_0/m^*)\epsilon_r \cdot a \tag{3.3}$$

It should be noted that in the case of a shallow impurity in a Quantum Well the confining potential of the barriers, $V(z)$, should also be taken into account and as such should be added to the above equation (3.2) [3]. The binding energy of an electron to a hydrogen impurity in a MQW exhibits considerable shifts from the bulk value when the three-dimensional effective Bohr radius approaches the well-width [3]. The limiting case for very thin QW structures results in a completely two-dimensional hydrogen model which will be commented on later. An alternative way to induce a confinement effect on the Hydrogen-like electron-donor system is by application of a magnetic field, which changes the Hamiltonian of equation (3.2), as is also discussed in the next sections.

3.3.1 Hydrogen-like donors in bulk GaAs

For normal bulk n-GaAs material, where $\epsilon_r = 13.1$ and $m^* = 0.067\ m_0$, equation (3.3) yields an R^* of 5.7 meV and an a^* of approximately 100 Å (compared with R=13.6 eV and a=0.5 Å respectively in the case of free hydrogen in vacuum). Following the hydrogenic analogy it is noted that the energy spectrum of the eigenstates is given by [17]

$$E_{nlm} = \frac{R^*}{n^2} \quad ; \quad n=1,2,3... \tag{3.4}$$

where *n,l,m* stand for the spectroscopic quantum numbers which identify the different bound states, eg. 1s, 2p, 3d etc. Here *n* is the principle quantum number of the energy state, *l* is the quantum number of the orbital angular momentum and *m* is the azimuthal quantum number describing the z-component of the angular momentum.

In principle there are infinitely many bound states for one single hydrogen atom. If selection rules are obeyed, it is possible for FIR photons to excite a ground state electron directly into the conduction band continuum or into another bound state. This results in an enhancement of the conductivity directly (for the former case) or (in the latter case) after further ionisation by photothermal or impact ionisation processes. In a real semiconductor sample however, the effective number of real bound states is not infinite due to a finite distance to the next donor site and the significant increase of the spatial extension of the higher bound states; overlap can occur with neighbouring bound states and as a result these states can no longer be be regarded as bound to one single donor. This spatial extension can be deduced from equation (3.2), resulting in the expectation value for the spatial extension of higher states [18]

$$\langle r\rangle_{nl} = \frac{1}{2}\, a^* \,[3n^2 - l(l+1)] \tag{3.5}$$

If impurity atoms are available in a semiconductor in concentrations such that even the ground state electron wavefunctions overlap (Mott-limit), an 'impurity band' is formed [19] in which electronic conduction may take place without recourse to the conduction band. For a semiconductor as n-GaAs (a^* = 100 Å) the critical donor density for this Mott-limit may be estimated at 10^{17} cm^{-3}.

The hydrogen model for the description of the impurities predicts all properties to be the same for all donors in a given material, independent of their chemical nature. Though, it is clear that the potential seen by an elec-

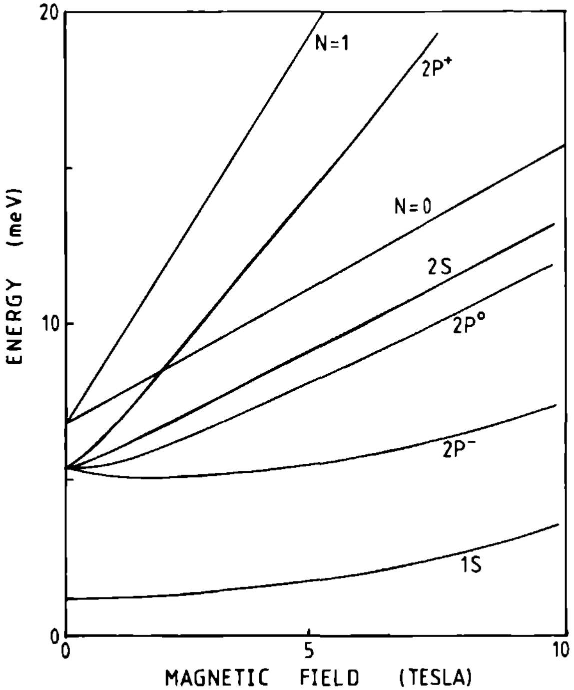

Fig 3.2 *Magnetic field dependence of the energy levels of some shallow donor bound states together with the lowest Landau levels, N=0 and N=1.*

tron close to the donor atom will not be the simple Coulomb potential. For shallow donors, with large Bohr radii, very little contribution to the binding energy comes from the potential at values of r less than a lattice spacing. Individual impurities, however, can be identified using FIR techniques [1] due to central cell corrections. These effects, however, do not directly relate to the scope of the present work and will not be considered further.

In the presence of a magnetic field, an additional field term is inserted in the Hamiltonian of equation (3.2) and for the resulting eigenstates the zero-field degeneracy in the angular momentum quantum numbers l and m (equation (3.3)) will be lifted. This problem has been studied using numerical [20] and variational methods [21] resulting in magnetic field dependent bound state energy levels as is shown in Fig. 3.2 for several different states. The increase in binding energy at increasing magnetic fields can be explained by the increased localisation of the wave functions around the impurity center. The influence of this confinement effect on the relaxation mechanisms will be discussed in due course.

In an experiment where the wavevector of the radiation is parallel to the magnetic field, **B**, (i.e. the Faraday configuration) the selection rules for electrical dipole transitions are $\Delta m=\pm 1$; l=odd. Therefore, the most prominent line observed in photoconductivity spectra at low temperatures corresponds to transitions from the 1s donor ground state to $2p^{+}$ exited state. This transition is experimentally very easy to observe in pulsed photoconductivity measurements in both bulk samples and multi quantum wells, and therefore it was used for the time resolved measurements which will be described in this chapter. Figure 3.2 also shows the two lowest Landau levels. Optical transitions are possible between Landau levels and between the bound states if the selection rules are obeyed.

It should be noted that in FIR photoconductivity spectra of hydrogen-like shallow donors in high purity GaAs epitaxial layers, spectral features have been observed [22,23] which could not be identified by (n,l,m) states; it has been concluded that these features are due to excitation of metastable states from the ground state. These metastable states arise in a magnetic field out of the donor continuum and do not correspond to donor bound states in the zero field limit [23,24]. Because these states only exist at energies above the lowest Landau level, they do not interfere with the present photoconductive relaxation model, which only includes bound states with energy lower than this Landau level.

3.3.2 Hydrogen-like donors in multi quantum wells

As previously mentioned, the confined shallow donor impurity in a multi-quantum well (MQW) presents a different case to the shallow donor in a simple bulk material because of the (quasi) two-dimensionality of its host lattice. The amount of two-dimensionality varies as the ratio of the QW length (L) to an effective Bohr radius (a^*) is changed: Theoretical studies, using a variational [3,25] or numerical [26] approach, have been performed, indicating that the binding energy for an on-center donor varies from the bulk effective Rydberg (R^*_{bulk}) at $L/a^*_{bulk} >> 1$, to a value of $4 \cdot R^*_{bulk}$ at L=0 for a confining potential with infinite potential barriers [27]. This latter case is of course exactly analogous to the two-dimensional hydrogen model, where infinite barriers ($V(z)=\infty$ in equation (3.1)) are used. (However, for finite barrier heights ($V(z)=V_0$), the theoretical predictions for the binding energy revert to three-dimensional values as the heights of the potential barriers approaches zero. The effective Bohr radius is also reduced by a factor of two between the $L/a^*_{bulk} >> 1$ and $L = 0$ limits. The physical reason for this change in binding energy is that for an impurity at the well center, the electron on average is forced to be closer to the attractive positive ion; therefore the binding energy increases with decreasing well width. This argument also explains the reduction of the effective Bohr radius, which is a very important parameter in the problem of the electron-impurity relaxation mechanism, as will be discussed later. Another important feature of binding energies of impurities in QWs is that for a finite well width the binding energy is found to decrease as the impurity is moved away from the center towards the edge of the well. In the limit the binding energy tends to $R^*_{bulk}/4$ for an interface located donor. A "handwaving" argument for this effect is that, as was mentioned above, for an impurity at the well-edge the electron is forced to be further from the attractive positive ion; in the ultimate situation the impurity is moved into the barrier while the electron remains in the well. All these effects predicted by theory have been examined using far infrared photoconductivity and transmission measurements in silicon-doped GaAs/AlGaAs MQWs, and generally good agreement is obtained [4,28].

Application of a magnetic field to such donor doped QW system was also theoretically considered in the context of FIR photoconductive response studies [29] and transmission measurements [30], where the field dependence of the transitions generally behaves like their bulk counterparts, although with an additional energy off-set caused by confinement, as is shown in Fig. 3.3. However, because the wavefunctions become more localised about the impurity center as the magnetic field increases, this quantum well confinement becomes less important (see Fig. 3.3). To confirm that the transitions come from the well structure (and not from the underlying substrate) the measurements used to achieve the results shown in Fig. 3.3 were also performed in tilted fields, thereby showing clear two-dimensional effects (see section 3.5.3 Fig 3.10).

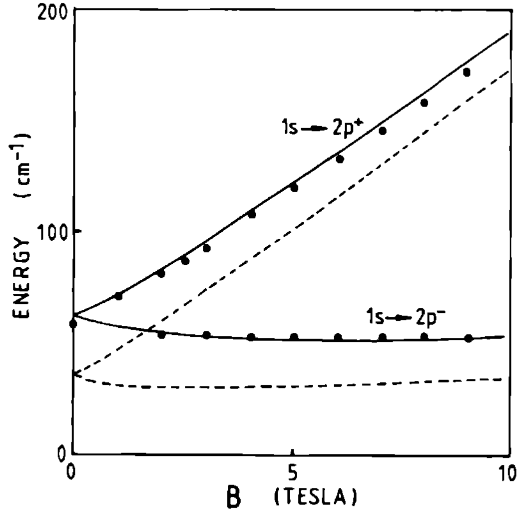

Fig 3.3 *Energy of $1s$-$2p^+$ and $1s$-$2p^-$ transitions for a center-doped 150-Å well (sample #6 ; GaAs/AlGaAs ; $a^*_{QW} \simeq 56$ Å ; $R^*_{QW} \simeq 10$ meV) as a function of magnetic field, B. Experimental data are indicated by solid circles. The solid line is calculated following Ref. 31. The broken line indicates the energy of the corresponding transitions as observed in n-doped GaAs bulk samples.*

3.4 Recombination mechanisms for photo-ionised shallow donor systems

3.4.1 Survey of possible processes

Recombination occurs through capture of free electrons into highly excited bound states, followed by a cascade to the impurity ground state. The dominant mechanism occurring in the cascade process is acoustic phonon emission [6], although Auger-type mechanisms [32] and photon emission [33] are other possible channels for energy relaxation. Re-excitation mechanisms [9] may also occur if the experimental sample is subjected to a high bias voltage or high FIR intensities or high temperatures due to respectively impact or thermal ionisation of very shallow bound states. The relative importance of these mechanisms has not been completely determined, but it is generally accepted that radiative recombination is relatively inefficient [7]. The theory of shallow donor recombination processes was first set down classically by Lax [7], who describes the capture of an electron in a Coulomb potential under emission of a cascade of phonons. A review of other theoretical studies has been given by Brown and Rodriguez, who first provided a quantum mechanical description [34]. These authors describe a recombination cross section of a conducting electron, having a spherical mass m^* and a donor impurity which is hydrogen-like. Recombination occurs with the initial capture of a conducting electron in an excited donor state (not necessarily highly excited) followed by successive transitions to lower lying states, with emission of a single acoustic phonon for each such transition.

The characteristic time scales of the phonon-assisted recombination processes are in the nanosecond or tens of nanoseconds region. FIR saturation-absorption [8] and FIR free-electron laser saturation-photoconductance studies [35] (as will be considered later) of GaAs have established that in a magnetic field the lowest excited bound state, $2p^-$, is long lived (typically 500 ns). This state may act as a bottleneck in de-excitation processes, as has been discussed for InP by Chamberlain et al. [9]. Early evidence for the presence of such long lived states was also obtained by Ohyama in InP [36], Brown et al. in GaAs [37], Muro et al. in Ge [38], and Müller et al. in InSb [39]. These workers used either electrical pulse excitation or CO_2 laser pulse excitation techniques.

The dynamics of recombination transitions in a magnetic field are often described by rate equations representing the filling and emptying of the levels involved. In saturation-absorption experiments, where steady-state behaviour is approached, these can be solved. Fig. 3.4 shows a conceptual diagram to illustrate the transition rates used in such a rate-equation treatment.

For a magnetic field of about 3 Tesla, the $2p^+$ state is at a higher energy than the N=0 Landau level (see Fig. 3.4). After resonant excitation of an electron from the 1s state into the $2p^+$ state two options are available

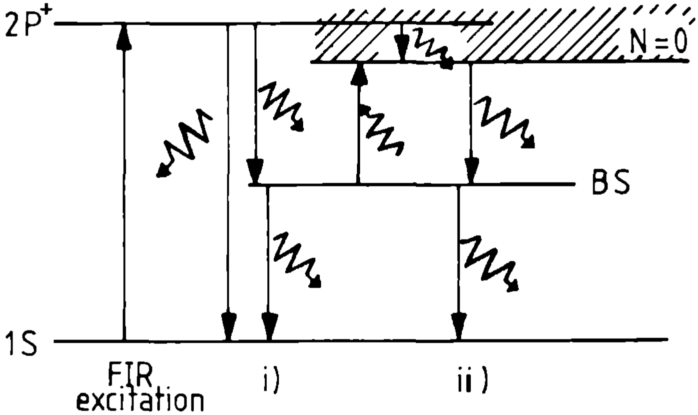

Fig 3.4 *Schematic representation of transitions between impurity and Landau levels for resonant 1s→$2p^+$ excitation for a magnetic field of about 3 Tesla. BS represents a generalised bound state. Phonon absorption and -emission is indicated. Transitions are indicated as described in the text.*

to relax back to the ground state: *i)* The electron can relax to the ground state of the donor where it is bound to in the $2p^+$ state. Such an electron will not be free and as such will not participate in the conduction. *ii)* The electron may be ionised by impact ionisation or phonon emission (absorption in the case of lower magnetic fields) into the N=0 Landau level. This electron will take part in the photoconductive process and after a certain time it will recombine after capture by a donor. The relative importance of both options are not clearly determined. However, a "controversy" is noted concerning the time scales involved in the latter process. Rikken et al. [10] using long-pulse FIR excitation (50 ns pulses with a quite well controlled fall, but not rise, characteristic) in InP, have concluded that the rate of entry into the N=0 Landau level from the resonantly pumped $2p^+$ state is fast (i.e. < 1 ns). This is in contradiction to the conclusions of Allan et al. [8], who deduce a $2p^+ \rightarrow$ N=0 lifetime of approximately 30 ns in GaAs to be the fastest relaxation process from the $2p^+$ state. The main reason to assign this relaxation time of

30 ns to the $2p^+ \rightarrow N=0$ transition and not to the recombination from the N=0 into a bound state was its independence of the acceptor concentration, N_A, which is expected to have an important influence on the latter process, as will be explained in the next section. Considering this argument, no possible recombination time smaller than this 30 ns would be measurable using TR-PC techniques, which is in contrast to the data presented furtheron in section 3.6. Additionally it is noted that these data (shown in section 3.6) do show the expected N_A dependence. Therefore, it is concluded that the $2p^+ \rightarrow N=0$ rate is very fast and that, as a consequence, the relaxation of the PC is only influenced by the recombination of the electrons to ionised donors.

3.4.2 Rate equations

To describe the change in time of the free charge carrier concentration, n, one can write down the rate equation [40]:

$$\begin{aligned}\frac{dn}{dt} = \; & A_T(N_D - N_A - n) + A_I n(N_D - N_A - n) + A_O(N_D - N_A - n) \\ & - C_T n(N_A + n) - C_I n^2(N_A + n) - C_O n(N_A + n) \qquad (3.6)\end{aligned}$$

where the first three terms on the right-hand side represent generation rates and the last three are recombination rates. N_A and N_D stand for the concentration of acceptors and donors respectively. The concentration of neutral donors from which free electrons can be generated at low enough temperatures, is written as $(N_D - N_A - n)$, and $(N_A + n)$ stands for concentration of recombination centers (i.e. the amount of ionised donors). The A_T-term is the rate of thermal generation by phonons from the crystal lattice vibrations, the A_I-term is the generation rate due to impact ionisation by other free charge carriers, and A_O is the rate parameter for the optical generation processes. The C-terms represent the corresponding recombination processes. Thus, C_T is the recombination rate parameter for which the excess carrier energy is reduced by emission of phonons into the crystal lattice, the C_I-term is the rate involving transfer of energy to other free charges (Auger effect) and the C_O-term represents the emission of photons.

To a first approximation all excitation parameters may be considered to be zero under moderate experimental conditions. This is because at low temperatures and electric fields the kinetic energy of the free electrons will be insufficient to ionise the impurity atoms [10]. For non-moderate experimental conditions, effects as thermal ionisation or electric break-through become important which is beyond the scope of the study presented here. For moderate conditions, though, all optical rates are considered too small to play a role of any importance. The C_I parameter will also be small, because for the Auger effect the two free electrons involved should interact at one impurity site and as such should be available simultaneously; under the condition of moderate donor concentration this is considered unlikely. The resulting equation for the description of the recombination rate for free electrons may now be written as:

$$\frac{dn}{dt} = - C_T n \left(N_A + n\right) \tag{3.7}$$

with a solution, considering n_0 as the initial electron concentration,

$$n(t) = \frac{N_A}{(1+ N_A/n_0)\cdot e^{(C_T\ N_A)t} - 1} \tag{3.8}$$

which can be approximated, for very low initial free electron concentrations ($n_0 << N_A$), by

$$n(t) \simeq n_0 e^{-(C_T N_A)t} \tag{3.9}$$

with a typical relaxation time $\tau = 1/(C_T N_A)$. As has already been discussed in section 3.2, this decay of the free electron concentration can be monitored by measuring the conductivity as a function of time after the FIR stimulus has stopped.

Note that equation (3.6) only considers the two level model of a conduction band and a bound state. In reality there are more bound states involved with different binding energies and different physical extensions, which could in principle affect the dynamical behaviour to the impurity system. Rikken et al [5,32] considered this problem under the assumption that *i)* the dominant recombination process is phonon emission , *ii)* the dominant generation process during decay is impact ionisation and *iii)* that the inter bound state transitions do not affect the free carrier concentration. These authors recovered the same non exponential-like behaviour as in equation (3.8) (for which impact ionisation and the presence of many bound states has been neglected). Both these effects, however, were expected to show up in the value of the decay time, τ, and its dependence on electric field. Nevertheless, it was stressed that quantitative reliability of the parameters, to be determined by the experimental results, was not guaranteed [41].

Equation (3.8) therefore was used to interpret the present experimental data and to yield recombination times which depend only on the acceptor concentration, N_A, and the rate parameter C' which is mainly governed by the (phonon) rate parameter C_T. It is noted that in this C' also A-terms (generation rate parameter) are mixed-in and that, therefore, C' is considered proportional to an "effective" capture cross section.

3.4.3 Cross section dependencies

A number of experimental parameters have been found to affect the measured recombination rate (τ). In addition to the macroscopic N_A dependence, which may be deduced from equation (3.6) in the previous section, τ is dependent on the rate parameter C' as follows from equation (3.9). This C' is proportional to an "effective" capture cross section which is governed by microscopic factors, as there are the physical extension of the impurity system itself, the sticking probability through electron-phonon coupling [53], or the re-ionisation probability. These microscopic factors may be influenced by sample bias voltage, incident laser intensity, sample temperature and magnetic field. These dependencies will now be discussed:

i) Sample bias-voltage can affect the recombination dynamics via impact ionisation [42] from the bound states and by Auger processes, when electron kinetic energies are increased [32]. In addition, changes in sample mobility may occur at high bias fields (heating effects) which change the shape of the photoresponse profile.

ii) The laser intensity might be expected to affect the free carrier mobility by free carrier absorption during the actual illumination period, also resulting in changes in the measured photoresponse profile [15,16].

iii) A square law dependence on temperature of the cross section for the capture of a conducting electron in a stationary state, due to increased thermal ionisation has been predicted using the principle of detailed balance [35] (This dependence has also been observed experimentally and will be commented on in section 3.7.1).

iv) Magnetic fields may be expected to influence the recombination process, since the effective cross section depends on the matrix element of the electron-phonon coupling Hamiltonian (H_q), between the initial i (conduction band) and final f (bound) states; these states are both influenced by the magnetic field. The transition probability ($W_i^{f,q}$) between these initial and final states by means of the accoustic phonon q (with energy E_q and frequency ω_q) can be calculated, using Fermi's Golden Rule:

$$W_i^{f,q} = \left(\frac{2\pi}{\hbar}\right)|<f|H_q|i>|^2 \, \partial(E_i - E_f - h\omega_q) \qquad (3.10)$$

Using this argument, this problem has been investigated in considerable detail by Toombs as described by Rikken et al. [10]. It has been shown that for a particular transition in a magnetic field (e.g. N=0 Landau level to the $2p^-$ state) the transition rate, Γ, is of the form

$$\Gamma = Dq^n \exp(-2a^2q^2) \qquad (3.11)$$

where D is a material constant (involving inter alia the deformation potential) and a is a characteristic wavefunction dimension of the order of the Bohr radius; n is about 2; q is the optimum wavevector for the acoustic phonon emitted in the transition. The expression (3.11) will have a maximum when $q^2 = 1/2\ a^{-2}$. Since the wavevector and energy of an acoustic phonon are related by the dispersion relation:

$$E = q\hbar v_s \qquad (3.12)$$

where v_s is the velocity of sound ($\simeq 10^5$ m/s), the energies of the participating phonon may also be determined (0.5-1 meV). The effect of increasing magnetic field will be to reduce the characteristic length parameter a. Estimates of this effect have been given as a reduction of 67 % for this characteristic length parameter in GaAs at 10 T [43]. The implications of this are considered in section 3.7.

In the present experiments the observed recombination time represents transitions from the conduction band to a number of bound states. The observed transition rate is therefore a weighted average of expressions such as (11), which thus may be written as

$$\Gamma = D'q^2\exp(-2a^2q^2) \qquad (3.13)$$

where the parameter D′ includes not only the material constants and characteristic lengths, but also involves a weighted average over all the participating transitions.

v) Quantum confinement (explained in section 3.3.2), in principle, is expected to affect the capture cross section (and as such the recombination time) the same way as the magnetic field confinement.

3.5 Time resolved measurement of photoconductivity

In the preceeding sections an idea has been given about the typical features of shallow donors in semiconductors and also the possible mechanisms of recombination and their dependence on different parameters. Many techniques are available for the experimental study of these effects, however time resolved photoconductivity is the most direct means of probing recombination processes in the different sample structures reported in this thesis.

3.5.1 Experimental methods of investigation of recombination processes

To investigate the recombination processes in shallow donor semiconductor systems there are several different experimental approaches available. One common necessity in these experiments however is the excitation of the electrons bound to donors into higher excited states or free carrier states. One method is the application of electrical pulses with high enough voltage to be able to impact-ionise all bound-to-donor electrons. Recombination is measured through optical detection of radiative recombination [33]. A second method is to use FIR optical excitation techniques. This technique of course has the advantage that photon energies are used which are just about equal to the ionisation energy of the impurities. This makes it possible to create a relatively cold electron gas which cannot be realised using electrical techniques, where hot electron effects introduce additional complications (for example, a possible increase of Auger recombination efficiency). The most widely used experiment to investigate recombination processes is by saturation-absorption or saturation-photoconductivity; in these experiments the saturation intensities are measured for an individual excitation by means of probing the transmission or photoresponse of the system involved. By means of the principle of detailed balance the rate equations involving all the participating bound and free state levels can be solved and the individual relaxation times can be deduced. The FIR powers necessary for these measurements normally can only be reached by pulsed sources. However to apply the detailed balance principle correctly the steady-state condition should be satisfied, and as such the applied FIR pulses should have a duration which is longer than the slowest process that is involved in the relaxation mechanism (i.e. in GaAs $2p^- \rightarrow 1s \simeq 500$ ns). This problem was overcome by Kaminski et al. who used a Free Electron Laser source [35] and who recognised that the use of too high saturation powers could lead to erroneous results.

Time resolved photoconductive studies are, therefore, a direct way of measuring the recombination process from the free carrier level. The information about the individual bound levels is not completely clear, however the response shapes can give information about such (dynamical) aspects of the free carriers themselves as heating, impact ionisation, etc.

3.5.2 Photoconductivity measurements

In a typical photoconductivity experiment the change of the sample's conductivity is a few orders of magnitude. Under normal operating conditions the sample impedances are very high, between $10^5\Omega$ and $10^{10}\Omega$, depending on the type of sample (bulk or quantum well), the type of contacts (eg. Indium-dots or interdigitated patterns), the strength of the applied magnetic field (which may induce magnetic freeze-out), and also on the sample temperature and the presence of background radiation (such as bandgap light from an LED). During the photoconducting process these sample impedances may ultimately decrease to the order of a few kΩ or less. For CW measurements the high impedance conditions of the measurements are not of vital importance. However, to perform fast response measurements with nanosecond resolution involving the generation and recombination of electrons in such high impedance systems it should be noted that all electronics which must operate in the GHz regime are standarised to 50Ω matching conditions. It is essential that great care is taken over the design of the necessary circuitry in order that meaningful conclusions may be drawn about the behaviour of the sample under investigation.

Consider a practical detector circuit consisting of a battery and a load resistor, R_l, in series with the photoconductor, $R_s(t)$, as is shown in Fig. 3.5. Under normal conditions a current (dark current) flows through the circuit, because of the finite resistance of the photoconductor. As the FIR photon flux is modulated either by using a chopper blade (in cw. measurements) or by applying pulses, the photocurrent can be distinguished from this dark current through the AC-coupling (by means of capacitor C_c) of the detector circuit to a preamplifier by either measuring the voltage over R_l or $R_s(t)$. The input impedance of this amplifier is described by R_a.

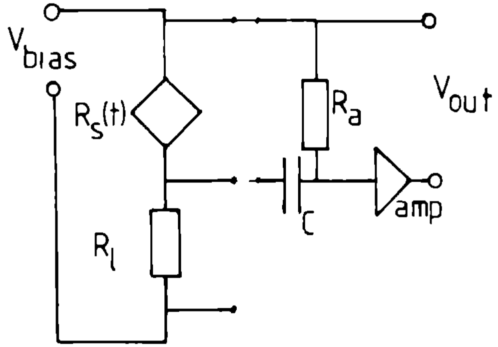

Fig. 3.5 *A typical circuit for photoconductive measurement, for details, see text.*

Generally there are two different arrangements of parameter settings to measure the photoconductivity: (a) 'constant' current through the sample and (b)'constant' voltage over the sample. This latter option is favourable for dynamical studies because free electron energy and drift-speeds will be kept constant during measurements. Both options, however, will now be considered.

(a) *'constant' current:* $R_s(t) < R_l$; the DC-current through the circuit will now be kept constant by the high value of load resistor R_l. A relatively big change in the voltage over the sample (of a few orders of magnitude) will occur, resulting in completely different energies (and hence dynamics) for an individual free electron during the illumination period. The change in voltage over the sample ($R_s(t)$) under constant current conditions now can be measured by the AC-circuit in the case of a high valued R_a. For low values of R_a, however, which are necessary to achieve matching conditions (50Ω) in the present time resolved measurements, the constant current conditions will not be satisfied any longer, because capacitor C_c will try to keep the voltage over the sample constant. As a consequence, the effective AC-measuring circuit (C_c, R_a, R_s) should now be regarded as a 'constant' voltage circuit in which the high valued R_l does not have any influence. This circuit now (C_c,R_a,R_s) is analogous to a circuit in which the voltage is measured over a low valued R_l. Such a circuit, however, is in principle characterised as the second arrangement of parameter settings for photoconductivity measurements:

(b) *'constant' voltage:* $R_s(t) > R_l$; the DC-voltage over the sample will now be kept constant because of the very low value of the load resistor R_l. In this case a relatively big change in current through the circuit (of a few orders of magnitude) will occur, thereby keeping the electron drift-speeds (and also the energy of the free electron) nearly constant, which is preferable for studies of the dynamics. In such an arrangement the signal strength is governed by the bias voltage over the sample and is proportional to the ratio of the load resistor R_l and the detector impedance. If the load resistor R_l = 50Ω, the system is matched to the 50Ω impedance of the electronics and the response time of the circuit is as fast as about 1 nanosecond, only limited by RC-times due to cable impedances and high frequency limits of the electronic equipment involved. Improvement of the signal strength evidently can be realised by either increasing the voltage or the ratio between the impedances. Increasing the bias voltage should be avoided because it affects the mechanisms of photoconductivity, and therefore can be applied as a measuring parameter for the study of the sample. As a consequence, the resistance ratio should be increased, which can be obtained by either using *i)* higher resistances than the standard 50Ω and/or *ii)* decreasing the sample resistances. Let us now consider these effects:

Improvement in signal strength by changing the load resistor R_l.

If R_l is adjusted, two significant factors must be considered. These are:

1) Proportionality of the measured voltage signal to the inverse sample resistance.
2) Impedance matching to the 50Ω circuit without loss of high temporal resolution including a JFET amplifier.

1) The first requirement of the proportionality of the measured voltage to the inverse sample resistance states that care should be taken in the analysis of the experimental data if R_l is equal to or greater than the resistance of the sample whilst it is photoconducting. Considering the signal voltage as

$$V(t) = \left(\frac{V_0}{R_l+R_s(t)}\right)\cdot R_l \tag{3.14}$$

where V_0 is the bias voltage, it is clear that in the case, as mentioned above, the 'constant' voltage approximation is no longer valid and the measured signal voltage can no longer be interpreted as inversely proportional to the resistance of the sample, because the influence of R_l in the denominator of equation (3.14). To illustrate the effect of the R_l-value on the time-resolved signal response, a simulation of V(t) was performed for an arbitrary photoconductor, $R_s(t)$, with a dark resistance of 1 MΩ and a photoconducting resistance of 500 Ω and with an R_l of 50Ω, 500Ω, and 5000 Ω respectively, as is illustrated in Fig. 3.6. In this simulation with an arbitrary relaxation time, τ=10 ns, the resistance during the photoconductivity process is assumed to be inversely proportional to the free electron concentration. Therefore $R_s(t) \propto 1/(n_0+n_1(t))$, where n_0 is defined by the dark resistance and $n_1(t)$ by equation (3.9). For clarity, all curves are normalised to unity at the beginning of the relaxation process. It is evident that the absolute values of the signal strengths show an electronic saturation effect, as shown in the inset of Fig. 3.6; in reality, the difference in signal strengths between the R_l=50 Ω and R_l=500 Ω curves (at time=0) is about a factor of five (use equation 3.14), whereas for the 500 Ω and 5000Ω curves this ratio is only a factor of two.

2) The second requirement concerns the impedance mis-matching, if $R_l \neq 50$ Ω, with the 50 Ω lines and electronic data retrieval equipment, thereby inducing reflections and high frequency noise and possibly deforming the original pulse signals. To solve this problem the electronic circuit was equipped with an active cryogenic device consisting of a source-following Silicon Junction Field Effect Transistor (Si-JFET). In such an arrangement this

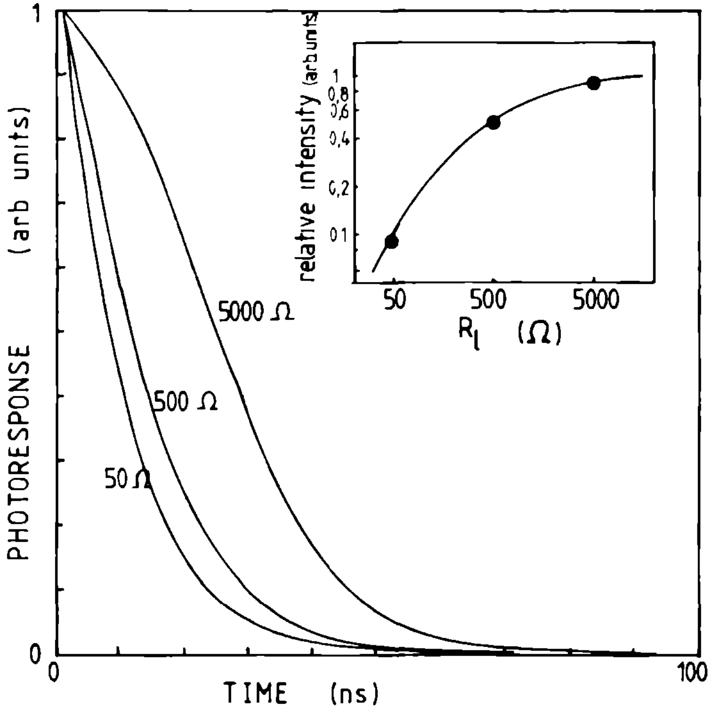

Fig 3.6 *Signal simulation using different R_l values, as discussed in the text. The inset shows the signal strength dependence of R_l.*

device behaves as a current amplifier which measures the voltage over the higher valued R_l and transfers this voltage to 50Ω by adjusting the current through it. Normal Si-JFETs have to be maintained above about 100K because of carrier 'freeze out'. However, certain manufacturers [44] obtained devices, operating also in liquid Helium environment and even up to magnetic fields as high as 22 Tesla. The devices used (Thomson 2N4416) did not have to be started with a heater resistor and were operational down to 2K. The non-dependency of carrier 'freeze out' may have its origin in very high doping or very effective thermal shielding. It is noted that for magnetic field operation above 5 Tesla the orientation of the field axis was of importance, probably because of the quasi-two dimensionality of the JFET.

The electronic circuitry which was used is shown in Fig. 3.7. The output impedance of the source follower varies roughly as 1 / g_m, where $g_m \equiv \Delta I_d / \Delta V_{gs}$ is the transconductance and *s,d,g* stand for the source, drain, and gate of the JFET. At about 4 K and 10 mA, the output impedance is around 50Ω and the gain of the follower is slightly less than unity. This has been confirmed by pulse response tests, applying electrical pulses to the system (of duration between 0.5 - 100 ns); no interference effects nor reflections due to mismatching were detected, which would have given an increase in noise dependent on the length of the coaxial line between the cryogenic circuit and the (room temperature) data acquisition system. A more detailed discussion on cryogenic amplifiers is given in [45] and references quoted therein.

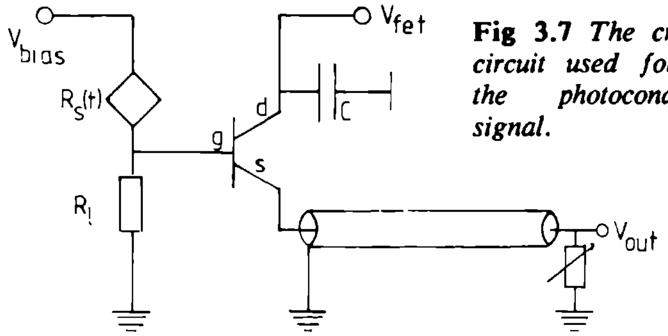

Fig 3.7 *The cryogenic electronic circuit used for improvement of the photoconductive response signal.*

The frequency limit of this circuit however, will be RC limited with R being the load resistor and C the sum over the detector capacitance the capacitance of the wires and the input capacitance of the JFET. This latter capacitance dominates, and in our case is about 2.5 pF. To resolve decay times smaller than 1 ns it is obvious that RC times must be smaller than 1 ns, which results in a value of R $\simeq$ 400Ω. This gives a gain in signal compared to a normal 50Ω load of rather less than one order of magnitude. The use of R = 1kΩ or more clearly affected the time resolution of the circuit response.

Improvement in signal strength by decreasing the sample resistance.

In order to use this as a means of improving the signal, it should be understood that resistivity is measured in Ωcm so that the sample resistance can be reduced by reducing the intercontact distance or by using greater area contacts. Through the use of interdigitated contact patterns (see Fig 3.8) it was possible to reduce the resistances of the samples by a few orders of magnitude. This resulted in minimum sample resistance under maximum FIR illumination of the order of less than 1 kΩ.

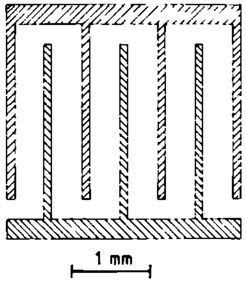

Fig 3.8 *Typical pattern of an interdigitated contact as used for most of the MQW samples*

Considering the discussion in (*i*) above about signal shape deformation due to equally-valued load and sample resistances it is noted that here again care should be taken in interpreting the experimental data. As the inter-contact distances are reduced in order to decrease the sample resistance the possibility of a feature known as 'carrier sweep-out' should be also taken into account [46]. This occurs when the free carrier drift length is comparable or greater than the distance between the electrodes of the contacts; all carriers will then be swept out of the element, leaving behind a uniform distribution of excess ionised acceptors. This space charge would give rise to a nonuniform electric field component which adds to the external bias field already present. In the experiments presented here, however, an estimation of the drift velocity at zero field of about 100 m/s ($=1\mu$m/ns) will result in a net drift which is far less than the contact distances applied.

Finally, to be able to study the recombination of electrons to ionised donors by time-resolved photoconduction the signal from the FET amplifier was captured by a fast digital storage system (Tektronics 7912 AD transient analyser) which was also used to average the transient photoresponse up to 1000 laser pulses if neccessary. In Fig. 3.9 the experimental configuration is shown. For the optical excitation of the bound electrons a FIR pulse (duration $\simeq$ 7 ns) was used, generated by the cavity dump laser as was described in the previous chapter. Optical switching elements could also be applied for additionally shortening this FIR stimulus. The magnetic field was applied to match the magnetic field dependent transition energies with the FIR photon energies. To achieve resonance conditions the PC signal was time-integrated by means of a boxcar integrator which output signal could be plotted against the magnetic field while this was scanned. Applying this technique makes it possible to distinguish between signals from impurity level resonances and background signals and, additionally, to obtain information of their relative importance, for instance, as a function of applied FIR intensity.

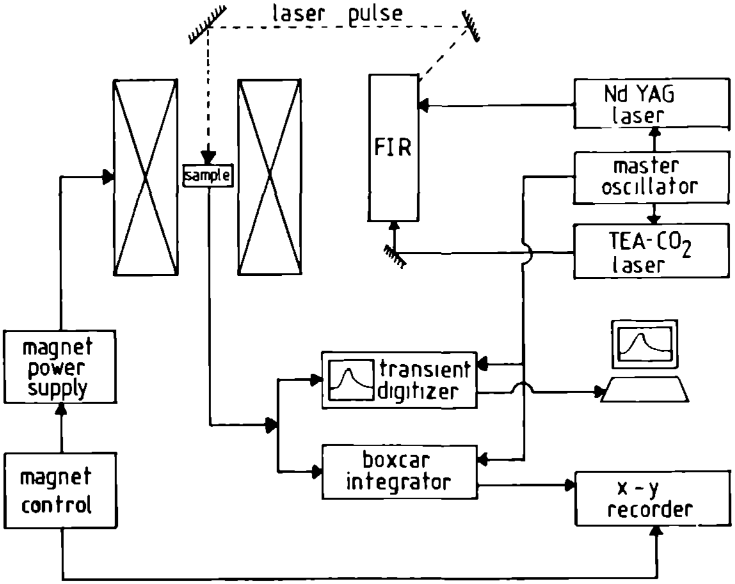

Fig. 3.9 *Experimental arrangement consisting of the FIR dump laser and a superconducting magnet providing field up to 10.5 T.*

3.5.3 Samples

The samples used for the experiments were all grown by MBE techniques except sample #3, which was grown by MOVPE. All samples were grown on a (100) semi-insulating (SI) GaAs substrate. The (intentional) doping of all samples was n-type, using Silicon (Si) as dopant. The electrical properties of these samples are listed in Table I. The samples may be divided into three groups:

i) Homogeneously Doped Bulk (HDB): Samples #1, #2, and #3 were grown with different doping levels under the condition that the impurities were distributed homogeneously through the sample. It is noted that for sample #1 and #2 very clear D^--effects were obtained in their magnetic field sweep CW FIR response [47]. This effect shows the very weak binding of an electron to a neutral donor (which already has one electron bound). The increased probability for a second electron to bind is expected to interfere with the relaxation process and therefore will be taken into account in the interpretation of the relaxation data from these samples.

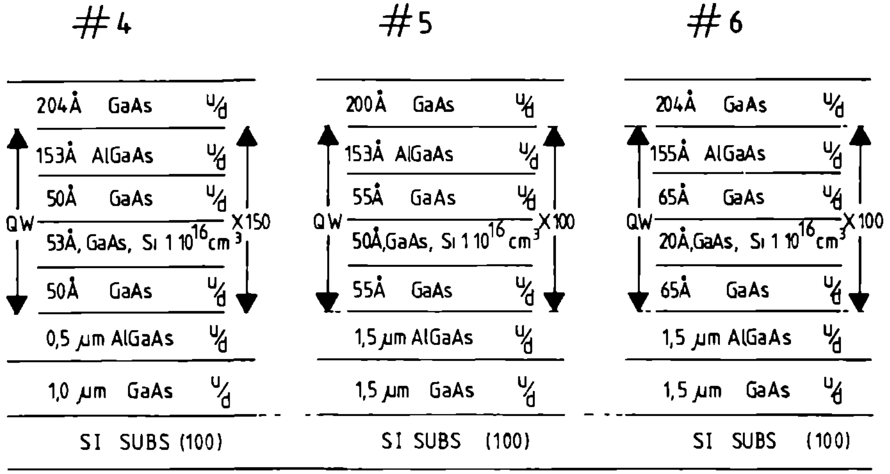

Fig 3.10 *Growth diagrams of the MQW samples showing the structure of the layers : a) #4 ; b) #5 ; c) #6. u/d indicates no intensional doping.*

ii) Multi Quantum Well (MQW): Samples #4, #5, and #6 are grown with the layer sequences shown in Fig. 3.10. The typical width of the wells was 150 Å which is approximately equal to the width of the $Al_xGa_{1-x}As$ ($x \simeq 0.33$) barriers: the central 50 Å of samples #4 and #5 (central 20 Å for #6) was doped with silicon to an approximately equivalent concentration of $1 \cdot 10^{16}$ cm^{-3}. All layers were grown on a relatively thick n-GaAs buffer layer (1-2 μm) and with an additional 1500 Å AlGaAs region between the MQW structure to prevent an unwanted FIR photoresponse from the (bulk) high quality n-GaAs buffer region. Sample #4 has 150 wells and samples #5 and #6 were grown with 100 wells. A thin (≃ 200 Å) GaAs top-cap was put on top of the QW structure to assist contacting and to prevent sample degradation. The great number of QWs reduces the significance of any possible band bending effects (due to surface charges) in the first few wells. MQW samples with only 30 wells were also grown and these were equipped with a 1500 Å layer between the QW structure and the top-cap to prevent this same effect. However, this additional layer increased the problem of obtaining good contacts; results on these wells were consistent with the present samples #4, #5, and #6, but will not be reported in this thesis.

iii) Sheet Doped Bulk (SDB): The bulk sample #7 was grown to mimic the two dimensionality of the doping structure of the MQWs in order to study the influence of this structure on relaxation times. Therefore #7 was grown with an identical structure to the MQW sample #5, but omitting the AlGaAs barriers and using the same undoped GaAs material as used for the wells.

Table I: *Electronic properties of the samples.*

Sample type	#	μ (77K) (cm^2/Vs)	N_D-N_A (cm^{-3})
HDB	1	$220\cdot10^3$	$2.8\cdot10^{13}$
HDB	2	$180\cdot10^3$	$5.0\cdot10^{13}$
HDB	3	$47\cdot10^3$	$3.0\cdot10^{14}$
MQW	4	$60\cdot10^3$	$8\cdot10^{15}$
MQW	5	$60\cdot10^3$	$8\cdot10^{15}$
MQW	6	$60\cdot10^3$	$8\cdot10^{15}$
SDB	7	$60\cdot10^3$	$8\cdot10^{15}$

The electrical properties of the HDB samples as shown in Table I were determined by Hall-effect measurements in a homogeneous magnetic field up to 0.75 T using a gas-flow cryostat with careful monitoring of sample temperature. The controlling software for the system also performed a self-consistent correction to allow for both substrate and surface depletion effects [48]. The N_D-N_A values presented in Table I are obtained from a best fit to the corrected mobility data using the procedure of Anderson and Aspley [49]. In the case of the MQW and SDB samples, the N_A and N_D and mobility data given in the Table relate to the silicon doped GaAs regions. These values were established by using the above procedures to test layers of GaAs grown under nominally identical MBE machine conditions.

To ensure that the photoresponse of the MQW samples was indeed confinement-related, additional cw measurements were done with the MQW growth direction at an angle $\theta = 19^0$ to the magnetic field. It is well known that spectral features of a two-dimensional electron gas with field parallel to the confined direction will be be observed under tilted field conditions at a field of $B/\cos\theta$. Figure 3.11 shows the field-tilting dependence of the 1s-2p$^+$ transition of sample #6 under 70.6 μm FIR illumination. At $\theta = 0^0$ the resonance is at 5.75 T and at $\theta = 19^0$ the resonance has shifted to 6.09 T $\simeq B/\cos\theta$ (=6.08 T). The effective Rydberg R^* for this MQW was determined to be 10.1 meV.

The anisotropy of the SDB sample #7, expected on grounds of the sheet structure, was confirmed by the field-tilting dependency of the cyclotron resonance (CR) linewidth. This effect is assumed to rely on the variation with angle of the scattering probability (and thus the CR linewidth and lifetime) as the electron moves through the sample with a spiral motion along the field direction [50] parallel or perpendicular to the doping sheets.

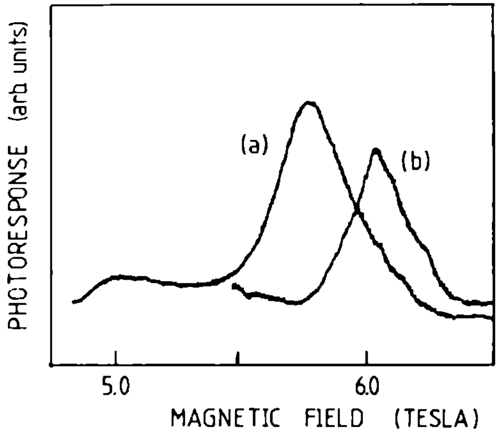

Fig 3.11 *Detail of the CW FIR ($\lambda \simeq 70.7\ \mu m$) photoconductive response at 4.2 K for MQW sample #4 from 5 to 6.5 T, for different orientations in respect to the magnetic field clearly showing dependence, as discussed in the text. a): $\theta=0^{\circ}$ and b): $\theta=19^{\circ}$.*

Good ohmic contacts could be formed to the samples using either indium dots or Au-Ge-Ni eutectic alloyed to the top surface. For the MQWs selective etching and contacting processes were performed along the edges of some of the samples studied. The most efficient way, however, to reduce the sample resistance of the MQW samples to convenient values for the detection circuitry, was through the use of interdigitated contact patterns, as have been shown in Fig 3.8 in the previous section. The ohmic contacts diffuse through the MQW stack, so that the current lines run along the well-planes.

3.6 Results

3.6.1 Zero magnetic field data

Figure 3.12 shows the typical photoresponse profiles of the homogeneously doped bulk (HDB) samples #1, #2 and #3 at zero magnetic field with 90.9 μm laser radiation and with a sample temperature of 4.2 K. In each case, the photoresponse is obtained at a convenient bias voltage (approximately 0.5 Vcm^{-1}) and at moderate laser pulse powers (approximately 5 W at the sample). The photoresponses shown in Fig. 3.12 are always normalised to the maximal signal. The decay profiles are all fitted with equation (3.8), and yield characteristic decay times, τ, of 150 ns, 23 ns, 8 ns for samples #1, #2 and #3 respectively. The laser stimulus pulse, as measured by a Schottky detector, is also indicated in the figure. The temporal displacement of the stimulus and response maxima will be discussed in section 7.

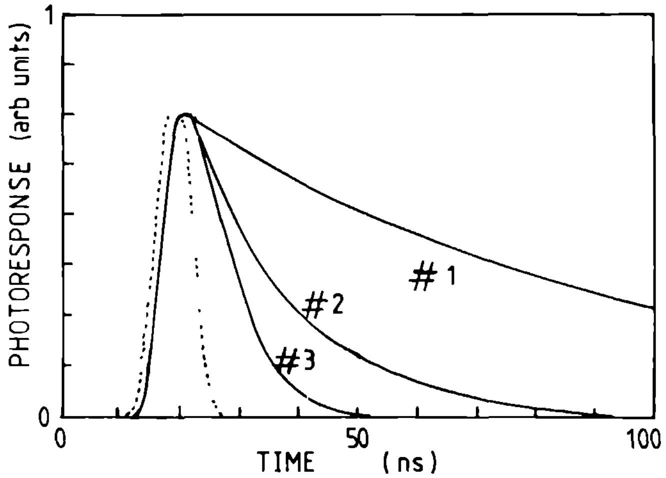

Fig 3.12 *The time-resolved photoconductive response of the HDB samples as discussed and numbered in the text, clearly showing the effect of the* N_A *dependence of the recombination time. The dotted line shows the response of the Schottky diode to the FIR stimulus. The slight temporal displacement of the maxima will be discussed in section 3.7.*

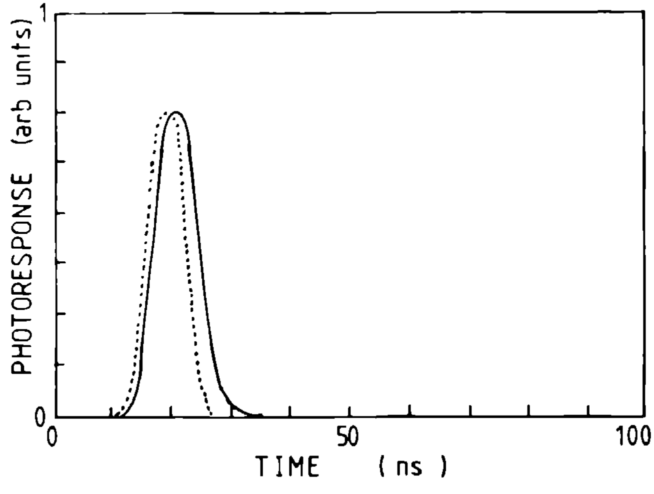

Fig 3.13 *Time-resolved photoconductive response of the MQW samples. The dotted line shows the response of the Schottky diode to the FIR stimulus. The slight temporal displacement of the maxima will be discussed in section 3.7.*

The pulsed FIR photoconductive response of the MQW samples #4, #5 and #6 have been investigated at 4.2 K in zero magnetic field under similar bias and illumination conditions. In general the characteristic decay time of the photoresponse was never longer than for the HDB samples.

In fact it is evident that the photoconductive response of the MQW layer at 90.9 μm is extremely fast. An upper limit of 1-2 ns may be placed on the photosignal rise and decay times from comparison of the measured Schottky and MQW responses as shown in Fig 3.13. These limits are set by the RC times of the detection circuitry. From these results it is suggested that the electron recombination time to the MQW shallow donor is less than 1ns. Fig 3.13 also shows the stimulus pulse (as observed on a Schottky diode); a slight temporal displacement is again noted between stimulus and response, which will be discussed subsequently.

A simple cw responsivity test of the MQWs was made for one wavelength only (118 μm), by comparing MQW signal sizes with a calibrated Ge:Ga detector. Using both detectors in the photoconductive mode, the MQW response at 70 Hz chopping frequency implied a responsivity of 10^5 VW^{-1}, which is comparable with an extrinsic epitaxial n-GaAs detector of longer response time.

A sheet doped bulk (SDB) n-GaAs layer (sample #7) was grown in order to replicate sample #5 but without the AlGaAs barrier layers. The zero-field decay time for this layer was rather slower (4 ns) than for the comparable quantum well for which a decay time of less than 2 ns was obtained.

In some cases it was possible to study the photoconductive decay of samples with various contact types or configurations (eg. Indium dots, Au-Ge interdigitated patterns, simple Hall bars, selectively-etched side contact samples etc. see section 5). In all cases similar response shapes were noted, so it may be deduced that artifacts arising from contact effects may be neglected.

A short overview of the decay times of the samples is given in Table II. Also the influence of the magnetic field is indicated qualitatively which will be discussed in the next section.

Table II: *Overview of the decay times as measured for all samples.*

Sample		experimental decay time (ns)	
type	#	B=0	B≠0
HDB	1	150	decrease
HDB	2	23	"
HDB	3	8	"
MQW	4	<2	no effect
MQW	5	<2	"
MQW	6	<2	"
SDB	7	4	increase

3.6.2 Magnetic field data

The time-resolved photoconductive response of the HDB, MQW and the SDB samples has been investigated at resonant 1s-2p$^+$ magnetic fields using a range of pulsed laser wavelengths. In each case, the decay time τ of the photoconductive response was extracted by fitting equation (8) to the experimental data. Fig 3.14 shows a compendium of data for the three HDB layers, and for the SDB layer for magnetic fields up to 9 T. In several cases, the behaviour of samples provided with different contact types or using different contact geometries was investigated, and identical results obtained. Fig 3.14 therefore represents results from 21 samples. In the case of the MQW layers, which displayed an extremely fast photoresponse (< 2 ns) at zero field, no significant magnetic field dependence was noted. This data is omitted from Fig 3.14 for clarity.

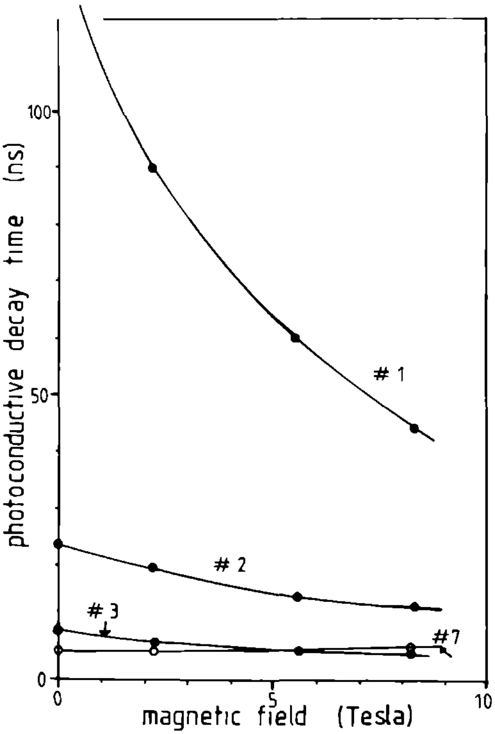

Fig 3.14 *The photoconductive decay time as a function of magnetic field for the three HDB samples as numbered in the text, and the SDB sample #7 at 4.2 K under resonant* $1s \rightarrow 2p^+$ *FIR excitation conditions.*

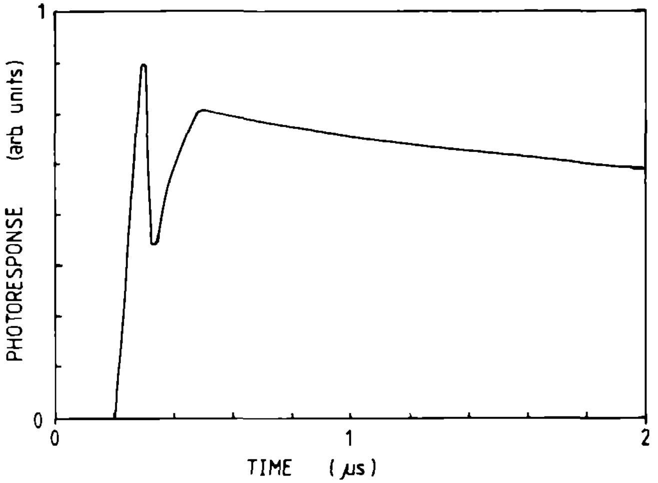

Fig 3.15 *Characteristic tail structure in the photoconductive response as a function of time at 4.2K for the SDB sample #7 at B=5.6 T and a bias of 5 V/cm.*

For the HDB samples Fig 3.14 clearly shows that the magnetic field dependence of the characteristic decay times (τ) decreases strongly with increasing magnetic field. In the case of the SDB sample, however, τ increases with increasing magnetic field from $\tau = 4$ ns at zero magnetic field up to $\tau = 8$ ns at about 9 T. An anisotropy was noted in the photoresponse when the sample was tilted with respect to the magnetic field direction. With an incident laser wavelength of 90,9 μm (resonant 1s-2p$^+$ field of 5.6 T) and magnetic field normal to the doping planes the decay time was slightly increased (1 ns) with respect to the decay time observed when the field was parallel to the planes.

All the foregoing data were taken with moderate bias. However, in Fig. 3.15, the photoresponse of sample #7 (SDB) is shown at resonant field for $\lambda = 90.9$ μm (5.6 T), under high bias conditions (5 V/cm). The photoresponse shows a tail extending to 10 μs after the laser pulse has ceased. Similar tails indicating bottle-neck effects are noted in InP by Chamberlain et al. [9]. It is noted that for the HDB samples, under high bias conditions, these tail structures were also observed, but were never as pronounced as in the case of the SDB sample.

3.6.3 Intensity dependence effects

The time-resolved FIR photoresponse has been investigated as a function of incident laser intensity. Although the characteristic decay times, as deduced from fits to equation (3.8) of the exponential part of the decay, are not directly affected by the laser intensity, it is noted that for intensities higher than a typical critical value, I_c, the very pronounced PC signal due to resonant excitation ($1s \rightarrow 2p^+$) is heavily affected by a very strong background signal as is clearly shown in Fig. 3.16. Furthermore it is noted that for all samples studied the magnitude of the photoresponse as a function of laser power displays a typical approach-to-saturation behaviour when the laser intensity exceeds a critical value, I_c; this may be seen in the inset of Fig. 3.16. I_c typically is measured to be about 10 Wcm^{-2}.

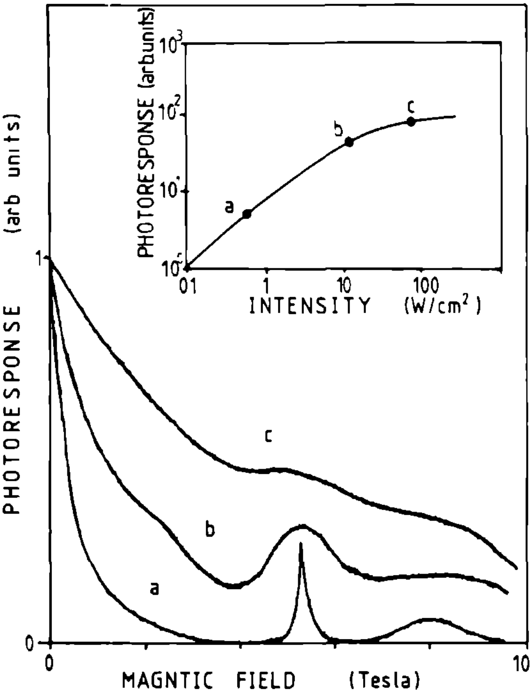

Fig 3.16 *The time integrated pulsed FIR ($\lambda \simeq 90.9$ µm) photoconductive response (PC) at 4.2K for HDB sample #3 as a function of the magnetic field (normalised at zero magnetic field) for different FIR intensities, increasing from a to c. In the inset, the saturation behaviour of the PC is shown for the resonant $1s \rightarrow 2p^+$ transition at 5,6T.*

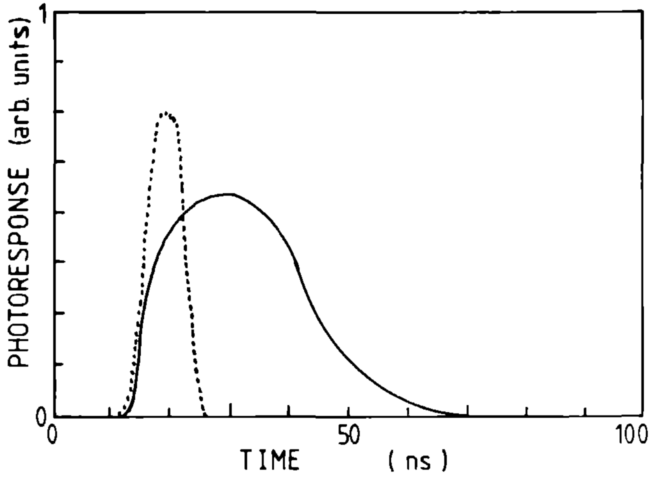

Fig 3.17 *Time-resolved photoconductive response of sample #3 under saturation conditions, clearly showing an anomalous prolongation of the signal after the stimulus has ceased. The dotted line shows the response of the Schottky-diode to the FIR stimulus.*

It is also noted that clear changes occur in the shape of the photoconductive response, just after the signal maximum, when the laser intensity is sufficiently high that the saturation conditions are approached. As may be seen in Fig. 3.17 the shape of the response, just after the signal maximum, clearly does not show an exponential-like decay. In such a case, the second derivative of the response function would be positive in this region. The same shape of response was found in the simulations for electronic saturation, see Fig. 3.7. It is noted that for all the classes of sample investigated the onset of saturation behaviour occurs at a lowest absolute laser intensity, I_c, under the specific magnetic field and laser energy conditions for which the $2p^+$ shallow impurity energy level is coincident with the N=0 Landau level. This behaviour will be discussed in section 3.7.1.

3.6.4 Temperature dependence effects

Finally, the time-resolved FIR photoresponse has been investigated as a function of temperature. A clear effect is noted: The characteristic decay times, τ, are found to increase with increasing temperature. Fig. 3.18 shows the temperature dependence of τ for the specific case of the HDB sample #3. A supra linear (approximately T^2) behaviour is observed up to T = 10 K, and a linear dependence is noted above this temperature, which will be further commented on in section 3.7.1.

At temperatures higher than about 30K no clear photoresponse could be obtained because of the extreme noise in the signals. At these temperatures the expected signal is weak due to thermal ionisation of the donors which affects the free carrier concentration drastically.

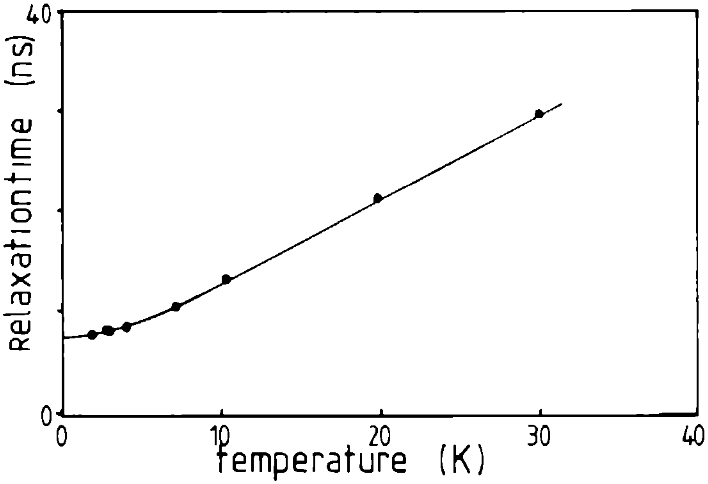

Fig 3.18 *Temperature dependence of the photoconductive decay time for HDB sample #3. The line which has a square law behaviour up to 10K is to guide the eye.*

3.7 Discussion

Previous time-resolved FIR photoconductivity measurements have been reported for InP using rather longer stimuli (typically 50 ns), for which only the pulse cut-off (and not the whole pulse) was well-defined. The present experiments are the first to be reported using a short pulse for which the entire profile is well-defined. The only other previous report of a time-resolved FIR measurement for GaAs is mentioned by J. Kaminski et al. [35]: for a bulk sample with electrical properties intermediate between the present samples #2 and #3, those authors determined a characteristic decay time of 15 ± 5 ns. This result is completely consistent with the present experimental data shown in Table III; a further discussion of this Table will be presented later in this section.

The application of the short pulse stimulus in the present experiments produces a characteristic photoconductive response, as shown in Fig. 3.12 of the previous section. The rise in the sample photoresponse closely follows the laser pulse, as measured by a Schottky detector, but a small temporal 'delay' between the maxima of stimulus and response is always noted; this feature may be explained considering the fact that the maximum of the photoconductive response will in general occur when the electron excitation and recombination rates are equal; because of the nearly square wave laser pulses available in the present study this situation of detailed balancing is achieved approximately at the termination of the stimulus pulse. The slight delay (typically 1-2 ns) noted in the present work is ascribed to the small departure from an ideal square wave stimulus. Chamberlain et al. [9] have also noted a time lag in the photo response of InP under saturation conditions using much longer pulses which did have typical fall times of about 100 to 200 ns, and described this feature to phonon diffusion effects. Because of the saturation condition, the detailed balance point probably is reached during the long decay of the laser stimulus. It is therefore possible to account for the delays noted in their experiment, using simple rate equation arguments, without recourse to a phonon diffusion process.

The decay of the photosignal will now be considered. Fits to the experimental data (D(t)), as typically shown in Fig. 3.12 of the previous section, in principle are made using equation (3.8).

$$D(t)=\frac{A}{(1+B)\exp(t/\tau)-1} \tag{3.15}$$

where A (the amplitude), B (the ratio N_A/n_0) and τ (the relaxation time) were fitted by a least square method considering about 100 data points. The decay-time fitting routine used by the computer is arranged to commence at a time position for which the second derivative of the signal is zero. This procedure is consistently used for all the decay profiles which have been measured. The results for zero magnetic field are shown in Table III. In general, the experimental conditions such as temperature, bias voltage, magnetic field, laser intensity are arranged so that the decay profiles are closely exponential. However, under extreme saturation conditions (see Fig 3.17) an anomalous response is developed which will be discussed subsequently. Nevertheless, the choice of this temporal starting point in the present fitting procedure delivers consistent results.

As discussed in section 3.4.2, the simple expression for the decay time, τ, may be obtained from the equation

$$\tau = \frac{1}{C' N_A} \tag{3.16}$$

Table III lists the values of τ calculated from the above equation at 4.2K for zero magnetic fields and moderate bias voltages and laser intensities and these are compared with the τ values obtained experimentally. In the absence of any values in the literature for the recombination coefficient, C′, for either bulk GaAs or MQW samples, the value, $2 \cdot 10^{-7}\mathrm{cm}^3\mathrm{s}^{-1}$, for bulk InP [5], is scaled, in first approximation (equation (3.13) not taken into account), to $4.5 \cdot 10^{-7}\mathrm{cm}^3\mathrm{s}^{-1}$ and to $1.4 \cdot 10^{-7}\mathrm{cm}^3\mathrm{s}^{-1}$ to account for the difference in the Bohr orbit area in the bulk GaAs and the MQW samples (with Bohr radius 100Å and 55Å respectively). As discussed previously, C′ is related to the effective cross section for capture.

It is important to note that the fit parameter B (defined as N_A/n_0) is expected to be much larger than unity in the case of highly compensated samples and/or low excitation intensities. Indeed, high B-values were found by the fitting routine for the rather highly compensated HDB sample #3 but not for the high purity HDB samples #1 and #2.

As noted in Table III, for the highly compensated HDB sample #3 the agreement between the calculated and measured values of τ is surprisingly good; similar agreements have also been noted in highly compensated InP specimens [5]. For the samples #1 and #2, however, a strong discrepancy was found between these values; one possible reason for this discrepancy may be the fact that both these samples show an additional effect in their CW FIR PC spectra which is known to be the D^--states. These are states of an electron bound to a neutral donor [47]. These D^--states are very weakly bound and have a rather large extension; therefore, they can only exist in very pure samples with a long scattering length. For the samples #1 and #2 these states can possibly enhance the capture of free electrons and as a consequence reduce the measured decay time.

Table III *Experimentally determined values (τ_{exp}) of the decay time of the photoconductive response at 90.9 μm in zero magnetic field for the samples studied. (N_D-N_A) and N_A values are obtained as discussed in the text. τ_{calc} is the calculated decay time from equation (8); a scaled value of $C = 4.5\cdot10^{-7}$ $cm^{-3}s^{-1}$ is taken for the bulk. *) has been geometrically weighted: see text.*

Sample type	#	τ_{exp} B=0 (ns)	N_D-N_A (cm^{-3})	N_A (cm^{-3})	τ_{calc} (ns)
HDB	1	150	$2.8\cdot10^{13}$	$0.7\cdot10^{13}$	317
HDB	2	23	$5.0\cdot10^{13}$	$2.0\cdot10^{13}$	111
HDB	3	8	$3.0\cdot10^{14}$	$3.0\cdot10^{14}$	7
MQW	4	<2	$8\cdot10^{15}$	$2\cdot10^{15}$	4
MQW	5	<2	$8\cdot10^{15}$	$2\cdot10^{15}$	4
MQW	6	<2	$8\cdot10^{15}$	$2\cdot10^{15}$	4
SDB	7	4	$8\cdot10^{15}$	$2\cdot10^{15}$	4*)

The impurity concentration data quoted in Table III for the other bulk doped sample (the SDB sample #7) relates to the doping sheet only. Recombination in this sample will, of course, also occur in the undoped regions ($N_A \simeq 7\cdot10^{13}cm^{-3}$). A simple application of equation (3.15) would yield τ_{calc} of 1 ns; however, application of this equation using a geometrical weighting for N_A in the sheet doped and undoped regions results in $\tau = 4$ ns in close agreement with the experimental values. The implication of this statement is that for B=0, the electrons can not distinguish the individual doping sheets but only detect a macroscopic average.

Table III also shows τ values for the MQW samples calculated from equation (3.15). Although the experimental and calculated τ values show order-of-magnitude consistency, there are several reasons why the use of equation (3.15) may be inappropriate for these confined geometry samples. Recombination in the MQW case is likely to be only to ionised donors in a particular quantum well, since tunnelling through (or transport over) the barriers is unlikely. This contrasts with the case of the bulk materials, for which recombination is possible in principle throughout the entire sample volume. Furthermore, the simple scaling of the recombination coefficient, C′, neglects any energy dependence of this quantity: in the MQW the larger effective Rydberg (10 meV) in comparison with the bulk case (5.7 meV) implies that the photoinjected electrons must be captured with different energies in the bulk and MQW cases. It should be noted also, that because of the strong coupling of the energies with the location of the donor in the well, much more different binding energies are involved. This can be seen, for example, by observing the linewidth of the transitions in a magnetic field, which clearly are wider than their bulk counterparts [29]; it is not clearly determined to what extent this linewidth influences the lifetime. The most significant omission, however, is that the recombination parameter, C′, although scaled, is essentially a three dimensional quantity. The direct use of this parameter does not reflect the confined two-dimensional nature of the electron motion in the MQW. In view of these important differences, the disagreements in τ_{exp} and τ_{calc} values shown for the MQW samples in Table III are not surprising; further discussion of the above-mentioned confinement effects will be considered now.

From a previous study [10] of shallow donor recombination dynamics in bulk material, there are good reasons to suggest that any effect which reduces the characteristic Bohr radius for the electrons will result in an increase of the acoustic phonon-assisted recombination rate. As discussed in section 3.4.3, the application of the Fermi Golden rule leads to a rate expression of the form:

$$\Gamma = Aq^2 \exp(-2a^2q^2) \tag{3.17}$$

where the parameter A contains both material constants and a weighted average over all of the individual recombination transitions involved.

It is argued from the magnetic field recombination studies of Rikken et al. [10] in InP, and also later in this section for the present GaAs-based samples, that the reduction in the Bohr radius which occurs in field as a result of the magnetic squeezing of wavefunctions will give rise to an increase in the electron recombination rate. Analogously, it may be argued that the reduction in Bohr radius which takes place for the present 150 Å MQWs will also give rise to an increased recombination rate. In consequence, the recombination parameter C′, considered above, will differ in the bulk and MQW samples.

It is possible to estimate the confinement effect on the parameter C′. The recombination rate (13) has a maximum when $2(a^2q^2)=1$, following from differentiation with respect to q. The implication of this statement is that, for a given a, a certain wavevector, q, exists for which the electron-phonon coupling is most efficient; the $\exp(a^2q^2)$ term in the recombination rate can be estimated to be constant and therefore the recombination rate (equation (3,17)) is governed by the prefactor, Aq^2. The change in the effective Bohr radius from 100 Å in the bulk case, where the most efficient phonon for recombination is the one with energy approximately 1 meV (from section 3.4.3), to 55 Å for the MQWs investigated now results in a most efficient phonon wavevector which is diminished by a factor of (55/100); this leads to an approximate decrease of $(55/100)^2$ ($\simeq$ 25%) in τ. Taking the value of τ for the sheet doped bulk sample of 4ns therefore results in a recombination time of 1ns for the MQW, which is consistent with the observed values within the experimental accuracy.

The Fig. 3.14 displays the magnetic field dependences of the recombination time, τ, for the bulk (HDB and SDB) data. For the HDB samples, the magnetic field results in every case in a reduction of τ : Typically, this reduction factor is between 2-3 times from zero to 10 Tesla. Applying similar arguments to the above, the squeezed Bohr radius at 10T (approximately 67 Å [43]) results in a τ diminished by a factor of approximately $(67/100)^2$, i.e. a reduction of 2.2, which is again consistent with the experimental observations. The variation in the actual reduction factor between the samples is a consequence of different weighted averages in the expression (3.13) for the different samples, which reflect the different capture efficiencies of the various excited bound states; for samples with a low doping concentration the inter-impurity distance is big and consequently more bound states are available. The confinement of the wavefunction due to the magnetic field will influence the different orbit sizes differently which may explain the difference for magnetic field dependence as obtained in the experiment.

A noteworthy feature of Fig. 3.14 is the reduction in the slope of the decrease in τ at increasing field; at very high magnetic fields (exceeding those available in the present measurement) it could be envisaged that the curves become parallel to the field axis. The explanation of this behaviour is that as the field is increased, pinning of the impurity energy levels to the Landau levels occurs [4]. Thus the relative weighted averages of the individual electron transitions to the excited bound states do not change with increasing field, as the energy separations between the Landau levels and the excited bound states remain approximately constant. An experimental test of this observation at magnetic fields of 30-40 T would thus be of considerable interest.

In contrast with the observation of Rikken et al. [10] for InP and the saturation-absorption studies of Allan et al. [8] in bulk GaAs, the experimental τ values, at the highest fields presently available, are still found to be dependent on N_A, as is expected in the rate equation model (as explained in section 3.4.2).

The τ value of the SDB sample #7, in contrast to the HDB samples discussed above, is observed to exhibit a factor of two increase as the magnetic field rises to 10T. A possible explanation of this effect is that the increase in τ represents a change in the relative contributions of the heavily doped (10^{16} cm^{-3}) sheet and the nominally undoped (10^{14} cm^{-3}) regions to the measured temporal dependence of the sample photoresponse. At zero magnetic field, the major proportion of the total sample photocurrent runs along the heavily doped sheet regions; the minor proportion runs along the higher resistance undoped regions between the doping-sheets. The resistance of the heavily-doped regions will be low in comparison with the nominally undoped regions, as the Mott broadening conditions are almost fulfilled. With increasing field, however, magnetic 'freeze-out' occurs initially for the heavily doped regions: the resistance of these regions rises, and the relative proportions of photocurrent carried by the two types of regions in the sample changes. The net result is that the contribution of the (longer decay) undoped regions is enhanced, and the measured photoresponse decay time is longer than at zero magnetic field.

3.7.1 Other effects

A saturation behaviour is noted in the inset of Fig. 3.16. This may arise, as in the case for a saturation-absorption experiment, from the exhaustion of donors in the ground-state. In a photoconductivity experiment, however, it is also important to bear in mind that under saturation conditions the heating of the free carriers (which have already been excited into the conduction band by the laser pulse) may result in an enhanced mobility due to free carrier absorption [15,16]. A simultaneous transmission and photoconductivity experiment on the same sample might therefore result in different saturation intensities. It can also be noted from Fig. 3.16 that at high intensities a smooth PC background signal can be obtained which is due to free carrier absorption; resonant transitions are broadened and finally completely smeared out as the laser intensity is increased. Fig. 3.17 shows clear evidence of the effects of carrier heating on the time-resolved scale when the saturation conditions are achieved. A pronounced 'delay' effect is noted close to the maximum photoresponse, which arises from increased mobility effects in the sample. As mentioned previously, care was taken to use in the analysis only those pulse decay shapes which did not show this anomalous behaviour. Nevertheless, the computer fitting routine is in principle capable of handling pulses obtained under saturation conditions. Finally, it is noted that anomalous pulse shapes, as seen in Fig. 3.17, could also be produced artificially if the load resistor used in the measurement circuit was not chosen correctly. Details of this problem have been considered in section 3.5.2.

It is noted that saturation behaviour is obtained at lower absolute laser intensity when the $2p^+$ shallow impurity level is coincident with the N=0 Landau level. Similar results have been reported by Kaminski and Spector [36] in a saturation-photoconduction study using a free electron laser. A possible explanation for this observed effect could be found in the increased ionisation efficiency from the $2p^+$ level into the N=0 Landau level. It should be noted that an electron in an excited $2p^+$ state always has different possibilities (and therefore different transition probabilities) for relaxing back to the ground state (see Fig. 3.4) by staying bound to the donor or by becoming ionised, and thus taking part in the conduction process. Due to a possible small interaction between the $2p^+$ and N=0 wavefunctions mixing can occur as their levels cross. This effect, known as hybridisation, is not unusual for orthogonal states [51]. Due to this hybridisation both $2p^+$ and N=0 states mix and a pronounced enhancement of the transition probability can be realised. Therefore, it is reasonable to assume that ionisation will be more efficient and that at lower stimulating intensities an increased population of electrons in the conduction band may be expected.

Although under normal experimental conditions no effects on the pulse response shape were obtained as a function of electrical bias, it should be noted that under saturation conditions the anomalous response shape (discussed above) could be further enhanced with increasing bias electric field. At extreme bias voltages ($\simeq$5 Vcm^{-1}), impact ionisation effects were noted which resulted in additional long-term structure extending to several microseconds after the termination of the laser pulse (see Fig. 3.15). These "tail"-structures can be explained by the reionisation (by impact ionisation) of electrons in a low lying bound state, which acts as a "bottleneck" in the (cascade) decay process of the electron into the ground state. This lowest lying excited bound state is known to be the $2p^-$ state in magnetic field or the 2s state for zero magnetic field which is then degenerate with the 2p level. Chamberlain et al. [9] have observed similar effects in InP; using an appropriate four-level model these authors simulated the observed photoresponse, and concluded that the maximum of the "tail" photoresponse occurred at a time approximately equal to 50 % of the $2p^- \rightarrow 1s$ lifetime after the maximum in the direct response. Applying the arguments of these workers to the data of Fig. 3.15, it is concluded that the $2p^- \rightarrow 1s$ lifetime for GaAs is 500ns. This value is in excellent agreement with the conclusions of the saturation-absorption studies of Allan et al. [8]. Chamberlain et al. [9] were unable to observe any tail structure in GaAs samples similar to #3 because of the limits of their instrumentation.

The temperature dependence of the recombination time, shown in Fig. 3.18, may be explained considering the simple expression for the relaxation time equation (3.16) where τ is inversely proportional to the number of recombination centers and to the recombination parameter. The lower temperature portion of Fig. 3.18 exhibits an approximately T^2 dependence. For low temperatures, however, the number of recombination centers is approximately constant and equal to N_A. The temperature dependence, therefore, is governed by the change in the recombination parameter, C'. Brown and Rodriguez [34] theoretically estimated a similar square law behaviour for Germanium by calculating the capture cross section using the principle of detailed balance between capture and thermal reionisation. Their approximation is in good agreement with the results obtained for shallow donors in Germanium [54] as well as in InP by Rikken et al. [5] who found a $T^{1.7}$ dependence. In the higher temperature part of Fig. 3.18 the temperature dependence flattens from a square law behaviour to a linear-like behaviour, as noted in the present measurements above 10K. A reason for this flattening could be the onset of thermal exhaustion of the donors which results in an increase of ionised donor centers and as a consequence application of equation (3.16) will induce a decrease in the recombination time. At even higher temperatures and higher thermal donor ionisation rates the possibility of free carrier absorption increases. This can induce an additional change in the electron mobility which can be estimated from the shape of the photo response. This complicates the interpretation of the trend of the temperature dependence at high temperatures.

3.8 Conclusion

An important aim of the present study was to determine if reduction of dimensionality, as in the MQWs, would result *per se* in an increase of recombination rates. This possibility had been suggested by analogy with the magnetic field case, where the capture cross section is influenced because of the squeezing of the electron wavefunctions which induces a change in the efficiency of the electron-phonon interaction mechanism. It is known that in QWs the quasi two-dimensional geometry has an analogous effect on the electron-donor system and that consequently the wave functions of the in-well donors are already squeezed.

Therefore a time-resolved photoconductivity study was performed to measure recombination times of AlGaAs/GaAs MQW-structures with a Silicon doping in the center of the well versus n-GaAs HDB material with an isotropic doping characteristic. Also a SDB sample was used with a non-homogeneous Silicon doping profile, in order to mimic the QW structures but omitting the AlGaAs barriers.

Within the limits of the experimental observations, it is noted that the recombination time in the SDB sample (4-8 ns) is indeed clearly longer than in the MQWs ($\simeq$1 ns), but is also shorter than in all HDB (8-150 ns) samples considered. The implication of this, therefore, is that confinement of electrons in the MQW does lead to an enhancement of the shallow donor recombination rate. This behaviour could form the basis for a new type of fast, sensitive submillimeter detector. It is noted that at a 70 Hz chopping frequency the MQW photoconductive responsivity is about 10^5 VW^{-1}, which is comparable with an extrinsic epitaxial n-GaAs detector of longer response time.

It is indicated that there are several problems associated with the design of a "clean" experiment which can definitively conclude if these confinement effects are, or are not, present. A fundamental problem could be the fact that the energies of the impurity states involved in a MQW are clearly different from their bulk counterparts and the fact that the recombination in a MQW is restricted to a single well whether in the bulk case recombination could occur throughout the entire sample. One of the experimental problems is the practical difficulty of growing bulk and MQW samples with exactly the same density of recombination sites (ie N_A), which is shown to be a very important parameter in the determination of the recombination time.

The magnetic field data, however, presented in this Chapter present unambiguous evidence of the increase in shallow donor recombination rates in magnetic fields up to 10T. This evidence is obtained for the first time in GaAs using a photoconductivity technique. The mechanism for this rate increase involves the change in cross section as the magnetic field squeezes the electron wavefunction.

The temporal photoresponse data presented have all been analysed using only phonon recombination and impact ionisation processes. No effects of electric field or illumination intensity could be discerned in the present measurements which produce changes in the temporal decay profiles of the type which Rikken et al [32] regarded as evidence for Auger recombination in InP samples under certain conditions. Radiative recombination events should occur in the GaAs samples investigated, though very weak [52]; however no attempts were made in this study to investigate them. The analysis was performed without recourse to the influence on the mobility of the sample due to the application of very short excitation pulses, as has been discussed in section 3.2. For longer pulse excitation, however, future time-resolved Hall measurements could provide further information about the mobility behaviour which probably increases in the saturation regime.

Due to an enhanced "tail"-structure, caused by impact re-ionisation under high bias conditions, it has been shown for the first time in time-resolved data that the relaxation time τ for the $2p^-$ level is 500 ns which is consistent with the value deduced from saturation experiments.

References

[1] e.g. R.T. Grimes, M.B. Stanaway, J.M. Chamberlain, M. Henini, and O.H. Hughes, Semicond. Sci. Technol. 4, 548 (1989)

[2] K.M. Lau, and W.L. Wilson, Jr. Infrared Phys. 23, 311 (1983)

[3] R.L. Greene, and K.K. Bajaj, Phys. Rev. B 34, 951 (1986)

[4] J.M. Mercy, Y.H. Chang, A.A. Reeder, G. Brozak, and B.D. McCombe, Superlattices and Microstructures 4, 213 (1988)

[5] G.L.J.A. Rikken, P. Wyder, J.M. Chamberlain, R.T. Grimes, and L.L. Taylor, Phys. Rev. B 34, 4156 (1988)

[6] G. Ascarelli, Z. Rodriguez, Phys. Rev 124, 1321 (1961)

[7] M. Lax, Phys. Rev 119, 1502 (1960)

[8] G.R. Allen, A. Black, C.R. Pidgeon, E. Gornik, W. Seidenbusch, and P. Colter, Phys. Rev. B 31, 3560 (1985)

[9] J.M. Chamberlain, A.A. Reeder, L.M. Claessen, G.L.J.A. Rikken, and P. Wyder, Phys. Rev. B 35, 2391 (1987)

[10] G.L.J.A. Rikken, P. Wyder, J.M. Chamberlain, G.A. Toombs, and L.L. Taylor, Phys. Rev. B 38, 2002 (1988)

[11] R.E.M. de Bekker, L.M. Claessen, and P. Wyder, J. Appl. Phys 68, 3729 (1990)

[12] G.E. Stillman, C.M. Wolfe, and J.O. Dimmock, in "*Semiconductors and Semi-metals*" Vol 12, "*Infrared detectors II*", chapter 4, eds. R.K. Willardson and A.C. Beer, Academic, New York (1977)

[13] H.J.A. Bluyssen, J.C. Maan, L.J. van Ruyven, F. Williams, and P. Wyder, Solid State Commun. 25, 895 (1978)

[14] H. Brooks, in "*Advances in Electronics and Electron Physics*", Vol 7, ed. L. Morton, Academic, New York (1955); and K. Seeger, "*Semiconductor Physics, an Introduction*", chapter 6, Springer, Berlin (1982)

[15] J. Burghoorn, A. van Klarenbosch, T.O. Klaassen, W.Th. Wenckebach, and C.T. Foxon, in Materials Science Forum 65-66, p. 363 (1990) [Trans-Tech Publications, Zürich]

[16] A. van Klarenbosch, thesis, University of Leiden 1990, unpublished

[17] H.A Bethe and E.E. Salpeter, "*Quantum Mechanics of One- and Two Electron Atoms*", Springer, Berlin (1957)

[18] A. Messiah in "*Quantum Mechanics*", North Holland Publishing Company, Amsterdam (1981)

[19] N.F. Mott, Can. J. Phys. 34, 1356 (1965)

[20] D.M. Larsen, J. Phys. Chem. Solids 29, 271 (9168)

[21] W. Rösner, G. Wunner, H. Herold, and H. Ruder, J. Phys. B 17, 29 (1984)

[22] H.P. Wagner, and W. Prettl, Solid State Commun. 66, 367 (1988)

[23] W.S. Boyle, and R.E. Howard, J. Phys. Chem. Solids 19, 181 (1961)

[24] J. Simola, and J. Virtamo, J. Phys. B 11, 3309 (1978)

[25] G. Bastard, Phys. Rev. B 24, 4714 (1981)
[26] M. Stopa, and S. DasSarma, Phys. Rev B 40, 8466 (1989)
[27] M. Shinada, and K. Tanaka, J. Phys. Soc. Jpn. 29, 1258 (1970)
[28] N.C. Jarosik, B.D. McCombe, B.V. Shanabrook, J. Ralston, and G. Wicks, Phys. Rev. Lett. 54, 1283 (1985)
[29] R.T. Grimes, M.B. Stanaway, J.M. Chamberlain, J.L. Dunn, M. Henini, O.H. Hughes and G. Hill, Semicond. Sci. Technol. 5, 305 (1990)
[30] S. Huant, M. Grynberg, G. Martinez, B. Etiennne, B. Lambert, and A. Regreny, Solid State Comm. 65, 1467 (1988)
[31] J.J. Dunn, E. Pearl, R.T. Grimes, M.B. Stanaway, and J.M. Chamberlain, in Materials Science Forum 65-66 p. 117 (1990) [Trans Tech Publications, Zürich]
[32] G.L.J.A. Rikken, P. Wyder, J.M. Chamberlain, D.P. Halliday, and R.T. Grimes, Solid State Electr. 31, 763 (1988)
[33] S.H. Koenig, and R.D. Brown, Phys. Rev. Lett. 4, 170 (1960)
[34] R.A. Brown, S. Rodriguez, Phys. Rev. 513, 890 (1967)
[35] J. Kaminski, J. Spector, W. Prettl, and M Weispfenning, Appl. Phys. Lett. 52, 233 (1988)
[36] T. Ohyama, E. Otsuka, S. Yamada, T. Fukui, and N. Kobayashi, Jpn. J. Appl. Phys. 22, 742 (1983)
[37] F. Brown, A. Anderson, and P.A. Wolf, Int. J. Infrared & Millimeter Waves 1, 277 (1980)
[38] K. Muro, N. Yutani, and S. Narita, J. Phys. Soc. Jpn. 49, Suppl A, 593 (1980)
[39] W. Müller, E. Gornik, T.J. Bridges, and T.Z. Chang, Solid State Electr. 21, 1455 (1978)
[40] P.R. Bratt in "*Semiconductors and Semi-metals*", Vol. 12,"*Infrared detectors II*", chapter 2, eds. R.K. Willardson and A.C. Beer, Academic, New York (1977)
[41] G.L.J.A. Rikken, thesis, Nijmegen 1987, unpublished
[42] T.K. Pramanik, D.B. Bhattacharya, Solid State Commun. 59, 737 (9186)
[43] Y. Yafet, R.W. Keyes, and E.N. Adams, J. Phys. Chem. Solids, 1, 137 (1956)
[44] B.Lengeler, Cryogenics 14, 439 (1974); R.K. Kirschman, Cryogenics 25, 115 (1985) Texas Instruments, Thomson
[45] A.T. Lee, Rev. Sci. Instrum. 60, 3315 (1989)
[46] R.L. Williams, J. Appl. Phys. 40, 184 (1969)
[47] S.P. Najda, C.J. Armistead, C. Trager, and R.A. Stradling, Semicond. Sci. Technol. 4, 439 (1989)
[48] A. Chandra, C.E.C. Wood, D.W. Woodward, and L.F. Eastman, Solid State Electronics 22, 645 (1979)
[49] D.A. Anderson and N. Apsley, Semicond. Sci. Technol. 1, 187 (1986).

[50] H. Sigg, K. Ploog, Q.Y. Ye, and F. Koch, Phys. Rev. Lett. **64**, 1951 (1990)

[51] eg. L.M. Claessen, thesis; chapter 3, University of Nijmegen 1987, unpublished; K. Langerak, thesis ; chapter 3, University of Nijmegen 1990, unpublished.

[52] Melngailis, G.E. Stillman, J.O. Dimmock, and C.M. Wolfe, Phys. Rev. Lett. **23**, 1111 (1969)

[53] S.H. Koenig, R.D. Brown and W. Schillinger, Phys. Rev. **128**, 1668 (1962)

CHAPTER 4

SPIN LATTICE RELAXATION MEASUREMENTS UNDER ELECTRON PARAMAGNETIC RESONANCE CONDITIONS BY MEANS OF A PICK-UP COIL

ABSTRACT

A new method of measuring the spin-lattice relaxation time in solids under far-infrared electron paramagnetic resonance conditions is presented. In this method the change of the longitudinal magnetisation due to the spin relaxation, after pulsed excitation, is directly probed by means of a pick-up coil. The method is illustrated for $Cd_{1-x}Mn_xTe$ mixed crystals where the magnetisation is due to the Mn^{2+} spins. The temperature dependence of the spin-lattice relaxation time is studied for a composition of x=0.005.

(Parts of this chapter have been published in Appl. Phys. Lett. 57, 831 (1990))

4.1 Introduction

Pulsed Far Infra-Red (FIR) Electron Paramagnetic Resonance (EPR) investigations in high magnetic fields offer a variety of advantages and new physical conditions with respect to conventional EPR measurements performed with standard low field microwave EPR spectrometers.

Consider a spin system consisting of uncoupled spins having a total electron spin "S". In the absence of a magnetic field this system will be multi-fold degenerate because the S_z=-S, -S+1, ..., S-1, S states all have the same energy [1]. Application of a magnetic field lifts this degeneracy and the levels are split by the Zeeman energy $g\mu B$ as is schematically shown in Fig. 4.1 for the case of S=1/2. Between these non-degenerate levels optical transitions can be induced if the selection rule $\Delta S_z=1$ is obeyed. The excitation energy corresponding to this transition at high magnetic field does not lie in the microwave region, but in the FIR spectrum.

Due to the lifting of the degeneracy a distribution of the population of the individual spin states will be obtained depending on the temperature. In high magnetic fields and at liquid helium temperatures, the Zeeman splitting can be larger than the thermal energy kT, a condition which is usually not encountered in microwave EPR. This means that only the lowest spin levels are populated and almost all spins are aligned along the external magnetic field, allowing for a higher sensitivity than in microwave experiments [2]. This external field may also be stronger than the internal dipole and exchange fields.

Under EPR conditions the equilibrium of the spin level population is disturbed by the resonant pumping of the spin levels. If the resonant radiation is continuous a new equilibrium population distribution will be reached. However, for short enough pulsed EPR excitation an equilibrium situation will not be achieved. The spins excited by the EPR FIR pulse will drop back to the levels they populated before the pulse excitation. This relaxation now will proceed with a typical relaxation time which is called the spin-lattice relaxation (SLR) time because the main mechanism for the process is the thermal coupling of the spin system with the lattice.

For paramagnetic ions in crystals the dominant mechanism for this spin-lattice interaction is the phonon modulation of the crystalline electric field. Different possible processes in the spin-lattice interaction, involving one or two phonons, are effective. Due to their own dependences of parameters as temperature and magnetic field, these processes may be distinguished and the measurement of the SLR time will provide a characteristic quantity for the study of the spin dynamics in a spin system.

To investigate SLR times a variety of low field measurement techniques under EPR conditions using radio frequencies or microwave radiation were developed [2] as there are line shape studies, continuous wave or pulsed saturation techniques [3] and field-modulated Faraday rotation techniques [4]. These techniques in principle could be extended into the high field region. Also non-resonant techniques have been successfully applied, which measure the dynamic susceptibility [5]. It is noted that in the nonresonant experiments, all objects influencing the magnetisation, such as single spins, pairs or clusters can contribute to the relaxation time. Applying all these techniques, however, the SLR time is only deduced in a rather indirect way. A direct way would be a time-resolved study of the spin-lattice relaxation process itself.

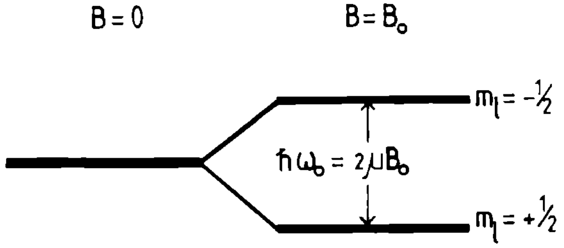

Fig. 4.1 *Energy level splitting of spin 1/2 in a static magnetic field B. In case of a field* B_0*, the photon energy,* $\hbar\omega_0$*, for resonant excitation is indicated.*

Evidently, one of the most direct means of a time-resolved measurement of the SLR time is probing the behaviour of all the spins after a perturbation by means of direct measurements of the change in the magnetisation due to the relaxation process. The perturbation is caused by FIR pulses with a photon energy equal to the Zeeman energy. Every spin that relaxes will change the magnetisation parallel to the static magnetic field and as a consequence, whilst the relaxation process progresses, the change per unit time of this magnetisation ($\Delta M/\Delta t$) will also change in time. This change can be detected as the induced voltage in a pick-up coil which is placed around the spin system [6,7]. Because the relaxation times are on the order of microseconds and the sensitivity of pick-up coils is dependent on their response time, it is necessary to apply a powerful pulsed FIR source to be able to create an instantaneous and prominent change in the population of the spins. It is noted that in addition to high power, the pulses should have fall-off times smaller than the relaxation time.

Therefore, in this chapter a magnetic spectrometer is presented based on a pick-up coil to measure the spin-lattice relaxation rates in high magnetic fields and low temperatures. Also first measurements are presented on samples of $Cd_{1-x}Mn_xTe$, which belong to a rather new class of magnetic materials, which are the dilute magnetic semiconductors (DMS) [8,9]. An advantage of these materials is that a large range of spin concentrations can be obtained (between 10^{+18} cm^{-3} to 10^{+23} cm^{-3}), which makes them very useful for fundamental studies of spin interactions.

The temperature dependence of the SLR-time for low Mn^{2+} concentration (x=0.005) at about 10 T has been measured, and shows a strong decrease as the temperature increased. This result will be discussed considering one- and two-phonon processes. For a more detailed study on $Cd_{1-x}Mn_xTe$ for different concentration x, magnetic fields and temperature, using this pick-up coil spectrometer a reference is given to the work of A.M. Witowski and T. Strutz as descibed in [10].

Another direct way of measuring the SLR time under EPR condition is the use of multi-pulse techniques to excite electron spin echoes [6,11]. This technique can also be used to measure the spin-spin relaxation time, which is another characteristic relaxation process in spin systems. This technique, however, is not yet available for high magnetic field applications, though most of the technical obstructions may be solved by now. In the APPENDIX a short explanation of the principles of spin-echo spectroscopy is presented, and the experimental possibilities for extension into high field are discussed.

4.2 Experimental

The principle of measuring the SLR times by means of a pick-up coil, placed around a magnetic sample, follows from Faraday's induction law. In such a coil a voltage is induced proportional to the time derivative of the sample magnetisation component along the coil axis. By monitoring this voltage, one can observe the relaxation of the magnetisation after a perturbation. The effect of the perturbation itself will also induce a voltage in the pick-up coil, though with opposite polarity. Because this signal due to the perturbation only depends on the magnetic response of a sample under EPR conditions, comparison with responses from simple transmission studies under similar conditions may show differences in, for example, sensitivity. Therefore, to study both the relaxation time and the proportionality of the signals of the sample response by different methods the experiment is split in two parts: one which only considers the time integration from both the transmission signal as also the response from the pick-up coil signal due to the perturbation itself and a second which in principle is the time-resolved measurement to obtain the SLR time.

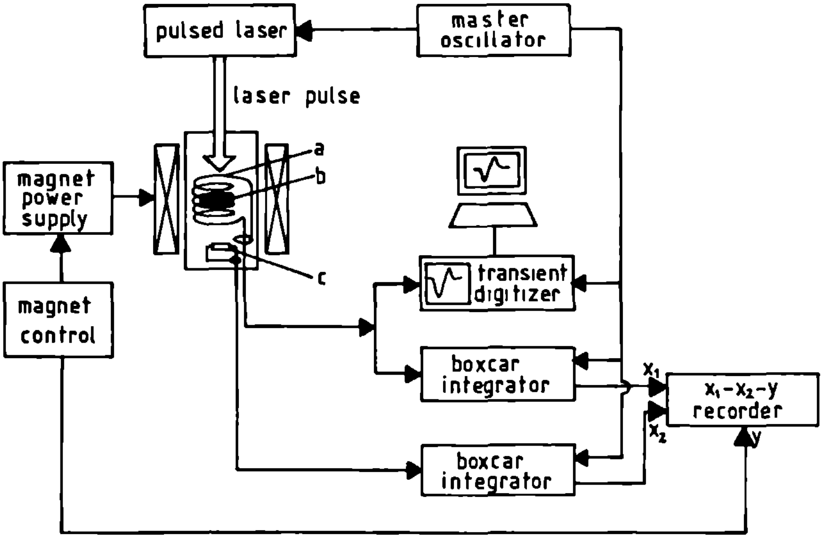

Fig. 4.2 *Experimental arrangement as used for measuring the SLR time: (a) pick-up coil; (b) sample; (c) bolometer for transmission measurements.*

The experimental arrangement that was used to measure the SLR rates is shown in Fig. 4.2. The perturbation of the spin system was realised by a pulsed FIR radiation source which was the optically pumped pulsed FIR laser as has been described in chapter 2. With this system, dependent on the wavelength, light pulses of a duration of about 100 ns can be generated. In the present experiment, radiation was applied with wavelengths of 1202 μm (8.3 cm^{-1}) and 1218 μm (8.2 cm^{-1}) obtained by optical pumping $C^{13}H_3F$, resulting in typical pulse energies of a few μJ. Both wavelengths are simultaneously produced in the laser. For a spin system with a g-factor of 2 the photon energies lead to an EPR resonance at a magnetic field of about 8.8 T. The FIR radiation was sent through an oversized waveguide and focussed onto the sample by a cone. To be able to perform transmission measurements, a bolometer made of an Allen Bradley carbon resistor was placed under the sample. The pick-up coil was fixed around the sample with its axis parallel to the external magnetic field. By the use of low-pressured helium gas the whole arrangement was in thermal contact with a liquid-helium bath. The temperature could be controlled by either pumping this bath or using a heater-resistance.

The voltage induced in the pick-up coil is amplified by a cooled field effect transistor (FET) which is placed as close as possible to the coil to minimise the noise. Therefore this FET is operating almost at the same field and temperature conditions as the sample. After further amplification at room temperature, the voltage induced in the pick-up coil is detected either with a transient digitiser (Tektronix 7912 AD) in order to observe its time evolution or is integrated by a boxcar (PAR 162). The integrated signal allows the observation of magnetisation changes caused by the FIR radiation when the external magnetic field is swept. The signal from the transmission also was integrated by a similar boxcar and was recorded simultaneously.

The present measurements were done with mixed crystals of $Cd_{1-x}Mn_xTe$ with x=0.005. In Fig. 4.3 simultaneously recorded coil signal and the bolometer (transmission) signal are presented as a function of the magnetic field around the EPR resonance field. The two minima seen in transmission are due to the EPR absorption at fields corresponding to both laser-lines. Their positions lead to a g factor of 2.00 ± 0.01, in agreement with other experiments [4,12,13]. At the same values of the magnetic field a strong signal is induced in the pick-up coil, which shows clearly that the observed signal from the pick-up coil is due to the magnetisation changes caused by the EPR.

From the transmission data and the known FIR pulse energy, the number of absorbed FIR photons under EPR condition can be estimated (Fig. 4.3). Assuming that each absorbed photon is exciting one transition between spin levels, the number of "inverted spins" at the resonance field of

8.8 T is about $5\cdot10^{14}$, causing a relative change of the magnetisation of the order of 0.1%, which was consistent with the expected value deduced from the pick-up coil signal. The expected signal could be deduced using

$$V(t)=L\cdot\frac{dM}{dt} \tag{4.1}$$

where L is the inductance of the pick-up coil ($L\propto a^2n^2/l$, where a is area and l is the length of the coil and n is the number of turns).

For the time-resolved measurements the response of the pick-up coil was analysed at a fixed magnetic field. The pick-up coil signal was averaged over typically 1000 laser pulses with the transient digitiser. In the inset of Fig. 4.4 the total response of the pick-up coil is shown as measured at EPR resonance. Clearly, the two processes can be distinguished. The first process involves the lowering of the magnetisation due to resonant EPR absorption and therefore, a pronounced negative signal is produced. The second process is due to the relaxation of the magnetisation and, consequently, the sign of the response is changed.

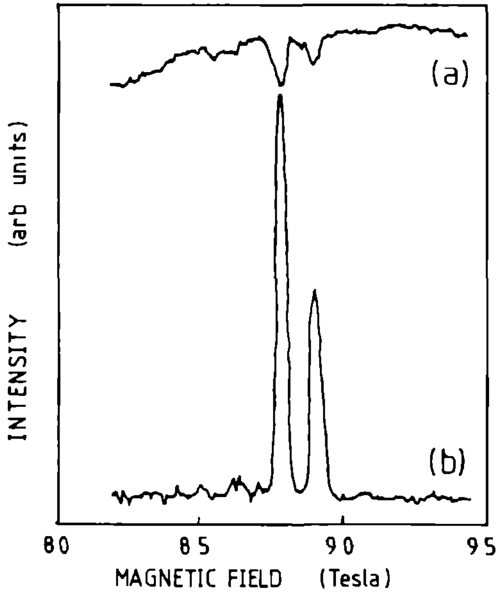

Fig. 4.3 *EPR of $Cd_{0.995}Mn_{0.005}Te$ with FIR excitation wavelengths of 1202 μm and 1218 μm: time integrated (a) transmission and (b) induction signal of a pick-up coil as function of the magnetic field.*

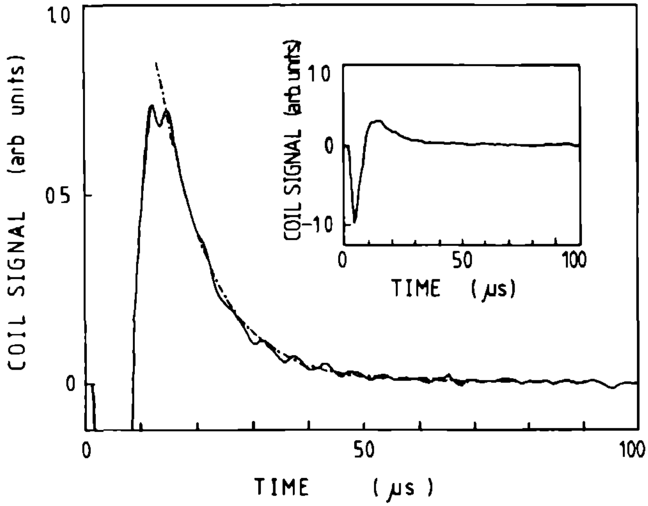

Fig. 4.4 *Time evolution of the pick-up coil signal of* $Cd_{0.995}Mn_{0.005}Te$ *for the 1218 μm laser line EPR resonance at 8.8 T using a coil circuit with a resonance frequency of 52 kHz. In the inset, the full coil response on the FIR excitation is presented. The main figure shows the positive part of the signal that is due to the relaxation of the magnetisation. The dotted line represents a exponential fit.*

In principle, the temporal behaviour of the response due to the first process should be as long as the FIR pulse is available. However, the coil is part of a critically damped RLC-circuit, where R is the damping resistance and C the combination of stray capacitances and the coil capacitance, and L is the coil inductance. The width of the minimum (5μs; inset Fig. 4.4) depends on the response time of the circuit which has resonance frequency ν with $\nu^2 \propto 1/(LC)$. Several coils have been constructed with a typical wire diameter of 30 μm wound on a brass or hysol body with an inner bore diameter of 4 mm. A 6000 turn coil with an inductance L=136 mH showed a resonance frequency of 52 kHz. A second coil with 600 windings achieved a resonance frequency of 613 kHz (L=350 μH). Additionally, pick-up coils with 60 and 6 turns were constructed having resonance frequencies of 6 and 160 MHz respectively and induction of 20 and 0.5 μH. With the fastest coil the signal from the pulsed EPR excitation folows closely the shape of the laser pulse.

However, such a configuration is not sensitive enough to detect the slow magnetisation relaxation which is characteristic of the sample which was used. For a slower but more sensitive coil-circuit which has a higher inductance L, the part of the signal coming from the magnetisation relaxation has a width determined only by the response time of the circuit, as is the case shown in Fig. 4.4. From this part of the data, the relaxation time can be obtained directly by an exponential fit to the response as is shown in Fig 4.4. In a later section a study of the temperature dependence of the SLR time obtained with this technique will be presented.

4.3 Samples

In EPR studies, the wide-gap semiconductor $Cd_{1-x}Mn_xTe$ is a widely used dilute magnetic semiconductor (DMS), whose low-temperature magnetic properties have recently been subject of various experimental and theoretical investigations [8,9]. Due to a partially filled $3d^5$ shell, the Mn^{2+} ions posses a total electron spin of S=5/2 which is six-fold degenerate. Application of a magnetic field lifts this degeneracy and optical transition can be induced if the selection rule $\Delta S_z=1$ is obeyed. This DMS is very well suited for the study of the whole variety of magnetic interactions as a function of Mn^{2+} concentration. It is noted that the pure CdTe crystal, however, has a different crystal lattice (zincblende fcc) than pure MnTe (hexagonal). Therefore, to be able to study the properties of the manganese atoms in an undisturbed lattice, the fraction of manganese atoms, x, is limited between 0 and 0.7. In the case of very small concentrations ($x<0.0001$) the magnetic ions are well separated in the nonmagnetic host lattice and EPR of single Mn^{2+} is observed [12]. For medium concentrations ($0.005<x<0.02$) interactions between neighbouring spins become important. At high concentrations spin-glass-like phase behaviour has been reported and also antiferromagnetic ordering for the very high concentrations [14].

For these medium concentrations, the EPR is broadened by dipolar interaction and exchange pairs of nearest neighbours (NN) are formed [13]. The NN energy will be proportional to $-2J_1S_{z1}S_{z2}$ in which J_1 is the Heisenberg ferromagnetic exchange parameter; this energy equals about 10 Kelvin. At magnetic fields of about 10 Tesla, the electronic Zeeman splitting becomes larger than the exchange energy J_1, level crossing occurs and the ground state changes from the S=0 nonmagnetic singlet to the S=1, m=-1 state of the triplet. This NN-state has a magnetic moment and can also be excited at arbitrary low temperature. This level crossing at high fields has also been observed [15,16] as steps in the sample magnetisation at corresponding magnetic fields. It has been concluded from lineshape studies [9] that these NN pairs have fast relaxation times to the lattice and that because of possible spin-spin relaxation from single spins to pairs or clusters a very effective "by-pass" for relaxation to the lattice can be achieved. Therefore, at these and higher concentrations of Mn^{2+} the relaxation process becomes very complicated. As a consequence, in the present experiment samples were used with a rather lower concentration of Mn^{2+} ions in order to prevent this effect.

The single crystals of $Cd_{1-x}Mn_xTe$, used in the experiment, were grown by a modified Bridgeman technique at the institute of Physics in Warsaw and the concentration of Mn^{2+} was known from the crystal growth ($x=0.005$). To overcome possible deviations from the low Mn^{2+} concentration due to an inhomogeneous composition caused by segregation during the crystal growth, the concentration was checked by an electron microprobe analysis. This resulted in a value of $x=0.002\pm0.001$, which is about half the value from the crystal growth. At this concentration the expected amount of pairs is about 1%.

4.4 Results and Discussion

The relaxation of magnetisation gives rise to an induced voltage with a sign opposite to the signal induced by the EPR absorption. Since the magnetisation after the FIR pulse relaxes exponentially, the induced voltage behaves likewise. From this part of the data (Fig. 4.4) the relaxation time can be directly obtained.

In the present experiment the relaxation time has been measured as a function of sample temperature, between 3 and 25 K. To cover the different time regimes, two different pick-up coils were used with resonance frequencies of 52 and 613 kHz, respectively. In Fig. 4.5 the resulting relaxation times are plotted against sample temperature. As is shown in this figure, the relaxation times as measured with both pick-up coils overlap. It is noted that for the measured SLR times no dependence of FIR laser power has been found.

However, a clear dependence on temperature is observed. The fact that the relaxation time reduces strongly as the temperature is increased can be explained by noticing that the mechanism of the relaxation is dependent on the phonon density, which increases as the temperatures get higher. As was firstly assumed by Kronig and van Vleck (eg. ref. 17), the spin-lattice relaxation mechanism is based on the modulation of the crystalline field due to lattice vibrations. An electrostatic field at the paramagnetic ion site arises in

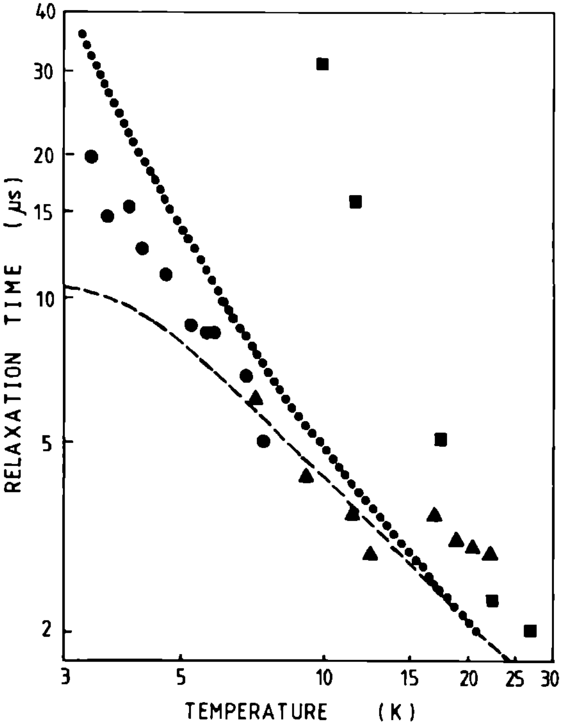

Fig.4.5 *Temperature dependence of the SLR time for* $Cd_{0.995}Mn_{0.005}Te$ *at 8.8 T. as measured by a pick-up coil. Circles correspond to a coil with resonance frequency of 52 kHz, triangles to 613 kHz. Squares are data points from ref. 5, obtained by another method and at lower magnetic fields. The dashed and dotted lines are simulations as discussed in the text.*

ionic crystals from the effect of charges of the neighbouring diamagnetic ions. If these ions are moving due to lattice vibrations, the crystalline field will be modulated, perturbing the orbital motion of the paramagnetic electron and inducing spin transitions through spin-orbit coupling. On grounds of the fact that the Mn^{2+} has no orbital momentum in the ground state, this state in principle should not be affected by the crystal field. However, by admixtures of higher lying states with nonzero orbital momentum, this condition was overcome following the suggestion of M. Blume and R. Orbach [18].

Several SLR relaxation processes with characteristic temperature and magnetic field dependence are distinguished [2]: the direct process which is a one-phonon process and two-phonon processes such as Raman, Orbach and two-phonon emission. The Raman process involves the absorption of one phonon and emission of another one with different energy. The intermediate state is virtual. In the case of the Orbach process the intermediate state should be real. Because excited states with low energy separation from the ground state are not widely available, the efficiency of this process is low.

To find a more qualitative explanation of the temperature effect on the SLR time, as obtained from our data, a simple model is assumed including only two spin levels, which is a reasonable approximation for low temperatures.

If the relaxation is due to single phonon emission the relaxation will be most effective for phonons with an energy equal to the electronic Zeeman energy. From the fact that phonons are described by Boson theory, emission into or absorption from a phonon distribution is more efficient when more phonons are available. From textbooks it can easily be shown that considering the Boltzman distribution, the density for phonons with frequency between ω and $\omega + d\omega$, $D(\omega)$, is proportional to

$$D(\omega) \propto \frac{\omega^2}{e^{\hbar\omega/kT} - 1} \tag{4.2}$$

It can be assumed that the temperature dependence of SLR rate, $1/\tau$, should in zero order follow equation (4.2), resulting in an expression for τ:

$$\tau \propto e^{\hbar\omega/kT} - 1 \tag{4.3}$$

The dotted line in Fig. 4.5 gives a τ as defined by equation (4.3), which is arbitrarily scaled at one point (25K) with an $\hbar\omega$ equal to the photon energy.

If also reexcitation of spins due to single phonon absorption is taken into account, which in principle is necessary for a pure two level system, the expression for the SLR time [19] will then be

$$\tau \propto 1/(\coth(\hbar\omega/2kT)) \tag{4.4}$$

The dashed line in Fig. 4.5 gives the temperature dependence of τ as according to this equation (4.4), under the same conditions as the dotted line in Fig. 4.5. has been obtained.

Both expressions do not completely fit to the data for low temperatures, although they give a qualitative explanation for the higher temperature part. In principle, equation (4.4) should be most valid. However, if an additional relaxation "by-pass" by pairs [13] (1%) is speculated upon, as mentioned in the previous section, the temperature dependence could be qualitatively adjusted. This can be understood by considering the effect that the relaxation process in high fields can be enhanced by cross relaxation with pairs. However, for the present experimental conditions the ground state of the pairs is not the optically active S=1, m=-1 state but the S=0 nonmagnetic singlet state. Therefore, a temperature freeze-out of the S=1, m=-1 state could be anticipated in the inverse-coth-graph (equation (4.4)), which would reduce the effect of this fast "by-pass" as the temperature decreases. This would straighten the dashed line in Fig. 4.5, resulting in a better fit with the data.

An other effect which could induce a better fit to the data is the fact that under low temperature conditions the specific heat of the $Cd_{1-x}Mn_xTe$ ($x \simeq 0.005$) crystal is decreasing strongly and may be comparable with the specific heat of the Mn^{2+} spin system [20]. As a consequence, at low temperatures the lattice temperature will not stay constant during the spin relaxation and the SLR time is no longer well defined as function of temperature. Under this condition the phonon spectrum is no longer in equilibrium and emitted phonons may be diffused into the phonon distribution before reexcitation of a spin. As a consequence it is expected that equation (3) would be more valid. Considering the heating-up of the lattice for lower temperatures, during the relaxation, it may be clear that the experimental value of the SLR time at a certain bath temperature will correspond to a theoretical value at a somewhat higher lattice temperature. This correction will reduce the mis-fit on the low temperature side of the simulation of equation (4.3) in Fig. 4.5.

The measured values for the SLR time can be compared with data received by different low field methods. These data about the spin dynamics of CdMnTe are available from, for example, dynamic susceptibility measurements [5]. The resulting SLR times as deduced by this technique, for comparable samples and for magnetic fields smaller than 4 Tesla, are inserted in Fig. 4.5. The temperature dependence of the SLR time is given by $\tau \propto T^{-2}$ [5]. These data do not fit with above theory. However, it is noted that the phonon densities at the energy of the electronic Zeeman energy in these experiments are much lower than at high fields. Therefore, relaxation processes involving two phonons become more likely. As has been mentioned above, a prominent two phonon process is the Raman process (inelastic diffusion of one phonon) with $\tau \propto T^{-6}$ or T^{-7}, which has been identified in lightly doped CdS [5,19]. The present data, however, are too limited to justify a more detailed discussion.

From the difference in magnetic field depence of the SLR time between the different single- or two-phonon relaxation mechanisms [2], further experiments could resolve the relative importance of several processes. A more extended study of SLR times in $Cd_{1-x}Mn_xTe$, based on the work described in this chapter, can be found in the work of A.M. Witowski and T. Strutz as described in ref. [10]. These workers measured the SLR time as a function of Mn^{2+} concentration, temperature and magnetic field and they analysed the data by considering the relative importance of both the direct one phonon and two phonon Raman process. They concluded that for low concentrations and magnetic fields higher than about 12 Tesla the one phonon process is clearly governing the relaxation process. It is noted that the one phonon approximation for the data discussed in this chapter is, therefore, reasonable.

4.5 Conclusion

The main goal of the present study is to expand spin lattice relaxation measurements into the high magnetic field region by means of the development of a new experimental technique which directly measures the spin relaxation process under pulsed EPR conditions. This technique is based on the measurement of the induction voltage of a pick-up coil around a spin system which is subjected to the pulsed radiation. It has been shown that the time-resolved EPR resonance on the dilute magnetic semiconductor $Cd_{1-x}Mn_xTe$ can be measured by detecting the magnetisation change in the sample as induced by the EPR transition.

Initial data of the SLR time at 8.8 T and at low temperatures can be reasonably explained by one phonon emission, within the experimental limits. Therefore, it is shown that the pick-up coil technique is applicable for SLR time measurements in high magnetic field. The method was sensitive to measure a SLR time for $5 \cdot 10^{14}$ excited spins with a typical time of about 10 μs.

Thus, at high fields, this technique allows direct monitoring of the dynamic behaviour of the spins, which is not only restricted to the relaxation process. For high powered pulses with duration much shorter than the spin relaxation mechanisms, this technique, in principle, could be sensitive to the time-resolved EPR absorption measurements. Applying pick-up systems with sufficiently high frequencies, studies may be performed of the spin-photon interaction to probe Rabi-like oscillations of the magnetisation (see also Appendix) rather than the spin-phonon interaction.

4.6 Appendix

As mentioned in the introduction, an other direct way of measuring the SLR time under EPR condition is the use of multi-pulse techniques to excite electron-spin-echoes [6,11]. Sequences of two or three pulses may be applied for the study of spin lattice relaxation times, T_1, or spin-spin relaxation times, T_2. Utilising these pulse sequences together with pulsed electrical fields or lasers provides a powerful tool for the measurement of perturbation of molecular symmetries or the study of photochemically induced radicals respectively [21,22]. For low field application this technique has been well developed because of the high quality and availability of microwave techniques which are necessary to obtain the pulse trains which can satisfy the experimental limits. Although the applied magnetic field is an important parameter for the spin-correlated effects, high field application of ESE techniques however, have been obstructed due to the lack of equipment which could provide and detect the well defined electro-magnetic wave pulse sequences. It is noted that at high magnetic fields the electro-magnetic wave which is necessary to achieve EPR is in the FIR region of the spectrum.

Nevertheless, in order to achieve a better understanding of the mechanisms involved in an ESE experiment and to survey the present state of the art and the problems in FIR ESE at high magnetic fields, in the following a classical vector model for two-pulse ESE will be presented. Additionally, an experimental feasibility in the case of two pulses of λ=496μm as have been obtained by the laser system, as explained in section 2.6 Fig. 2.8. will be presented.

A single spin in a magnetic field B_0 will in the ideal case precess around the the field axis with a frequency ω_0 (Larmor frequency). In a real physical environment however, each spin will precess at its own Larmor frequency ω_i around the center frequency ω_0. This means that the EPR line as observed will be inhomogeneously broadened, and can be considered as composed of "homogeneous spinpackets" each having a Larmor frequency ω_i (see Fig. 4.6) [23]. The precession frequency ω_i is given by $\omega_i' = \gamma B_i - \omega_0$, where B_i is the effective magnetic field at the site of spin packet "i". Due to the fact that all individual spin-magnetic moments belonging to spinpacket "i" precess with ω_i but with random phase, the resulting magnetic moment of every spinpacket, in steady state, will be aligned along B_0. The effect of FIR radiation with a frequency ω_0 incident parallel to the B_0 direction (i.e. polarised in the x-y plane) on the spin system will now be discussed in a classical way. The oscillating B_1-field of the FIR radiation can be decomposed into two counter rotating components: one is rotating in the same direction as the Larmor precession of the spins and hence, in the rotating frame this B_1 is a steady field, defined along the x-axis (Fig.4.7a); the second component will rotate at double frequency in the rotating frame and may be neglected. If the

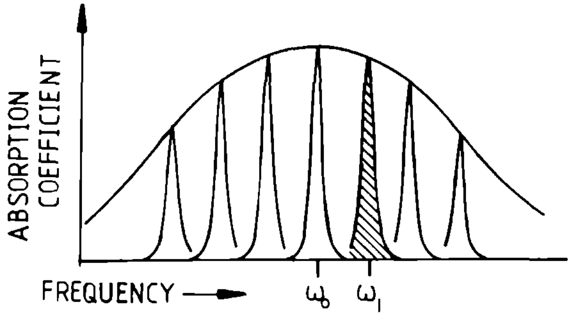

Fig. 4.6 *For a paramagnetic center in a solid the EPR line is inhomogeneously broadened. Individual spin packets have linewidths of the order of 1mG.*

intensity of the FIR radiation is sufficiently high the resultant magnetic field in the rotating frame is oriented along B_1 for all spin-packets. This new effective field B_1 will force the magnetisation M_i to precess around the x-axis. When the FIR pulse is long enough to flip the magnetisation M_i into the x-y-plane, the pulse is defined as a 90^0 or $1/2\pi$ pulse. In the laboratory-frame this can be seen as a magnetisation which rotates with a frequency ω_0 which gives rise to "coherent spontaneous emission" [24]. For ω_0<1GHz this rotating magnetisation can be detected by pick-up coil systems [25,26], however for higher frequencies microwave cavities are necessary to detect magnetic dipole radiation [21]. Since the different spin-packets in the rotating frame have different frequencies ω_i', they start to dephase immediately after the pulse (Fig. 4.7b). This process is called the Free Induction Decay (FID) which in typical ESE-applications will be complete in several tens of nanoseconds.

From this FID an echo can be generated due to a second FIR pulse which is applied after a waiting time τ and which rotates the spins over 180^0 (Fig. 4.7c). This π-pulse results in a reflection of the dephased pattern in the x-z-plane (Fig. 4.7c), and therefore, it is expected that the spin-packets rephase after the same waiting time τ and as such produce an echo. This echo is called the "two-pulse" or "primary" echo (Fig. 47d) [23]. By monitoring the intensity of this echo as a function of τ a method is offered to measure the "phase-memory time" or homogeneous T_2 of the spin system under the condition that other relaxation processes (eg. spin-lattice relaxation, T_1) are not influencing the result.

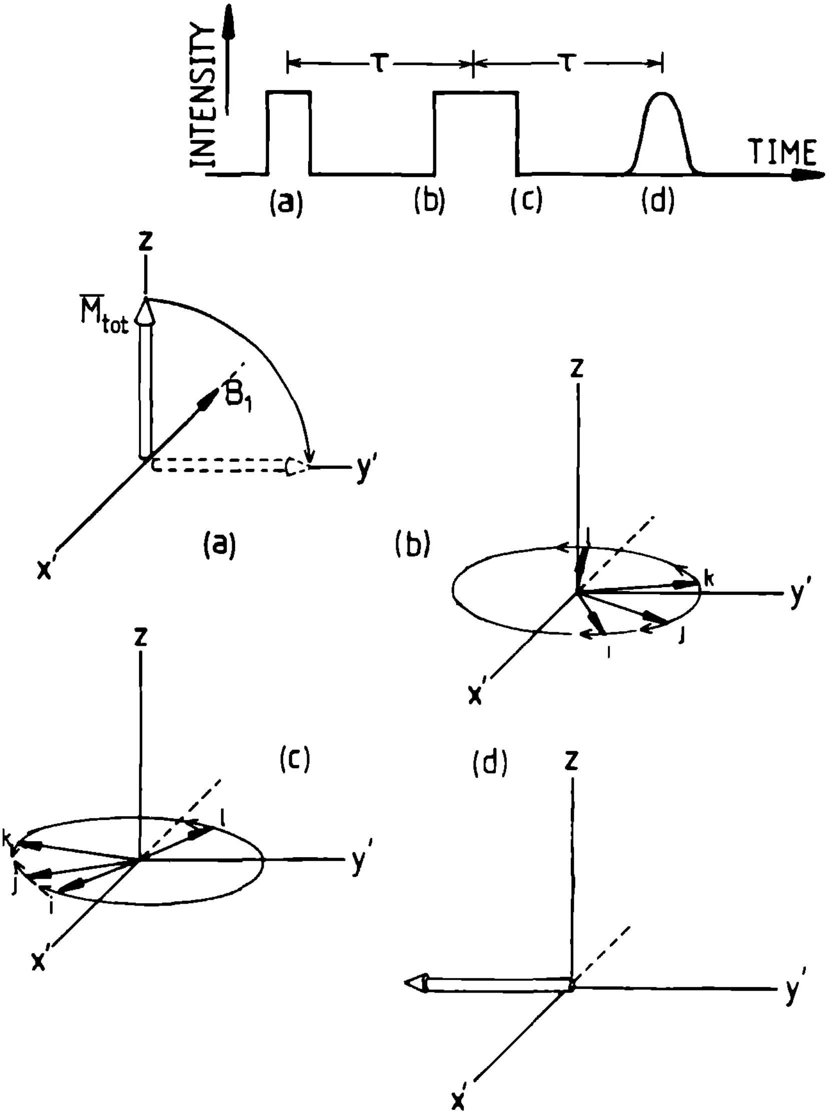

Fig. 4.7 *Magnetisation of spin packets during a two pulse experiment. a) during* $1/2\pi$ *pulse; b) during waiting time* τ*; c) after* π*-pulse; d) echo at time* τ *after the last pulse. The coordinates of the rotating frame are indicated by* x'*,* y' *and* z*.*

It is noted that the existence of inhomogeneities in the spin system is essential for the echo phenomenon. Further, the maximum echo intensity is obtained with the 90^0-180^0 sequence of pulses. However, if different pulse lengths are applied an echo may be detected due to the fact that there are components of the dephasing pattern which can contribute.

In the case of pulses with a wavelength λ=496μm (chapter 2.6) which have an EPR resonance for spins with g=2 at about 21.6T, the magnetic field ,B_1, due to the FIR laser radiation to achieve a $1/2\pi$ pulse of 10ns can be calculated, considering [1]

$$\gamma B_1 \cdot 10\text{ns}=1/2\pi \tag{4.5}$$

to be about 10 Gauss, which implies a laser power of $P=c/2\mu_0\ B_1^2 \simeq 1.3 \cdot 10^8$ w/m². Considering a sample with an area of 10mm² this will lead to a laser power of 1.3 kW, which at this moment is available (see chapter 2.6). Such a pulse will consist of $4 \cdot 10^{16}$ photons. However, due to the fact that the B_1 field should not be affected by the transfer of energy from the pulse into the spin system, the amount of spins is much smaller than this number. If the spin system is considered small in comparison with the wavelength, the rotating macroscopic magnetic moment "m" may be considered as two perpendicular magnetic-dipole oscillators, for which the radiated power is defined as [27]

$$P=\left(\frac{16}{3}\right)\cdot\left(\frac{\pi^4 c}{\lambda^4}\right)\cdot m^2 \tag{4.6}$$

If 10^{13} spins are taken into account this would yield an emitted power of 2mW. Because the radiated energy comes from the energy of the spin system in the magnetic field this power will induce a loss of 10^{10} spins per ns of radiation. Such low pulse powers, in principle, can be detected by using tuned Schottky-diodes which have sensitivities of less than a μW. An experimental problem however, is that this high sensitivity should be available shortly after the main kW pulses. In principle, shielding of the detector can be obtained by means of optical switches as discussed in chapter 2.3.

It may be concluded, therefore, that ESE will be possible in high fields, although still some technical obstacles have to be tackled, which may be realised in the near future.

References

[1] C. Kittel, *Introduction to Solid State Physics*, p. 466 (John Wiley & Sons, New York, 1986)

[2] A. Abragam and B. Bleany, *Electron Paramagnetic Resonance of Transition Ions*, p. 123 (Clarendon Press, Oxford, 1970)

[3] M.K. Bowman and L. Kevan in *Time Domain ESR*, p. 67, edited by L. Kevan and P.N. Schwatz (John Wiley & Sons, New York, 1979).

[4] R.E. Kramer and J.K. Furdyna, Phys. Rev. B **32**, 5591 (1985).

[5] D. Scalbert, J. Cernogora, and C. Benoit a la Guillaume, Solid state Commun. **66**, 571 (1988); *Proceedings of the 19th International conference on Physics of Semiconductors*, p. 1547, edited by W. Zawadski (Polish Academy of Science, Warsaw, 1988)

[6] A. Schweiger and R.R. Ernst, Journal Magn. Res., 77, 512 (1988)

[7] G.J. Jongerden, A.F. Arts, J.I. Dijkhuis, and H.W. de Wijn, Phys. Rev. B 39, 6355 (1989)

[8] J.K. Furdyna and J. Kossut, *Semiconductors and Semi-metals*, Vol. 25 (Academic Press, Boston, 1988).

[9] J.K. Furdyna, J. Appl. Phys. **64**, R29 (1988), and references therein.

[10] T. Strutz, thesis, Konstantz (1991), unpublished.

[11] W.B. Mims in *Electron Paramagnetic Resonance*, p. 263, edited by Geschwind (Plenum Press, New York, 1972).

[12] R.E. Kramer and J.K. Furdyna, Phys. Rev. B 31, 1 (1985).

[13] L.M. Claessen, A. Wittlin, and P. Wyder, Phys. Rev. B **41**, 451 (1990).

[14] A. Wittlin, L.M. Claessen, and P. Wyder, Phys. Rev. B 37, 2258 (1988).

[15] B.E. Larson, K.C. Hass, and R.L. Aggerwal, Phys. Rev. B 33, 1789 (1986).

[16] E.D. Issacs, D. Heiman, P. Becla, Y. Shapira, R. Kersaw, K. Dwight, and A. Wold, Phys. Rev. B **38**, 8412 (1988).

[17] K.W.H. Stevens, Rep. Prog. Phys. **30**, 189 (1967).

[18] M. Blume and R. Orbach, Phys. Rev. 127, 1587 (1962).

[19] S. Geschwind, *Electron Paramagnetic Resonance* (Plenum Press, New York, 1972).

[20] R.R. Galazka, Shoichi Nagata, and P.H. Keesom, Phys. Rev. B 22, 3344 (1980).

[21] E.J. Reijerse, thesis, Nijmegen (1986), unpublished.

[22] J. Schmidt and D.J. Single, Ann. Rev. Phys. Chem. **38**, 141 (1987).

[23] E.L. Hahn, Phys. Rev. **80**, 580 (1950).

[24] R.H. Dicke, Phys. Rev. **93**, 8 (1954).

[25] N. Bloembergen and R.V. Pound Phys. Rev. **95**, 8 (1954).

[26] F. Bloch, Phys. Rev. **70**, 460 (1946).

[27] J.D. Jackson, *Classical Electrodynamics*, p. 396, (John Wiley & Sons, New York, 1975).

CHAPTER 5

FAR INFRARED ASSISTED TUNNELLING IN DOUBLE BARRIER RESONANT TUNNELLING STRUCTURES

ABSTRACT

The influence of far infrared radiation on the tunnel current of GaAs/AlGaAs double barrier resonant tunnelling devices has been investigated for well structures of different widths and as a function of bias voltage and different far infrared photon energies. Analysis of the non-classical response permits a determination of an upper limit of the scattering time in the well. In the samples under study, this scattering time is less than the tunnelling time and therefore tunnelling appears to be mainly sequential.

(Parts of this chapter have been accepted for publication in Appl. Phys. Lett.)

5.1 Introduction

Tunnelling is a pure quantum-mechanical effect which describes the traversing of potential barriers by particles which, classically, do not have enough kinetic energy to do so. For a particle with an energy less than the barrier height a finite probability exists for tunnelling through or reflection from this barrier. However, a special feature of 'resonant' tunnelling exists where for certain energies below the barrier height the electron is completely transmitted and transport through the structure is maximal. This phenomenon was first observed in 1970 [1] in a Double Barrier Resonant Tunnelling Structure (DBRTS) and the interest in resonant tunnelling has been growing since then (see for review Ref.2 and 3). In Fig. 5.1 such a DBRTS structure is schematically shown consisting of a quantum well of GaAs sandwiched between AlGaAs barriers. As also shown in the figure, the transport of carriers through the structure is maximal when the energy level of the emitter coincides with the energy of the quantum well subband. The resulting current-voltage characteristic of such a device, therefore, is highly non-linear as also is shown in Fig. 5.1.

From the point of view of technical applications, these structures can be used for oscillators, due to an intrinsic bistability of the negative differential resistance (NDR) region, and also for mixers of very high frequency, microwave amplifiers and fast transistors [4,5]. However, on the fundamental level, these structures offer an excellent system for the study of problems regarding tunnelling and discrete levels in quantum wells.

Although at first the description of electron transport through a DBRTS may seem like a simple textbook problem, the modeling of devices based on this structure has not been fully successful [6-10]. For example, the fundamental mechanism which produces the NDR region in these structures is still under discussion. Tsu and Esaki considered the effect as a coherent process similar to the Fabry-Perot etalon in optics [1] in which the electron spends a certain time inside the well, being multiply reflected in the barriers, before leaving the structure. Luryi [6] proposed that the NDR arrises from a sequential process in which electrons first tunnel from the emitter electrode into the quantum well and subsequently from the well to the collector. Between these two steps the electron phase memory may be completely lost and hence it was suggested that a resonant enhancement of the transmission coefficient was unnecessary. Although several authors have treated this problem theoretically [6-10] an experimental determination of the dominant tunnel mechanism is still an unsolved problem.

In this chapter, an experimental method is proposed to distinguish between coherent and sequential tunnelling, by means of the study of the response of the tunnel current to far infrared (FIR) radiation. This is based on the fact that the timescale of the FIR period is comparable to the tunnel-

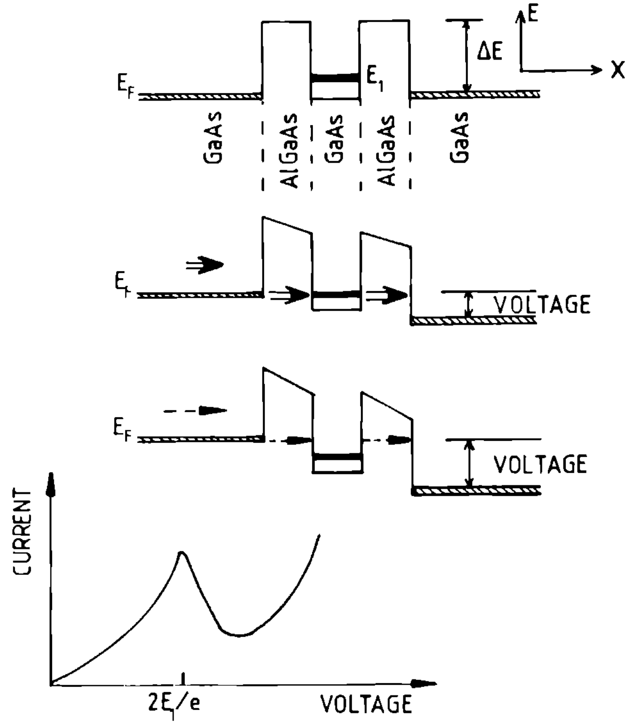

Fig 5.1 *Spatial variation of the electron potential energy through a DBRTS, showing a bound state,* E_1*, and the Fermi levels,* E_F*, as a function of applied voltage, and the resulting current-voltage characteristic.*

ling times for the different processes. The definition of the tunnelling time is one of ongoing scientific discussion [11]. It is noted that two 'times' can be distinguished which characterise the tunnelling processes. One is the characteristic coherent tunnelling time, τ_c, which essentially is the time that an electronic wave spends inside the well, being multiply reflected by the barriers, before leaving the structure. This τ_c can be defined as $\hbar/\Gamma$, where Γ is the full width at half maximum energy of the calculated, energy dependent, transmission coefficient for a certain structure. The coherence of the wavefunction, however, may be destroyed by collisions which can be characterised by a typical scattering time, τ_s. This scattering includes both elastic scattering by carriers, impurities, inhomogeneities in the layer thickness and inelastic phonon scattering. As a consequence, tunnelling is considered coherent for $\tau_c < \tau_s$, and sequential when $\tau_c > \tau_s$.

To be able to distinguish experimentally between both coherent and sequential tunnelling, a third 'time', τ_r (the FIR oscillation period) is introduced in this chapter to the problem. For coherent tunnelling and $\tau_c < \tau_r$ the carrier will not have enough time to interact with the radiation during tunnelling and the current response to the FIR radiation will follow the second derivative of the current-voltage characteristic, due to the classical rectification mechanism [12]. If $\tau_r < \tau_c$ the carrier is expected to interact strongly and the FIR response should be calculated quantum mechanically [13] and will be found sensitive to the radiation energy. For sequential tunnelling, however, no photon energy dependence is expected as long as $\tau_s < \tau_r$ because, due to scattering, a carrier will have no time to interact coherently with the radiation field. Therefore, for $\tau_r < \tau_c$, it will be possible to determine if the tunnelling is dominated by coherent or sequential processes and in the latter case to obtain an upper limit for the scattering time τ_s.

Therefore, in this chapter, an experimental study is presented in which the current response was measured for different DBRTS's as a function of bias and radiation frequency. Results from a study where a 100 MHz voltage modulation was superposed on the bias voltage clearly showed a classical rectification response. The results from FIR radiation (λ=496μm ; τ_r =2.6·10^{-13} s and λ=90.9μm ; τ_r=5.06·10^{-14} s) showed no photon energy dependence and as a result it has been concluded that tunnelling in these devices is dominated by the sequential process and that the scattering time in these samples is shorter than 10^{-13} s.

Finally, another dynamical aspect of these DBRTS devices was observed, which is the intrinsic bistability of the negative differential resistance. For some bias voltages oscillations were observed with frequencies up to 150 MHz and it has been noted that under irradiation with intense FIR the amplitude of these oscillations could be modulated with the shape of the FIR pulse. This effect is explained by the smoothing of the I-V characteristic due to the FIR radiation which reduces the importance of the NDR in comparison with in the DC case.

5.2 Theoretical

It is well known, that a device which shows a non-linear current-voltage characteristic (I-V) can be used as a rectifying element. To describe the rectifying response of such a device, consider a non-linear device which is subjected to a modulated voltage, V_m, at a frequency, ω. Firstly, in the classical limit, i.e. is for frequencies for which the nonlinearities in the I-V characteristic are small on the scale of a voltage $\hbar\omega/e$, the resulting DC current, I_{dc}, under influence of a modulation of the voltage will be given by

$$I_{dc} = \frac{1}{T}\int_0^T I(V(t))\,dt \tag{5.1}$$

where $V(t)=(V_a + V_m\cos\omega t)$, with V_a the applied DC voltage. For low V_m the expansion of the I(V) may hold in the second order and therefore the signal current due to the modulation may be approximated by

$$I_{det} = I_{dc} - I(V_a) = \frac{1}{4}\frac{d^2I}{dV^2}V_m^2 \tag{5.2}$$

where $(d^2I)/(dV^2)$ is the second derivative of I(V) at the bias point V_a. The expected response, therefore, will not be frequency dependent.

In the second case, however, that the nonlinearities in the I-V characteristic on a scale of a voltage $\hbar\omega/e$ are not negligible, a quantum mechanical approach is necessary. The effect of a single photon emission or absorption will now be expected to appear in the response characteristic. For the present case of a DBRTS in the presence of radiation the current density may be determined using the transfer matrix formalism [1,14,15]. In this formalism, assuming the tunnelling is coherent (no scattering), the transmission coefficient as a function of incident energy is obtained by solving the time-dependent Schrödinger equation

$$i\hbar\frac{\partial\psi}{\partial t} = (H_0 + H')\,\psi \tag{5.3}$$

where $H_0 = -\dfrac{\hbar^2}{2m}\dfrac{\partial^2}{\partial x^2} + V_0(x)$ and $H' = V_1(x)\cos(\omega t)$

$V_0(x)$ describes the shape of the quantum well potential and H' gives the AC electric field of the applied radiation perpendicular to the quantum well. The

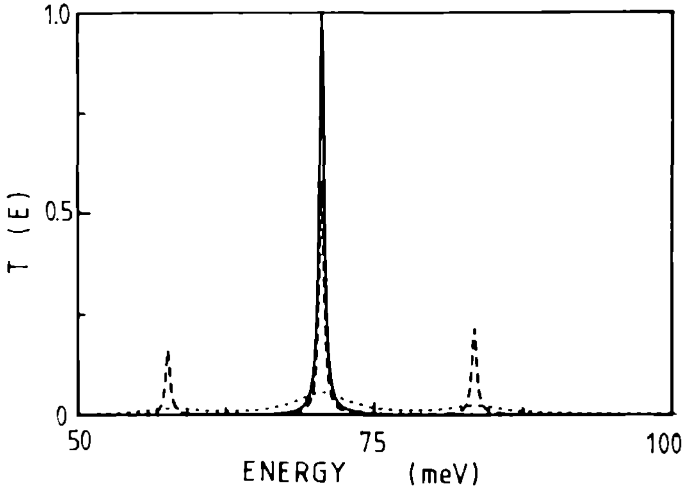

Fig. 5.2 *Calculated transmission coefficient T(E) for DBRTS at zero bias voltage; solid line for coherent tunnelling without radiation; dashed line for coherent tunnelling with applied radiation with* $\hbar\omega = 13$ *meV* $(V_1/\hbar\omega = 0.5)$ *and dotted line for sequential tunnelling* $(\tau_S = 1.32\cdot 10^{-13}$ *s) with applied radiation with* $\hbar\omega = 3$ *meV* $(V_1/\hbar\omega = 0.5)$.

resulting transmission coefficient now shows satellite peaks at energies $\pm\, \hbar\omega$ with respect to the DC transmission peak, where ω is the frequency of the applied radiation. This effect is clearly shown in Fig. 5.2. These satellite peaks correspond to the absorption and emission of a photon. The expected response, therefore, will show a frequency dependence.

V.A. Chitta [16] calculated the current density, J, as a function of the bias voltage for the case of a DBRTS of a 50Å GaAs quantum well between two $Al_xGa_{1-x}As$ ($x \simeq 0.4$) barriers of 50Å each and with both emitter and collector consisting of heavily doped GaAs (10^{18} cm^{-3}), using [15]

$$J = \frac{e}{4\pi^3\hbar} \int_0^\infty dk_l \int_0^\infty dk_t \; (f(E)-f(E')) \; T(E) \; \frac{\partial E}{\partial k_t} \tag{5.4}$$

where T(E) is the transmission function at energy E, E′ is the energy of the transmitted electron, f(E) is the Fermi-Dirac distribution and k_l and k_t are components of the momentum perpendicular to the layers. The result, without radiation, is shown in Fig. 5.3a (solid line). The assymetry can be understood from the change in the shape and energy of the barriers as the applied bias voltage increases. The difference in current density between this unilluminated situation and the equivalent result under the condition of FIR radiation (side peaks in transmission at $\hbar\omega/e$) is plotted in Fig. 5.3b for different frequencies. A clear frequency dependence can be observed in the voltage dependence of the responses.

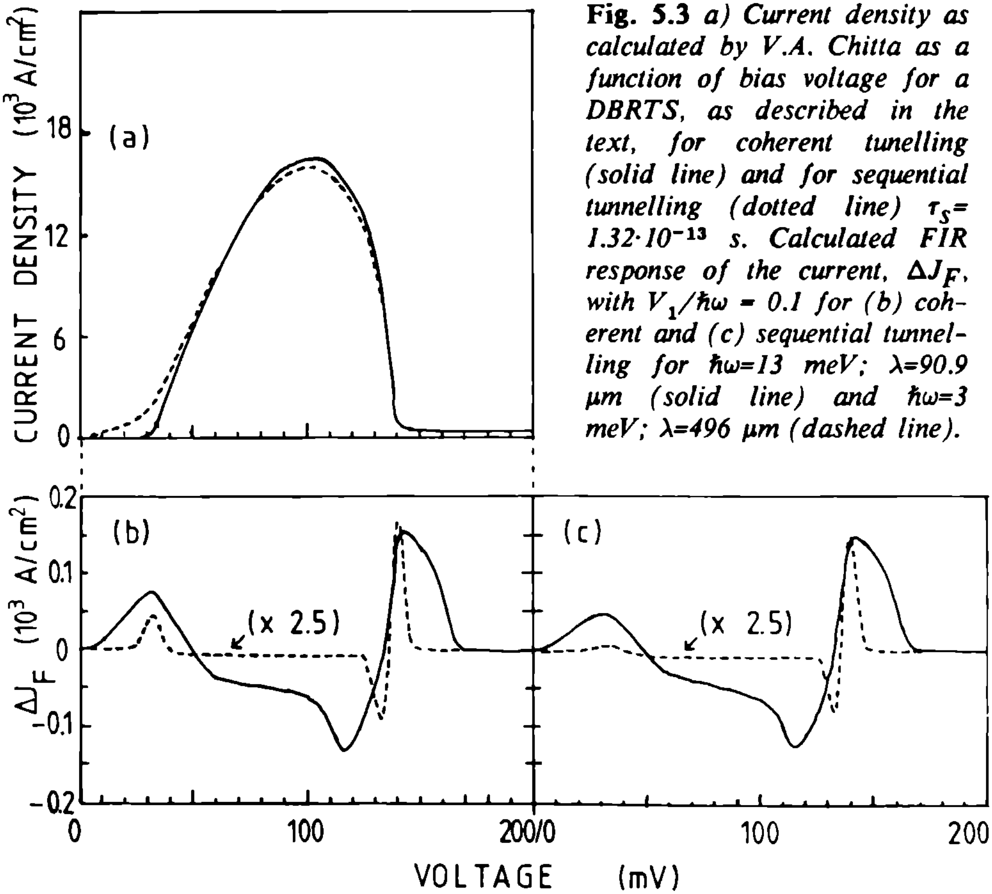

Fig. 5.3 *a) Current density as calculated by V.A. Chitta as a function of bias voltage for a DBRTS, as described in the text, for coherent tunelling (solid line) and for sequential tunnelling (dotted line) τ_S= 1.32·10^{-13} s. Calculated FIR response of the current, ΔJ_F, with $V_1/\hbar\omega$ = 0.1 for (b) coherent and (c) sequential tunnelling for $\hbar\omega$=13 meV; λ=90.9 μm (solid line) and $\hbar\omega$=3 meV; λ=496 μm (dashed line).*

So far, however, tunnelling has been assumed to be coherent. When scattering is introduced, i.e. for sequential tunnelling, the same formalism can be used to obtain the high frequency response, under the condition that the transmisson coefficient is convoluted with a scattering broadening function [17,18] given by

$$S(E,\tau_s) = \frac{1}{\pi}\,\frac{(\hbar/2\tau_s)^2}{E^2+(\hbar/2\tau_s)^2} \tag{5.5}$$

where τ_s is the scattering time including both inelastic scattering by phonons and elastic scattering by impurities, carriers and inhomogeneities in the layer thicknesses. This scattering leads to broadening and decrease of the resonant transmission T(E) and therefore to a broadening and a reduction of the tunnel current as described by equation (5.4). The dashed line in Fig. 5.2 shows a calculated current-voltage characteristic with a scattering time $\tau = 1.32\cdot10^{-13}$ s. The current density at the onset is increased and the peak current is decreased, while the valley current remains unchanged.

Another consequence of the change of T(E) due to scattering is that in the case of FIR radiation, the importance of the satellite peaks (at energies $\pm\hbar\omega$) is strongly reduced because of their broadening and decrease as is shown in Fig. 5.2 (dotted line). In combination with the smoothing of the tunnel current characteristic (Fig. 5.3a) due to scattering, the radiation energy dependence of the current at the onset of the peak is completely destroyed (see Fig. 5.3c), even for FIR radiation with a smaller oscillation period such as $\hbar\omega$ = 13 meV ($\tau_r = 5.06\cdot10^{-14}$ s). Due to the fact that the scattering does not seem to affect the valley current (Fig. 5.3a), the response in this region will stay dependent on $\hbar\omega$.

Therefore, considering this argument, measurement of the FIR response of a DBRTS should offer a possible means to distinguish between coherent and sequential tunnelling by the analysis of the radiation energy dependence of the FIR response.

5.3 Experimental

Three different DBRTS-samples were used in the experiment, all grown by MBE technique. Samples (I), (II) and (III) have a quantum well width of 50 Å, 600 Å and 1200 Å respectively. Apart from the width of the quantum well all the samples have a similar composition as is shown in the layer diagram of Fig. 5.4. All samples have been grown on a GaAs substrate with an electron carrier concentration $n = 2\cdot 10^{18}$ cm^{-3} with a 2 μm thick GaAs buffer layer ($n = 2\cdot 10^{18}$ cm^{-3}). In each case, the quantum wells were sandwiched between a symmetric structure composed of two undoped $Al_{0.4}Ga_{0.6}As$ barriers of 56 Å, two 25 Å thick spacer layers of undoped GaAs and two layers of 500 Å Si doped GaAs ($n = 2\cdot 10^{16}$ cm^{-3}). Finally a layer of 0.5 μm GaAs doped at $n = 2\cdot 10^{18}$ cm^{-3} was grown on top of the structures to connect contacts.

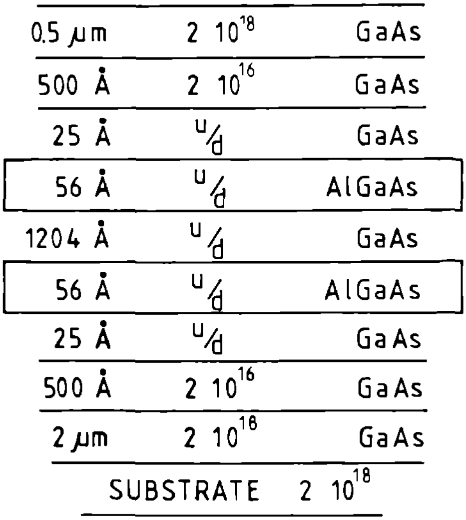

0.5 μm	2 10^{18}	GaAs
500 Å	2 10^{16}	GaAs
25 Å	u/d	GaAs
56 Å	u/d	AlGaAs
1204 Å	u/d	GaAs
56 Å	u/d	AlGaAs
25 Å	u/d	GaAs
500 Å	2 10^{16}	GaAs
2 μm	2 10^{18}	GaAs
SUBSTRATE	2 10^{18}	

Fig. 5.4 *Typical growth diagram for the DBRTS sample #3. The doping concentration for the levels concerned are indicated in cm^{-3}, u/d indicates no intensional doping.*

Square mesas were etched with a size of 200 x 200 μm^2 up to 500 x 500 μm^2 and ohmic contacts were made to the substrate and the top of the samples. To be able to couple the FIR radiation in with the right polarisation, the top ohmic contact has a grating coupler geometry (50 μm periodicity) [19]. For normal incident radiation with $\lambda > 50$ μm this grating induces a spatially modulated electric field with a component perpendicular to the layers, i.e. with the same direction as the bias field and the current. Only this perpendicular component can couple the radiation to the electrons in the well [20]. Because of the low impedance of the DBRTS normal whisker techniques could not be applied. At these frequencies, a whisker may be considered as an antenna which also couples the high frequency signal across the contact; however, it can be represented as a voltage source with an internal impedance R_w which is loaded by the junction. At FIR frequencies, this R_w has a value typically about 150Ω so that the signal across the junction will be current controlled for junction resistances less than R_w.

To determine the current through the samples the voltage over a load resistance was measured. The value of this load resistance was about 1% of the sample resistance in order not to influence the voltage over the sample during the measurement. For the high frequency 100 MHz experiment the current response has been detected after modulation with 100 Hz and by using standard lock-in techniques. For the pulsed FIR responses the data were retrieved by the transient digitiser Tektronix 7912 AD) as has also been used for the experiments described in previous chapters.

5.4 Results and discussion

Typical DC current-voltage characteritics as measured for sample (I) and (III) at liquid Helium temperature are shown in Fig. 5.5. For sample (I) in Fig. 5.5a the valley region of the NDR could not be smoothly resolved as a function of voltage due to the series resistance in the sample itself which leads to the sharp drop in the bias voltage at 0.6 V. For sample (III) some plateau regions can be distinguished in the valley region of the NDR (see Fig.5.5b) for bias voltages higher than 0.35 V. Such a plateau arises when the sample resistance oscillates and only an averaged current can be measured. An explanation for these oscillations can be found in the bistable nature of any device with a negative resistance [3,15,21].

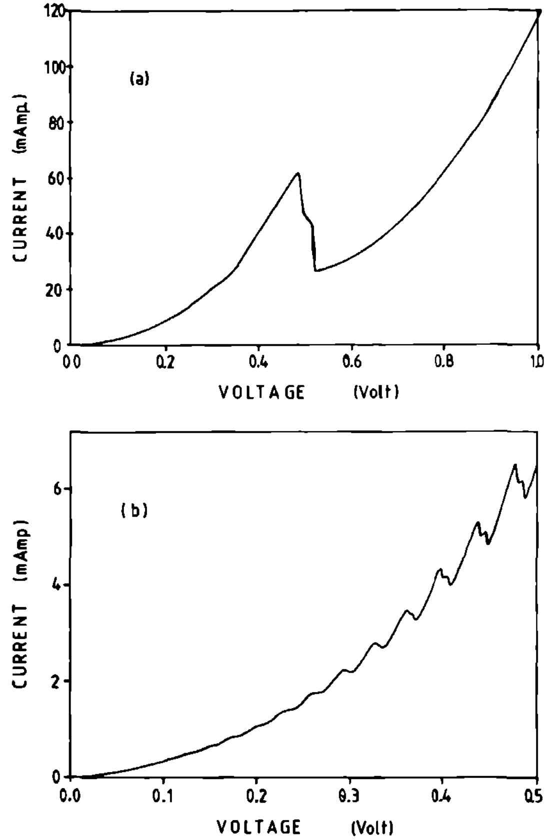

Fig. 5.5 *I-V characteristics of several DBRTS samples: (a) sample (I) with one pronounced resonance; (b) sample (III) clearly multiple resonances can be distinguished.*

5.4.1 100 MHz data

To confirm the classical response of a non-linear device for low frequencies the response of sample (III) was studied as a function of bias voltage for a frequency of 100 MHz. The result of this experiment is plotted in Fig. 5.6 together with the second derivative of the IxV characteristic which was calculated from Fig. 5.5b. Apart from some small off-set signal, the experimental response is completely consistent with the theoretical approach.

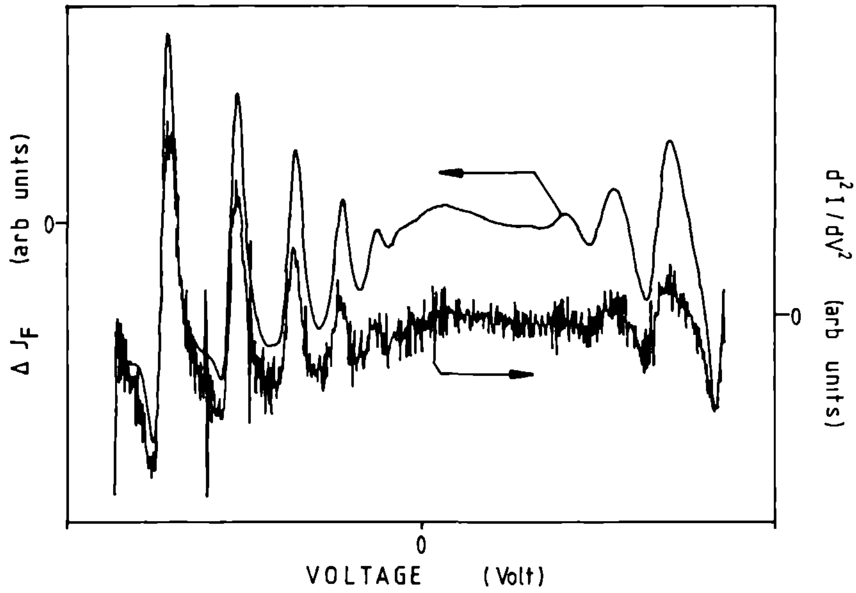

Fig. 5.6 *Current response, ΔJ_F, of sample (III) (solid line) as a function of applied voltage subjected to an oscillating electric field together with the second derivative found from the experimental I-V characteristic (noisy line).*

5.4.2 FIR data

The FIR response study was performed at liquid helium temperature using FIR laser pulses (pulse width 100 ns; power $\geq$ 10 W) with a wavelength in the range $\lambda = 90.9$ μm ($\hbar\omega = 13.6$ meV, $\tau_r = 5.06 \cdot 10^{-14}$ s) up to $\lambda = 496$ μm ($\hbar\omega = 2.5$ meV, $\tau_r = 2.6 \cdot 10^{-13}$ s). The calculated τ_c, assuming coherent tunnelling, is equal to $1.41 \cdot 10^{-11}$ s, $2.53 \cdot 10^{-10}$ s, and $6.47 \cdot 10^{-10}$ s for devices I, II, and III respectively and τ_r is in the range of $2.6 \cdot 10^{-13}$ s up to $5.06 \cdot 10^{-14}$ s. Therefore, the condition $\tau_r < \tau_c$ is satisfied for all the studied devices and consequently no frequency dependence is expected (see section 5.3).

Fig. 5.7a again shows the I-V characteristic for sample (I). Fig. 5.7(b+c) shows the FIR response as a function of bias voltage, for sample (I) with FIR radiation of $\hbar\omega = 13.6$ meV (Fig. 5.7b) and $\hbar\omega = 4.2$ meV (Fig. 5.7c). For both radiation energies, the change in the current presents positive maxima at bias voltages 0.32 V and 1.32 V which coincide with the onsets of the NDR regions of the I-V characteristic and a negative maximum in the I-V valley region (bias 0.6 V). A similar behaviour of the signal current is obtained for both other devices (II) and (III) as shown in Fig. 5.7e ($\hbar\omega = 13.6$ meV) and Fig. 5.7f ($\hbar\omega = 2.5$ meV) for device (III). Due to the large thickness of the quantum well, the I-V characteristic for this device (III) consists of a series of closely separated NDR regions (as shown in Fig. 5.5b). However, for clarity only two of these NDR regions are shown in Fig. 5.7d. Due to the small energy spacing the valley region of the first NDR coincides with the onset of the second NDR. Therefore, the measured current signal shows positive maxima in the valley regions (0.302 V and 0.335 V), while the negative maxima almost coincide with the peak regions of the I-V characteristic (0.291 V and 0.324 V). If some stray resistance in the device, parallel to the tunnel structure, is taken into account, the bias voltages for optimal tunnelling will induce a shift to lower voltage for these peak regions. As a result coincidence will be perfect. The possiblity of such a stray resistance is deduced from the observation that for the same tunnel structure from the same chip different current densities could be obtained with similar contacts.

A first important observation, therefore, is that the current response is never proportional to the second derivative of the I-V characteristic for any of the samples studied. Fig.5.8 shows the second derivative of sample (III) as a function of bias voltage together with the FIR current response. Consequently, classical rectification can not be used to explain the results, which is expected since $\tau_r < \tau_c$ in all cases. A trivial temperature effect is excluded because the measured change in the current with increasing temperature never showed negative values and additionally, the shape of this change is quite different from the observed change.

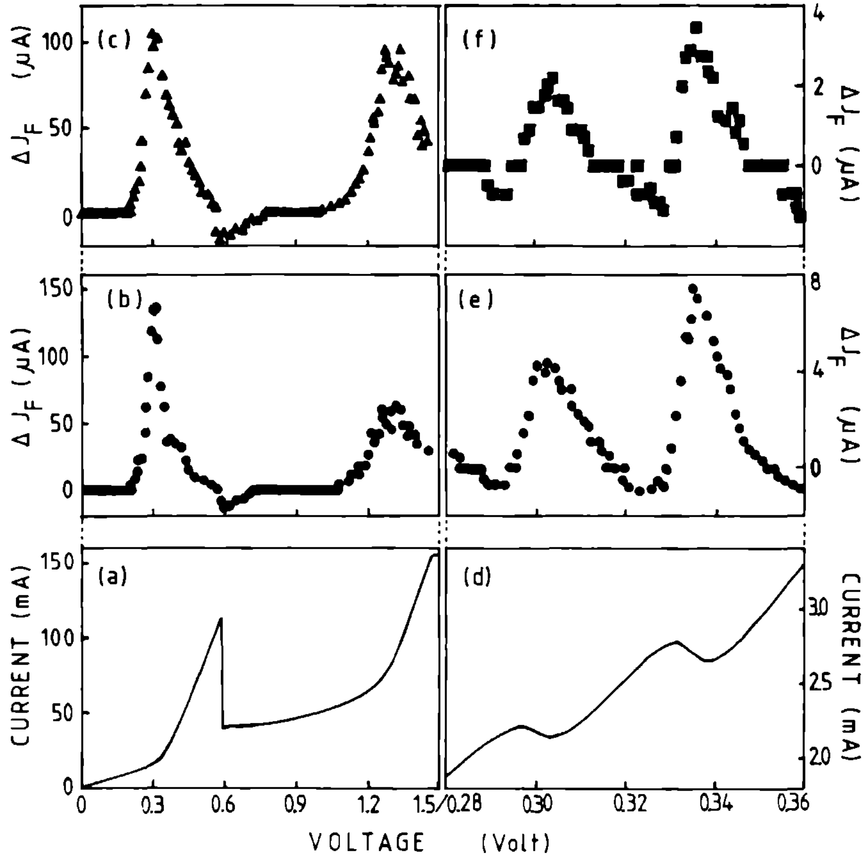

Fig. 5.7 *Measured I-V characteristic and FIR response of devices (I) and (III). (a) I-V characteristic of device (I) at 4.2 K. FIR response of device (I) for (b) ħω=13.6 meV (λ=90.9 μm) and (c) ħω=4.2 meV (λ=292 μm) as a function of bias voltage. (d) I-V characteristic of device (III) at 4.2 K showing two consecutive NDR regions. FIR response of device (III) for (e) ħω=13.6 meV and (f) ħω=2.5 meV (λ=496 μm).*

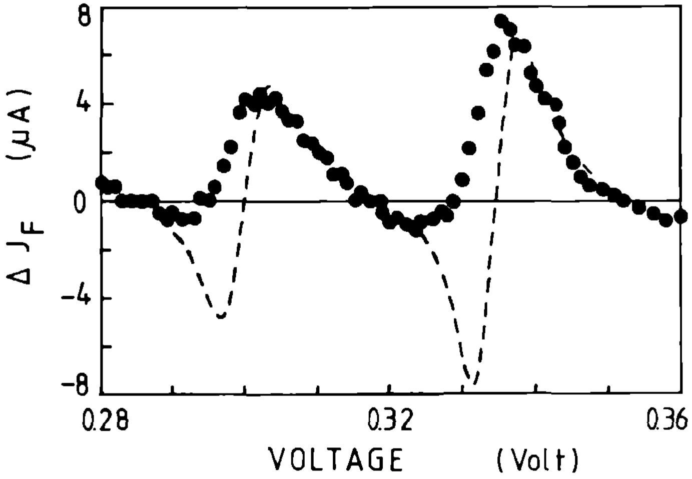

Fig. 5.8 *The second derivative of the I-V characteristic of sample (III) (dashed line) together with the measured FIR response (dotted line) as a function of bias voltage.*

A second important result is that in the FIR responses no radiation energy dependence is observed, which would be expected from the fact that $\tau_r < \tau_c$. As was discussed before, for true photon assisted resonant tunnelling quantum detection would be expected.

To explain these experimental results it seems to be necessary to assume that scattering events are very important for our samples and that $\tau_s < \tau_r$ which implies that tunnelling is mainly sequential. Considering the arguments of section 5.2, it is concluded that the scattering times in these samples are shorter than $1 \cdot 10^{-13}$ s.

5.4.3 Amplitude modulation of oscillations in the NDR region by FIR

The possibility of generating oscillations, as was mentioned before, due to the intrinsic instability of a device with a negative differential resistance, has been one of the main reasons for the renewed interest in resonant tunnelling devices since Sollner et al. demonstrated production of oscillators with frequencies in excess of 400 GHz [21]. Sample (III) could be arranged to oscillate at a frequency of 150 MHz for certain NDR regions (see Fig 5.5b) by using an external capacitor parallel to the device. The measurement of the current response to the pulsed FIR radiation showed a clear influence of the FIR pulses on the amplitude of the oscillations. As is shown in Fig. 5.9 the FIR radiation was able to modulate the amplitude of the oscillations with the shape of the FIR pulse. An argument for a possible explanation of this effect is that the negative differential resistance is reduced due to the smoothing of the I-V characteristic by the FIR radiation. A clarifying example for this statement is shown in Fig. 5.10 where the I-V characteristic of sample (I) is plotted for different values of an oscillating voltage with a frequency of 10 kHz additional to the DC bias voltage.

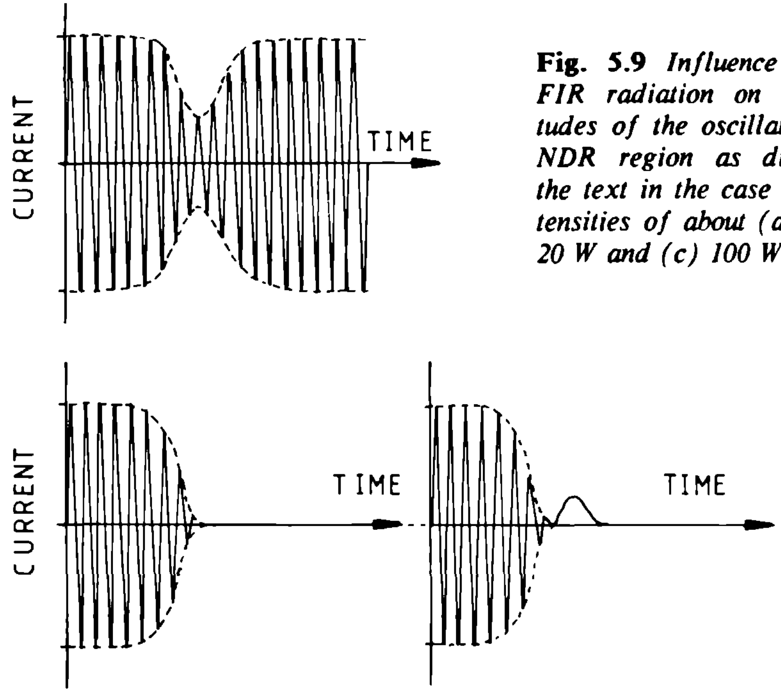

Fig. 5.9 *Influence of pulsed FIR radiation on the amplitudes of the oscillations in the NDR region as discussed in the text in the case of FIR intensities of about (a) 5 W; (b) 20 W and (c) 100 W.*

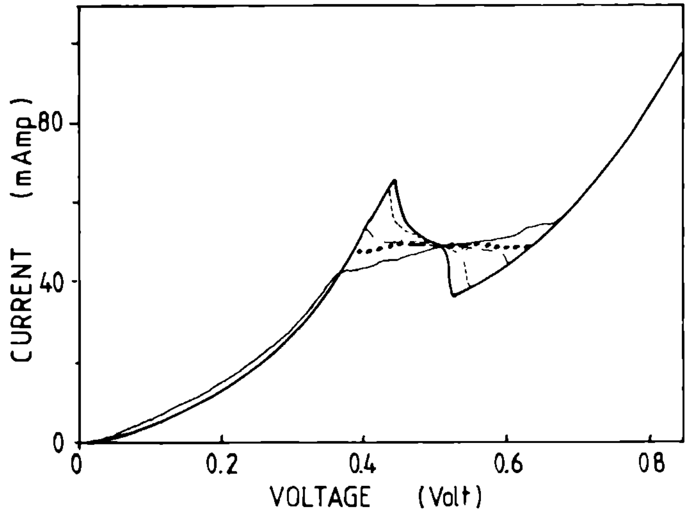

Fig. 5.10 *Smoothing of the IxV characteristic of sample (I) at room temperature for different values of an oscillating voltage with a frequency of 10 kHz additional to the DC bias voltage.*

Furthermore, it is noted that this amplitude modulation effect is enhanced as the FIR intensity is increased. At small intensities (≃5W) the amplitude of the oscillations is only modulated with the shape of the pulse. However, for higher intensities the oscillations were completely stopped. For maximal intensity (≥100W), a response was obtained as would normally be expected at this part of the 'wiggle'-structure in the I-V characteristic.

A second reason for the smoothing of the I-V characteristic is that the amplitude modulation depends on the value of the DC bias voltage within the NDR region as is shown in Fig. 5.11. Normally the peak-to-peak value of the oscillations is determined by the difference in current between the two extreme DC bias voltage values for which the current is still stable and without the presence of oscillations (A and B in Fig. 5.10). If the DC bias is near to one of these limiting voltages, the positive peak values of the oscillations have different values in comparison with the negative peak values. In the case of such non symmetric oscillations, the modulation by the FIR is proportional to both of the different amplitudes. Lastly, it is noted that these effects do not depend on the frequency of the radiation.

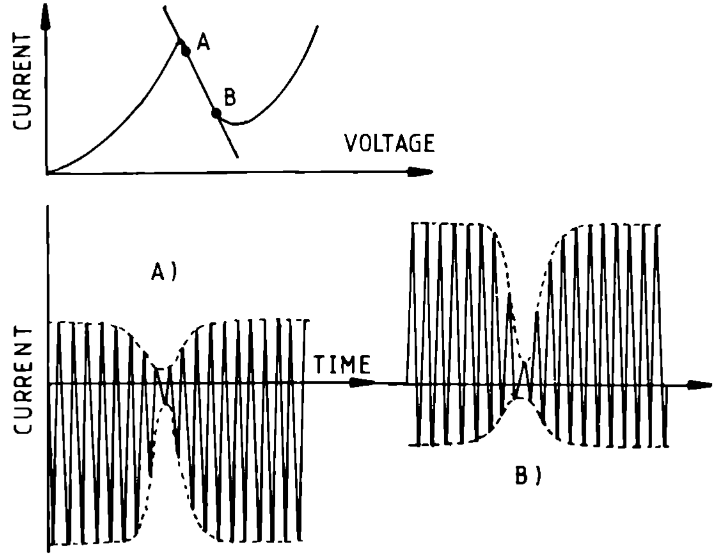

Fig. 5.11 *Amplitude modulation for non-symmetric oscillations at different bias points.*

5.5 Conclusions

As the experimental determination of the relative importance of both tunnelling mechanisms (coherent or sequential) is still an unsolved problem, a method has been proposed to distinguish between coherent and sequential tunnelling, based on the study of the response of the tunnel current to FIR radiation. In the coherent tunnelling model, the expected response for FIR radiation with a period time smaller than the coherent tunnelling time τ_c will be dependent of the photon energy. Introduction of a scattering time much shorter than the τ_c, leads to a FIR response which does not depend on the FIR frequency.

Therefore, the influence of FIR pulses on the tunnel current of several different GaAs/AlGaAs double barrier resonant tunnelling structures has been investigated. No FIR frequency dependence was observed as a function of bias voltage and, therefore, it is concluded that the tunnelling is dominated by sequential processes. Based on these experimental results, an upper limit for the scattering time $\tau_s \leq 1 \cdot 10^{-13}$ s has been deduced.

References

[1] R.L. Tsu and L. Esaki, Appl. Phys. Lett. 22, 562 (1973).

[2] *Electronic Properties of Multilayers and Low-Dimensional Semiconductor Structures*, p.243-349, Eds J.M. Chamberlain et al., Plenum Press, New York, 1990.

[3] M.L. Leadbeater, thesis, University of Nottingham, 1990, unpublished.

[4] T.C.L.G. Sollner, W.D. Goodhue, P.E. Tannenwald, C.D. Parker, and D.D. Peck, Appl. Phys. Lett. 43, 588 (1983).

[5] F. Capasso, K. Mohammed, and A.Y. Cho, IEEE J. Quantum Electron. QE-22, 1853 (1986).

[6] S. Luryi, Appl. Phys. Lett. 47, 490 (1985).

[7] A.D. Stone, and P.A. Lee, Phys. Rev. Lett. 54, 1196 (1985).

[8] M. Jonson, and A. Grincwaijg, Appl. Phys. Lett. 51, 1729 (1987).

[9] M. Buttiker, IBM J. Res. Dev. 32, 63 (1988).

[10] M.C. Payne, J. Phys. C 19, 1145 (1986).

[11] S. Collins, D. Lowe, and J.R. Barker, J. Phys. C 20, 6213 (1987).

[12] H.C. Torrey and C. Whitmer, *Crystal Rectifiers* (McGraw-Hill, New York, 1948).

[13] J.C. Tucker, IEEE J. Quan. Electron. QE-15, 1234 (1979).

[14] D.D. Coon and H.C. Liu, J. Appl. Phys. 58, 230 (1985).

[15] G.A. Toombs and F.W. Sheard in Ref. 2, p.257.

[16] V.A. Chitta, thesis, Grenoble, 1991, unpublished.

[17] A.A. Abrikosov, L.P. Gorkov, and I.E. Dzyaloshinski, *Methods of Quantum Field Theory in Statistical Physics* (Prentice-Hall, Englewood Cliffs, New York, 1963).

[18] G. Rickayzen, *Green's Functions and Condensed Matter* (Academic Press, New York, 1980).

[19] D. Heitmann, J.P. Kotthaus, and E.G. Mohr, Solid State Commun. 44, 715 (1982).

[20] F. Stern, Phys. Rev. Lett. 33, 960 (1974).

[21] T.C.L.G. Sollner, E.R. Brown, C.D. Parker, and W.D. Goodhue, in Ref. 2, p.283.

[22] E.R. Brown, T.C.L.G. Sollner, W.D. Goodhue, C.D. Parker, and C.L. Chen, Appl. Phys. Lett. 53, 385 (1988).

SUMMARY

This thesis describes an experimental study of different dynamical properties in semiconductor systems in which an excitation source has been used consisting of a pulsed far-infrared (FIR) laser. Three independent physical phenomena have been studied. The first concerns the excitation and recombination of the electron donor system, the second involves the spin-lattice relaxation of excited spins under electron paramagnetic resonance conditions (EPR) and the third is about electron transport through a tunnelling-structure under the influence of FIR radiation.

In chapter 2 a description is presented of the FIR pulse laser including its specific properties. Due to the application of plasma-reflection switches pulses of several nanoseconds can be generated with very well defined rise and fall characteristics. Additionally, by means of these switches it has become possible to produce pulse sequences. As an example a two pulse sequence has been generated consisting of two pulses having a duration of 10 ns with a time delay of 100 ns.

Chapter 3 considers time-resolved photoconductivity measurements with nanosecond resolution to study the recombination dynamics of photo-ionised shallow donor impurities in semiconductor materials as epitaxial grown GaAs with both a homogeneous or modulated impurity-doping characteristics and two-dimensional GaAs/AlGaAs quantum well structures.

The recombination time of electrons to photo-ionised donors was determined as a function of impurity concentration, temperature, electric field and reduction of dimensionality which can be achieved by confinement of a quantum well or application of a magnetic field. By means of a simple theory considering rate equation arguments, where only an electron-acoustic phonon interaction is taken into account, the impurity concentration can be considered a significant factor. As the concentration increases the relaxation time is found to decrease. The other parameters influence the recombination probability of the individual impurities.

Applying a magnetic field changes the energy levels of the bound states of the hydrogen-like donor impurity and as such the photoconduction which is induced by the ionisation of the resonantly excited $2p^+$ level. The measured reduction of the recombination time with increasing magnetic field can be explained by a theory which describes the transition probabilities under emission and absorption of acoustic phonons. The same arguments can be used to explain the very fast (<1ns) recombination in the case of shallow donor systems in quantum wells. The influence of the quantum well confinement on the energy levels of the hydrogen-like electron donor system is even more dramatic than the application of a magnetic field.

Chapter 4 considers pulsed EPR in dilute magnetic semiconductors. Measurements have been performed on crystals consisting of CdTe in which a small part of the Cd^{2+} ions is replaced by paramagnetic Mn^{2+} ions. A new technique to study the process of pulsed EPR is presented in which the change in the magnetisation of the paramagnetic crystal due to a resonant EPR FIR pulse is detected as an induction voltage in a pick-up coil around the crystal. After the excitation process the spin system relaxes back to thermal equilibrium due to spin-lattice coupling. Again an induction signal is observed, though with opposite polarity. In this way it is possible to measure directly the spin-lattice relaxation (SLR) time. The SLR times have been measured as a function of temperature and within the experimental resolution the results were explained by one-phonon processes.

In the appendix of chapter 4 a small feasibility study is presented about possible measurements of another important relaxation process known as spin-spin relaxation. By means of FIR pulse-sequence excitation of electron spin echoes the phase coherence of spins could be studied.

Finally, in chapter 5 an experimental study is described concerning the influence of FIR radiation on the transport properties through a tunnel structure with two potential barriers. Due to the existence of bound states in such a tunnel structure a maximum transmission through the structure can be achieved under resonant bias voltage conditions. The current-voltage characteristic, therefore, is found to be highly non-linear. If an oscillating electric field (i.e. radiation field) is applied over such a structure a rectification signal is expected.

In the description of the electron transport through a tunnel structure two different mechanisms can be distinguished: in the "coherent" process the phase correlation of the transport electron is conserved in contrast with the "sequential" process in which scattering processes destroy the phase correlation of the electron after tunnelling through the first barrier and before tunnelling through the second.

For all structures measured, the typical transit times for the coherent process were calculated to be much longer than the oscillation period of the FIR radiation. Therefore, in the case where the tunnel current is dominated by the coherent mechanism, a frequency dependence in the rectification characteristic is expected. Due to the fact that no frequency dependence is detected it is concluded that in the structures under study the typical time scale for the tunnel process is smaller than the FIR oscillation period. Therefore, it is concluded that the tunnel current has a mainly sequential nature. From this observation an upper limit for the scattering time may be estimated.

SAMENVATTING

Dit proefschrift beschrijft een experimenteel onderzoek naar verschillende dynamische eigenschappen in halfgeleider systemen waarbij als excitatie bron gebruik gemaakt is van een gepulste ver-infrarood (VIR) laser. Drie verschillende fysische systemen zijn hierbij onderzocht. Allereerst is de excitatie en recombinatie van het electron-donor systeem bestudeerd, vervolgens de spin-rooster relaxatie van geexciteerde spins onder paramagnetische resonante excitatie van electronen (EPR) en als derde systeem is het transport door een tunnel-structuur onder invloed van VIR straling onder de loep genomen.

In Hoofdstuk 2 wordt de beschrijving gegeven van de VIR laser alsmede van de specifieke eigenschappen hiervan. Door middel van toepassing van plasma-reflectie schakelaars kunnen pulsen van enkele nanoseconden worden gegenereerd met zeer goed gedefinieerde stijg en afval karakteristieken. Bovendien wordt het met deze schakelaars mogelijk puls-reeksen te realiseren. Als voorbeeld is een puls-reeks gerealiseerd van twee 10 ns pulsen et een interval van 100 ns.

Hoofdstuk 3 behandelt tijd opgeloste fotogeleidings metingen met nanoseconde resolutie aan ondiepe donor verontreinigingen in halfgeleider materialen zowel in epitaxiaal gegroeid GaAs met een homogene of gemoduleerde verontreinigings karakteristiek als in tweedimensionale GaAs/AlGaAs quantum-put structuren.

Onderzocht is hoe de recombinatie tijd van electronen met foto-geioniseerde donoren zich gedraagt afhankelijk van verontreinigings dichtheid, temperatuur, electrisch veld en de beperking van de bewegings vrijheidsgraden in geval van de quantum-put of toepassing van een magneetveld. Met behulp van een eenvoudig model, waarin alleen de wisselwerking tussen electronen en acoustische fononen is meegenomen, kan de dichtheid van de verontreinigingen als belangrijke factor gezien worden. Het blijkt dat met toenemende dichtheid de relaxatietijd afneemt. De andere parameters beinvloeden de recombinatie kans voor individuele verontreinigingen.

Door een magneetveld veranderen de energieniveaus van de gebonden toestanden van de waterstof achtige donor en dus ook de fotogeleiding die wordt geinduceerd door ionisatie van het resonant geexciteerde het $2p^+$ niveau. De gemeten afname van de recombinatietijd met oplopend veld kan worden verklaart met een theorie die de overgangswaarschijnlijkheden onder emissie en absorptie van acoustische fononen beschrijft. Het zelfde argument kan worden gebruikt voor de verklaring van de zeer snelle recombinatie (<1ns) in het geval van de quantum-putten. De invloed op de energieniveaus van de gebonden toestanden van een waterstofachtige donor door reduceren van de dimensie in een quantum-put is nog dramatischer dan het toepassen van een magneetveld.

Hoofdstuk 4 gaat over gepulste EPR in verdunde magnetische halfgeleiders. De metingen zijn gedaan aan CdTe kristallen waarin een deel van de Cd^{2+} ionen is vervangen door paramagnetische Mn^{2+} ionen. Een nieuwe techniek om EPR te meten met gepulst VIR is geintroduceerd waarbij de magnetisatie verandering van het paramagnetische kristal ten gevolge van de resonante VIR puls wordt gedetecteerd als een inductie spanning in een oppik-spoeltje om het kristal. Na de EPR-excitatie relaxeren de spins terug naar hun thermisch evenwicht door middel van de spin-rooster koppeling. Dit effect op haar beurt induceert wederom een spanning in het oppik-spoeltje (met tegengestelde polariteit) en zodoende kan op een directe manier de spin-rooster relaxatie (SRR) tijd worden bepaald. Metingen van deze SRR tijd zijn gerealiseerd afhankelijk van temperatuur en binnen de experimentele nauwkeurigheid verklaard met behulp van één-fonon processen.

In de appendix van hoofdstuk 4 wordt een korte voorstudie gepresenteerd over mogelijke metingen aan spin-spin relaxatie processen met behulp van VIR puls-reeksen. Door middel van de excitatie van electron spin echo's zou met deze meer-puls techniek de fase coherentie van spins bestudeerd kunnen worden.

In het laatste Hoofdstuk 5 wordt een experimentele studie beschreven over de invloed van VIR straling op het transport door een tunnel-sructuur met twee potentiaal drempels. Ten gevolge van het feit dat een dergelijke tunnel structuur gebonden toestanden kent in de richting van de potentiaal drempels is er onder de conditie van een resonante voorspanning over de structuur sprake van een maximale transmissie. De stroom-spannings karakteristiek is om die reden dan ook sterk niet-lineair en er wordt een gelijkrichtings-effect verwacht onder belasting met een oscillerend electrisch veld (cq. extern stralings veld).

Twee mechanismen zijn te onderscheiden bij het tunnel-transport van de electronen door de structuur: "coherent" waarbij de fase van het getransporteerde electron behouden blijft en "sequentieel" waarbij verstrooiingsprocessen de fase correlatie vernietigen omdat na transmissie door de eerste potentiaal drempel het electron verstrooit voordat het verder tunnelt. Voor alle gemeten structuren is de typische transmissie tijd voor het coherente proces veel groter dan de periode tijd van de VIR straling. Indien de tunnel-stroom geheel volgens het coherente mechanisme zou verlopen, zou een frequentie afhankelijkheid in de gelijkrichting verwacht worden. Op basis van het uitblijven van de frequentie afhankelijkheid wordt derhalve aangenomen dat de typische tijdschaal van het tunnel-proces kleiner is dan de VIR-periodetijd en daarom de tunnel stroom een sequentieel karakter heeft. Hieruit kan een bovengrens van de verstrooiingstijd afgeschat worden.

CURRICULUM VITAE

R.E.M. de Bekker

geboren 29 augustus 1962 te Deventer

1974-1980 : V.W.O. opleiding aan het Geert Grootte College te Deventer, afgesloten met een Gymnasium β diploma

1980-1987 : Studie Natuurkunde aan de Katholieke Universiteit Nijmegen, met als afstudeerrichting experimentele molekuul- en laser- fysica,
onder leiding van Prof. dr. J. Reuss

12 april 1984 : Kandidaats examen Natuurkunde, bijvak Informatica

12 februari 1987 : Doctoraal examen Natuurkunde

16 juni 1987 : Promotie onderzoek in dienst van het Max-Planck-Institut für Festkörperforschung (Hochfeld-Magnetlabor), Grenoble, Frankrijk,
onder leiding van Prof. dr. P. Wyder